THE VAN DER WAALS EPITAXY OF BISMUTH CHALCOGENIDE TOPOLOGICAL INSULATORS FOR TERAHERTZ PLASMONIC APPLICATIONS

by

Theresa P. Ginley

A dissertation submitted to the Faculty of the University of Delaware in partial fulfillment of the requirements for the degree of Doctor of Philosophy in Materials Science and Engineering

Fall 2019

2019 T.P. Ginley
All Rights Reserved

THE VAN DER WAALS EPITAXY OF BISMUTH CHALCOGENIDE TOPOLOGICAL INSULATORS FOR TERAHERTZ PLASMONIC APPLICATIONS

by

Theresa P. Ginley

Approved: ____
Darrin Pochan, Ph.D.
Chair of the Department of Materials Science and Engineering

Approved: ____
Levi T. Thompson, Ph.D.
Dean of the College of Engineering

Approved: ____
Douglas J. Doren, Ph.D
Interim Vice Provost for Graduate and Professional Education and Dean of the Graduate College

I certify that I have read this dissertation and that in my opinion it meets the academic and professional standard required by the University as a dissertation for the degree of Doctor of Philosophy.

Signed: ____

Stephanie Law, Ph.D.
Professor in charge of dissertation

I certify that I have read this dissertation and that in my opinion it meets the academic and professional standard required by the University as a dissertation for the degree of Doctor of Philosophy.

Signed: ____

Joshua Zide, Ph.D.
Member of dissertation committee

I certify that I have read this dissertation and that in my opinion it meets the academic and professional standard required by the University as a dissertation for the degree of Doctor of Philosophy.

Signed: ____

Robert Opila, Ph.D.
Member of dissertation committee

I certify that I have read this dissertation and that in my opinion it meets the academic and professional standard required by the University as a dissertation for the degree of Doctor of Philosophy.

Signed: ____

John Xiao, Ph.D.
Member of dissertation committee

ACKNOWLEDGMENTS

I would like to thank my advisor Dr. Stephanie Law for being my guide through this journey. This dissertation was a mental marathon that I would not have finished without your encouragement and understanding. The passion you have not only for research, but also for helping your students flourish is something I hope to carry with me wherever my career may wander It has been an honor to help you establish such a thriving lab.

I would also like to thank the family and friends who supported me in so many indispensable ways throughout this process. You are all honorary co-authors on this dissertation.

And of course, I thank my cats Edward and Tiberius. Without thier keen scientific insights none of this would have been possible.

TABLE OF CONTENTS

LIST OF TABLES viii
LIST OF FIGURES ix
ABSTRACT xv

Chapter

1 INTRODUCTION 1

2 THEORY 3

2.1 Topological Insulators 3

2.1.1 Band Gap Theory 3
2.1.2 Band structure of a Topological Insulator 5
2.1.3 Quantum Spin Hall effect 8
2.1.4 The Dirac Cone in Topological Insulators 11

2.2 Material Properties 12

2.2.1 Crystal Structure 12
2.2.2 Defect Types 13
2.2.3 In_2Se_3 14

2.3 Plasmons 14

2.3.1 Plasmons background 14
2.3.2 Plasmons in Topological Insulators 17

3 METHODS 21

3.1 Growth 21

3.1.1 Molecular Beam Epitaxy 21
3.1.2 Reflective High Energy Electron Diffraction 27

3.2 Characterization 29

3.2.1 Hall 29
3.2.2 Atomic Force Microscopy 30
3.2.3 Scanning Electron Microscopy 32
3.2.4 X-ray Diffraction 33

3.2.5 Fourier Transform Infrared Spectroscopy 34

3.3 Fabrication 36

4 THE GROWTH OF HIGH-QUALITY BISMUTH SELENIDE USING A SELENIUM CRACKER SOURCE 38

4.1 Introduction 38
4.2 Growth 39
4.3 Electrical Properties 40
4.4 Film Morphology 45
4.5 Summary 48

5 UNDERSTANDING THE ROLE OF DEFECT TYPE IN THIN FILM DOPING 49

5.1 Introduction 49
5.2 Controlling Alloy Composition 50
5.3 Preferential Selenium Incorporation 53
5.4 Electrical Properties 55
5.5 Indication of a Disordered Interface 56

6 BISMUTH INDIUM SELENIDE BUFFER LAYERS TO IMPROVE ELECTRONIC PROPERTIES 59

6.1 Introduction 59
6.2 Seed Layer 60
6.3 $(Bi_{0.5}In_{0.5})_2Se_3$ as a Buffer Layer 62
6.4 Topological Insulator Heterostructures 63
6.5 Conclusion 64

7 SELF-ASSEMBLED BISMUTH SELENIDE NANOWIRES IN VAN DER WAALS EPITAXY 65

7.1 Introdcution 65
7.2 Deoxidization 66
7.3 Seed Layer 67
7.4 Varying Selenium During Growth 68
7.5 Varying Indium:Bismuth Ratio 70
7.6 X-Ray Diffraction Data 71
7.7 Effectiveness of the Buffer Layer 73
7.8 Discussion 74
7.9 Conclusion 79

8 COUPLED 2D DIRAC PLASMONS IN BISMUTH SELENIDE THIN FILMS 80

8.1 Introduction 80
8.2 Extinction Spectra 82
8.3 Data Fitting 84

9 CONCLUSION 92

REFERENCES 95

LIST OF TABLES

Table 2.1 Lattice constants and bandgaps of Bi_2Se_3, Bi_2Te_3, and In_2Se_3. 14

Table 5.1 Growth parameters for films grown with varying alloy compositions. The lattice constants were determined by XRD and the tellurium content was calculated using Vegard's Law. [47] 51

Table 6.1 A description of all films discussed in sections 3 and 4. Including the composition of the TI layer, thickness and growth type of the buffer layer, thickness of the capping layer, mobility μ, and 2D sheet carrier concentration n_s [60]. 62

Table 7.1 A list of all samples included in this study. The selenium fluxes and indium contents given are those used during the $(Bi_{1-x}In_x)_2Se_3$ stage of the growths 66

Table 8.1 Frequency (ω_x), strength (S_x), and losses (γ_x) for the variables in equation (8.4) [86] 82

Table 8.2 Physical parameters (film thickness, d, stripe width, W), extracted fit parameters (plasmon frequency (ω_p), plasmon linewidth (γ_p), phonon-plasmon coupling factor (v), photon-phonon coupling factor (w), α-phonon frequency (ω_α), β-phonon frequency (ω_β), non-interacting phonon linewidth (γ_{NI}), and non-interacting phonon strength (S_{NI})), effective mode index (n_{eff}), and plasmon lifetime (τ_{pl}) for all samples. The error for the physical parameters (*d er* and *W er*) was calculated using the average deviation of values measured via AFM and profilometery. [86] 85

LIST OF FIGURES

Figure 2.1 Schematic of band structures for various types of materials. Filled states are represented in blue, while available states are shown in white. 4

Figure 2.2 Schematic of the formation of TSS a) normal band structure, b) band inversion due to strong spin orbit coupling, c) band renormalization, and d) formation of the topological surface states. [15] 5

Figure 2.3 Schematic of coupled states forming in neighboring identical quantum wells. [18] 7

Figure 2.4 Band diagram of the topological insulator Bi_2Se_3 (a) without adjusting for spin orbit coupling and (b) with spin orbit coupling. The lifting of the degeneracy can be and the avoided level crossing can be clearly seen at the Γ point. [19] 7

Figure 2.5 Schematic of topologically distinct insulating, Quantum Hall, and Quantum Spin Hall states. [22] 9

Figure 2.6 The Dirac Cone formed by the TSS. [25] 11

Figure 2.7 Crystal structure of tetradymite Bi_2Se_3 (other TI materials are similar). Bi atoms are large and shown in blue while Se atoms are smaller and shown in yellow. (**a**) Crystal structure along the a-b plane showing two quintuple layers with the van der Waals gap between them. (**b**) Crystal structure along the c-axis. [27] 12

Figure 2.8 The oscillation of electrons and resulting electric field of a surface plasmon polariton...15

Figure 2.9 The dispersion of a plasmon at the interface between a metal and air, as well as a metal and a silica prism.[35] 16

Figure 2.10 The time resolved oscillation of electrons and resulting electric field of a localized surface plasmon...17

Figure 2.11 A schematic of coupled Dirac plasmons showing the induced electric field (yellow) at both surfaces of the topological insulator (blue). [113] 18

Figure 2.12 The theoretical dispersion relations of a 2D massive plasmon (dotted line) and 2D couple Dirac Plasmons with varying film thicknesses (solid lines). A 2D carrier density of $ns = 2.38 \times 1013$ cm^{-2} was used for the calculation.. 19

Figure 3.1 A schematic of an MBE chamber. 22

Figure 3.2 Schematics of (left) a traditional Knudsen effusion cell with the outgassing molecules depicted as molecular beam and (right) a cracker cell with the outgassing molecules depicted as clusters of atoms. 22

Figure 3.3 A diagram of behaviors at the growth surface. From left to right: impinging atom, evaporation, hopping between equal sites, hopping to a step edge, hopping up a step edge, and hoping down a step edge. Black arrows represent behaviors who rate is primarily dependent on substrate temperature and source flux, green arrows represent typically energetically favorable moves, and the red arrow represent a move that is generally unfavorable. Blue circles represent stylized substrate atoms and yellow circles represent adatoms. 24

Figure 3.4 RHEED diffraction geometry and construction of the Ewald sphere. [49][50] 27

Figure 3.5 Example RHEED patterns for a) single crystal, b) polycrystalline, and c,d) 3D growth. 28

Figure 3.6 A schematic of the measurement set up Hall (left) and van der Pauw (right) measurements. 29

Figure 3.7 A schematic of an AFM set up.[52] 30

Figure 3.8 (a) Approach and withdrawal of the AFM-tip in a single tapping cycle (b) principle of Peak Force Tapping operation with the tip trajectory (c) schematic of force-distance curve obtained at each tapping cycle with the peak force as controlling parameter. [53] 31

Figure 3.9 Generation of secondary electrons. [56] 32

Figure 3.10 Diagram of the focusing components of an SEM. [57] 32

Figure 3.11 Reflection off of crystal planes that cause peaks in XRD patterns due to Bragg's Law. [58] 33

Figure 3.12 A diagram of a Michelson interferometer.[61] 34

Figure 4.1 Room temperature sheet density (open symbols) and mobility (closed symbols) as a function of substrate temperature for Bi2Se3 films grown with Se:Bi ratios of 2:1 (black squares), 3:1 (red circles), 4:1 (green triangles), and 6:1 (blue diamonds). The lines are a guide to the eye. For all sheet density and some mobility measurements, the error bars are smaller than the size of the symbols and are not visible on this plot. [38] 41

Figure 4.2 Sheet density (top, open symbols) and mobility (bottom, closed symbols) over time for films with thickness 10nm (black squares) and 20nm (red circles). The sheet density remains constant, indicating reduced ageing effects. [38] 44

Figure 4.3 2μm x 2μm AFM scans for 100nm films grown with varying flux ratios, as indicated. [38] 45

Figure 4.4 AFM scans of 100nm Bi_2Se_3 films grown using a 4:1 Se:Bi BEP ratio at varying substrate temperatures. [38] 46

Figure 4.5 AFM scans of Bi_2Se_3 films with different thicknesses grown using a 4:1 Se:Bi BEP ratio at a substrate temperature of 300°C. [38] 47

Figure 5.1 HAADF STEM image of Bi_2Te_2.7Se0.3 viewed along the [100] direction. The corresponding Te, Se, and Bi atomic resolution EDS maps are shown at the top. Note the Se signal resides in the Te(2) position. [73] 49

Figure 5.2 a) Wide-range XRD spectra for samples with different tellurium content, as indicated in the legend. Tellurium content increases from top to bottom. All intensities are normalized and data is offset for clarity. b) The [0021] peak showing the shift in peak position with tellurium content. The growth parameters for samples in this Figure can be found in Table 5.1. [74] 52

Figure 5.3 XRD spectrum of samples grown with a fixed flux ratio and a variable substrate temperature. The blue line represents the sample grown with a two-step procedure: a substrate temperature of 200°C for first 4 QLs and followed by a ramp up to 300°C for the rest of the growth. Lines on the far left and far right are pure Bi_2Te_3 and Bi_2Se_3 respectively, for comparison. [74] 53

Figure 5.4 The mobilities (black) and sheet carrier concentrations (blue) of films grown with varying tellurium content. As tellurium content increases the mobility trends downwards while the carrier concentration trends

upwards. Data clusters around 33% and 66% indicate samples with different growth parameters but similar compositions. [74] 55

Figure 5.5 a)-d) The progression of the RHEED pattern from polycrystalline rings to single crystal streaks over the course of 5-15 QL (depending on growth conditions). 56

Figure 5.6 The a) sheet carrier density and b) mobility of films of varying thickness. 57

Figure 6.1 Comparison of co-deposited (a, b) BIS films with BIS films grown on a sequentially deposited seed layer (c, d, e). (a) XRD scans of five co-deposited BIS films with indium concentration increasing from bottom to top, as indicated in the legend. All the scans are normalized to the maximum of each scan and offset for clarity. For high indium content films, the FWHM of the peaks increases and double-peaks begin to arise, indicating poor crystal quality. (b) RHEED image of a co-deposited (Bi0.5In0.5)2Se3 film showing wide, diffuse streaks with intensity variation, indicating polycrystalline growth. (c) XRD scans of five BIS films grown on a sequentially-deposited seed layer with the same compositions as in (a). For all films, the peak FWHM is narrow and no double-peaks are observed. (d, e) RHEED images in the 1010 (d) and 1120 (e) directions showing thin lines and different streak spacing, indicating high-quality, single-crystal film growth.[88] 60

Figure 6.2 Room temperature sheet density and mobility of the samples listed in Table 6.1. Black symbols represent Bi_2Se_3 samples while red symbols represent Bi_2Te_3. Circles are unbuffered samples, squares are buffered samples, and triangles are layered heterostructures. Error bars were included for all images but may be hidden by the symbol. 63

Figure 7.1 RHEED (a-c) and AFM (d-f) images of various stages in seed layer development. (a) and (d) show 5nm of Bi_2Se_3 (Sample A); (b) and (e) show 5nm of In_2Se_3 on 5 nm of Bi_2Se_3 (Sample B); (c) and (f) show the completed seed layer after annealing (Sample C). All AFM images are 2μm x 2μm and have the same scale bar and orientation relative to the substrate. 67

Figure 7.2 RHEED (a-c), SEM (d-f), and AFM (g-i) images of complete $((Bi_{0.5}In_{0.5})_2Se_3$ buffer layer grown at varying selenium over pressures. (a), (d), and (g) show Sample D grown with a low selenium overpressure; (b), (e), and (h) show Sample E grown with a moderate selenium overpressure; (c), (f), and (i) show sample F grown with a high selenium overpressure. All SEM images have the same scale bar and substrate

orientation. All AFM images are 2μm x 2μm and have the same scale bar. 69

Figure 7.3 (a-e) AFM images of $(Bi_{x-1}In_x)_2Se_3$ films grown at varying indium to bismuth ratios: (a) Sample G with x=1, (b) Sample H with x=0.75, (c) Sample I with x=0.5, (d) Sample J with x=0.25, (e) Sample K with x=0. All AFM images are 2μm x 2μm and have the same scale bar and orientation relative to the substrate. (f) Line cuts of (d) and (e) showing the heights of the nanowires. 70

Figure 7.4 XRD scans of (a) Samples D, E, and F and (b) Samples G-K. The * represents a standard orientation $(Bi_{1-x}In_x)_2Se_3$ peak while the κ represent a κ-phase In_2Se_3 peak. 72

Figure 7.5 AFM images of Bi_2Se_3 grown on (a) a smooth buffer later (Sample L) or (b) a buffer layer with a needle morphology (Sample M). (c) XRD scans of Sample L (red) and Sample M (blue). 73

Figure 8.1 Extinction as a function of frequency for a sample with $d = 100$nm and $W = 2$μm for TE (red) and TM (black) polarized light. The α and β phonons are marked in the TE spectrum. Inset shows a scanning electron microscopy plot of a fabricated stripe array with the TE and TM electric field directions indicated. [113] 82

Figure 8.2 Extinction spectra for samples with stripe width of 1μm (a), 2μm (b), and 4μm (c). Film thicknesses of 200nm (red square), 100nm (black circle), and 50nm (yellow diamond) are shown in each plot. 83

Figure 8.3 Normalized experimental data (squares) and fit model (line) for the W=2μm d=100nm sample.[113] 85

Figure 8.4 Extracted fitting parameters as a function of stripe width: plasmon frequency (a), plasmon linewidth and lifetime (b), phonon-plasmon coupling (c), and photon-phonon coupling (d). Film thicknesses of 200nm (red square), 100nm (black circle), and 50nm (yellow diamond) are shown in each plot. Dashed lines are a guide to the eye. Numerical values for these data are tabulated in Table 8.2 [113]. 86

Figure 8.5 Experimental plasmon frequencies and theoretical dispersion curves for coupled 2D Dirac plasmons. (a) Theoretical curves for *d*=200nm (red line), *d*=100nm (black line), and *d*=50nm (yellow line). Experimental plasmon frequencies are shown as triangles (*W*=1μm), circles (*W*=2μm), and squares (*W*=4μm) in the corresponding thickness color. Dashed line

shows the theoretical dispersion for a massive plasmon with $ns = 2.38 \times 1013$ cm^{-2}. (b) Theoretical curves for W=1μm (red line), W=2μm (black line), and W=4μm (yellow line). Experimental plasmon frequencies are shown as triangles (W=1μm), circles (W=2μm), and squares (W=4μm) in the corresponding stripe width color. Dashed line shows the dispersion curve for a massive plasmon with $n3D = 1.5 \times 1021$ cm^{-3}. [113]......... 89

ABSTRACT

Bismuth chalcogenide topological insulators are of great interest to scientist due to their unique band structures. They are characterized by linear surface states that cross the bulk band gap. In these surface states, electrons are confined to two dimensions in a Dirac cone, much like electrons in graphene. It is these surface states electrons that make topological insulators so interesting, as electrons that inhabit them are massless, travel at relativistic speeds, and are spin polarized. Understanding these materials could help in fundamental physics applications, like the search for the Majorana fermion or the definition of the Ohm, to device-based applications, such as spin computing or improving sensors in hard to reach frequency ranges.

The key to good material science research is the ability to produce high quality material. To that end this dissertation explored the growth of bismuth chalcogenide topological insulators. We sought to not only improve the quality of the material, but to understand the mechanism at work in van der Waals epitaxy. The growth of $Bi_2Se_3$with a selenium cracker cell on sapphire substrates was explored to reduced selenium vacancies and improve the electrical properties of the system. Results from initial research suggested that bulk behaviors did not dominate in thin films and instead a layer of disorder at the interface was to blame for the high bulk doping in thin films. Thus, a $(Bi_{1-x}In_x)_2Se_3$ buffer layer was used to bury the interface, resulting in reduced bulk carriers and improved mobilities. Attempts to recreate this buffer layer on GaAs(001) substrates resulted in complex 3D morphologies in the

$(Bi_{1-x}In_x)_2Se_3$. We attribute these morphologies to the interaction of bismuth with the reconstructed surface of GaAs(011) after deoxidization, as well as the tendency of In_2Se_3 to phase segregate. Finally, the unique properties of topological insulators were explored by demonstrating the excitation of coupled two dimensional Dirac plasmons in patterned Bi_2Se_3 samples. This dissertation demonstrates improved knowledge of van der Waals epitaxy as well as contributing to the field of three-dimensional topological insulators.

Chapter 1

INTRODUCTION

Material science research often focuses on finding new materials with applications we are only just beginning to think of. Bismuth chalcogenide topological insulators are once such material whose potential applications vary from fundamental physics exploration, in the search for the Majorana fermion [1,2] or the metrology of the Ohm [3], to device-based applications, such as spin computing [4,5] or improving sensors in hard to reach frequency ranges [6]. The unique band structure of these devices create linear surface states in which electrons are confined and behave in a similar way to those in graphene [7–9]. The two-dimensional surface states are the key to much of the behaviors that make researchers so excited about these materials. However, bismuth chalcogenide topological insulators are a fundamentally three-dimensional material [10] [11], so they do not suffer from the same manufacturing challenges as their two-dimensional counterparts. Thin films of these materials can instead be produced using molecular beam epitaxy, a technique already proven for the commercial manufacturing of high-quality semiconductor devices. The marriage of two-dimensional properties with three-dimensional production techniques makes bismuth chalcogenide topological insulators a highly promising material system for a wide variety of applications.

The key to good material science research is the ability to produce high quality material. To that end this dissertation explored the growth of bismuth chalcogenide

topological insulators. We sought to not only improve the quality of the material, but to understand the mechanism at work in van der Waals epitaxy. The growth of Bi_2Se_3 with a selenium cracker cell on sapphire substrates was explored to reduced selenium vacancies and improve the electrical properties of the system. In addition, the alloying of Bi_2Se_3 and Bi_2Te_3 was explored in the hope that thin films mirrored bulk behavior and the major defect sources for each of these two materials would counter act each other. Results from these two research projects suggested that bulk behaviors did not dominate in thin films and instead a layer of disorder at the interface was to blame for the high bulk doping in thin films. Thus, a $(Bi_{1-x}In_x)_2Se_3$ buffer layer was used to bury the interface, resulting in reduced bulk carriers and improved mobilities. Attempts to recreate this buffer layer on GaAs(001) substrates resulted in complex 3D morphologies in the $(Bi_{1-x}In_x)_2Se_3$. We attribute these morphologies to the interaction of bismuth with the reconstructed surface of GaAs(011) after deoxidization, as well as the tendency of In_2Se_3 to phase segregate. Finally, the unique properties of topological insulators were explored by demonstrating the excitation of coupled two dimensional Dirac plasmons in patterned Bi_2Se_3 samples. This dissertation demonstrates improved knowledge of van der Waals epitaxy as well as contributing to the field of three-dimensional topological insulators.

Chapter 2

THEORY

Thoroughly understanding the theory behind your work before you begin any experiments is key to scientific success. Proper understanding of the material saves time and resources by enabling you to design efficient experiments. If, as often happens in research, you get unexpected results, returning to the underlying science helps you to reshape your theory to incorporate the new data. Much of this dissertation is focused on understanding growth dynamics of bismuth chalcogenide topological insulators. This chapter seeks to explain why these materials are of such great interest to scientists and to explore the origin of their unique properties.

2.1 Topological Insulators

2.1.1 Band Gap Theory

Quantum physics tells us that electrons in an atom can only occupy certain discrete energy levels, called orbitals. When multiple atoms come together to form a molecule through covalent bonds, these orbitals shift and combine as the atoms share electrons. In even more complex arrangements, such as a crystal lattice, there are a multitude of allowed energy states that combine to form an allowed energy band. However, there will still be energies that the electron cannot occupy [12]. The band theory of solids allows materials to be classified by these regions of allowed and

forbidden energies and can predict the behavior of materials individually or when combined into heterostructures. [13]

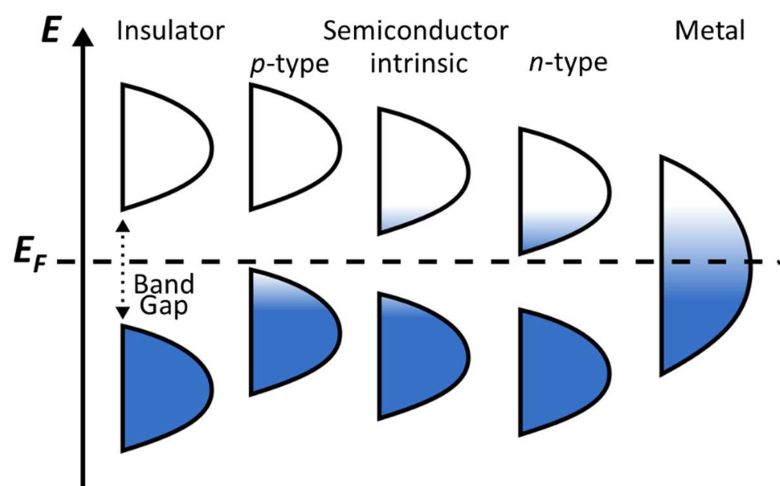

Figure 2.1 Schematic of band structures for various types of materials. Filled states are represented in blue, while available states are shown in white.

The classification of a material in terms of band theory relies on the relative positions of occupied states, unoccupied states, and a threshold known as the Fermi level (as shown in Figure 2.1). Band theory uses the Fermi-Dirac distribution to determine the probability that a state with a specified energy will be occupied. The energy at which this probability is 50% is called the Fermi energy (or Fermi level). If the Fermi level lies in the middle of an allowed band, the material is a metal. The easy availability of states for electrons to transition between aids in the flow of charge through a metal. In insulators, the Fermi level lies in the middle of a large gap, called the band gap, between two allowed energy regions. This results in a fully occupied band, called the valence band, below the Fermi level and an empty band, called the conduction band, above. The lack of unoccupied states in the valence band prevents current from flowing. Similar to insulators is a class of materials called semiconductors, which still have a Fermi level located between a valence band and a conduction band. However, the band gap of a semiconductor is much smaller than in an insulator, allowing for each band to be only partly occupied. Some free electrons

will occupy states in the conduction band, while some unfilled states known as holes are present in the valence band. If the Fermi level is closer to the valence band the semiconductor is referred to as p-type while a semiconductor with the Fermi level close to the conduction band is called n-type [12,13].

2.1.2 Band structure of a Topological Insulator

In the bulk, topological insulators like Bi_2Se_3 and Bi_2Te_3 tend to have small band gaps (0.3eV and 0.2eV respectively), meaning they would be classified as semiconductors. However, due to their unique band structure, these materials demonstrate much more complex behaviors than simply n-type or p-type behavior [14]. The formation of topological surface states can be understood by starting with a simple semiconductor model (Figure 2.2.a) [15] and adding in complexity to better approximate real behavior.

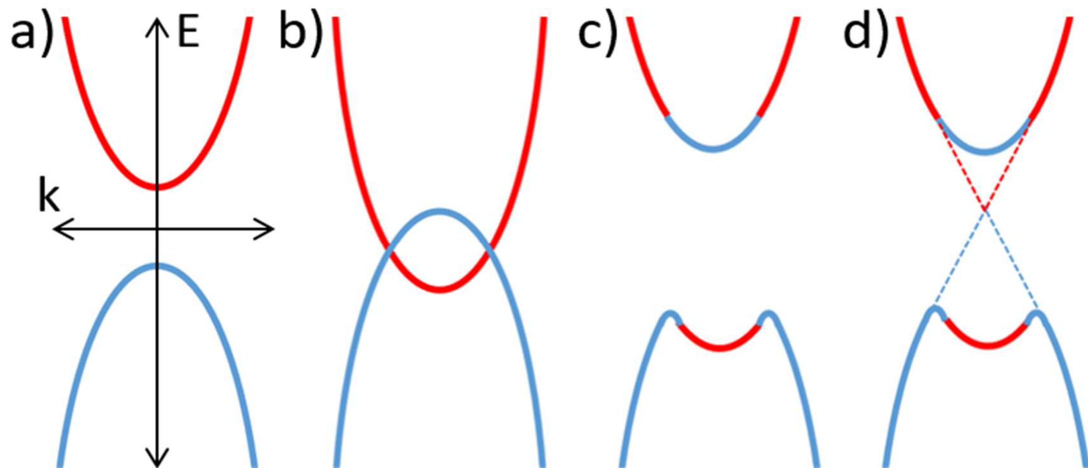

Figure 2.2 Schematic of the formation of TSS a) normal band structure, b) band inversion due to strong spin orbit coupling, c) band renormalization, and d) formation of the topological surface states. Reproduced with permission from [15]

First, the effects of spin-orbit coupling on the band structure must be considered. Since an electron carries charge, its orbit around the nucleus induces a magnetic field. The interaction between the induced magnetic field and the electron's spin is called spin-orbit coupling and its strength is proportional to $\boldsymbol{l} \cdot \boldsymbol{s}$, where $\boldsymbol{l}$ is the orbital angular moment and $\boldsymbol{s}$ is the spin angular momentum. In bulk crystalline materials, spin-orbit coupling affects the band structure most strongly at degenerate points (points that are occupied by more than one allowed band with equal energies) near the Fermi level. Spin-orbit coupling causes the degenerate bands to split apart resulting in a shifting of the valence band energy by $\Delta E_v \propto Z^4$, where Z is the atomic number. High Z elements tend to have large atomic radii and thus large $\boldsymbol{l}$ for the outer electrons leading to high energy shifts ΔEv. [16] We are therefore most likely to observe behaviors derived from strong spin-orbit coupling in materials containing high Z elements.

Bi2Se3 and Bi2Te3 experience a large spin orbit coupling effect primarily due to bismuth's high atomic number of 83. In fact, the spin orbit coupling is so strong that it pushes the conduction and valence bands over each other creating a band inversion [17], as can be seen in Figure 2.2.b. The overlapping bands create new degenerate points which are forbidden due to the Pauli exclusion principle. The conduction and valence bands will renormalize to form an avoided level crossing and prevent this degeneracy. This behavior can be understood through the similar situation of two identical quantum wells in close proximity. Here the degenerate states couple to become a symmetric state of lower energy and an antisymmetric state of higher energy as can be seen in Figure 2.3 [18]. The total energy is conserved but the electrons now inhabit different energy levels while the original energy level is

forbidden. [18] Similarly, the band structure of the TI will renormalize to prevent band overlap, while conserving total energy. A key point for topological insulators is that when the bands renormalize parts of the original conduction band become part of the valence band and vice versa, as shown in Figure 2.2.c. Figure 2.4 [19] shows the calculated band diagram of Bi_2Se_3 before and after incorporating spin orbit coupling and avoided level crossings. The differences can be seen most clearly at the Γ point where the inclusion of spin orbit coupling creates a drastic change in the band structure [19].

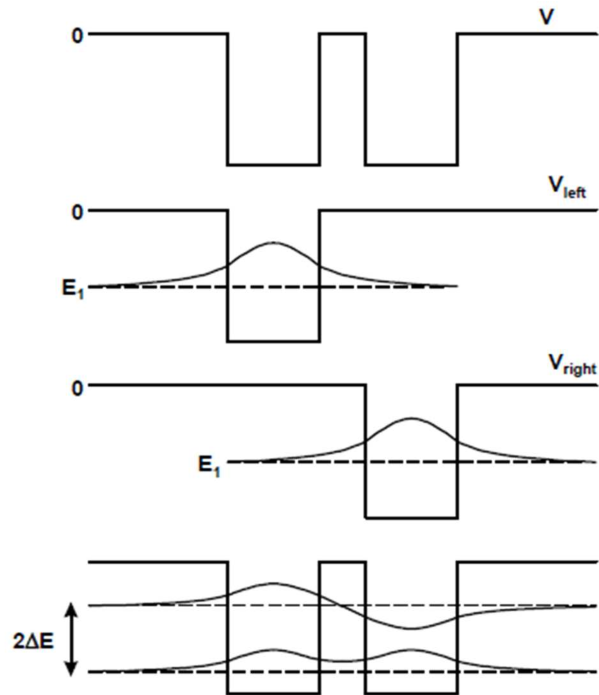

Figure 2.3 Schematic of coupled states forming in neighboring identical quantum wells. [18]

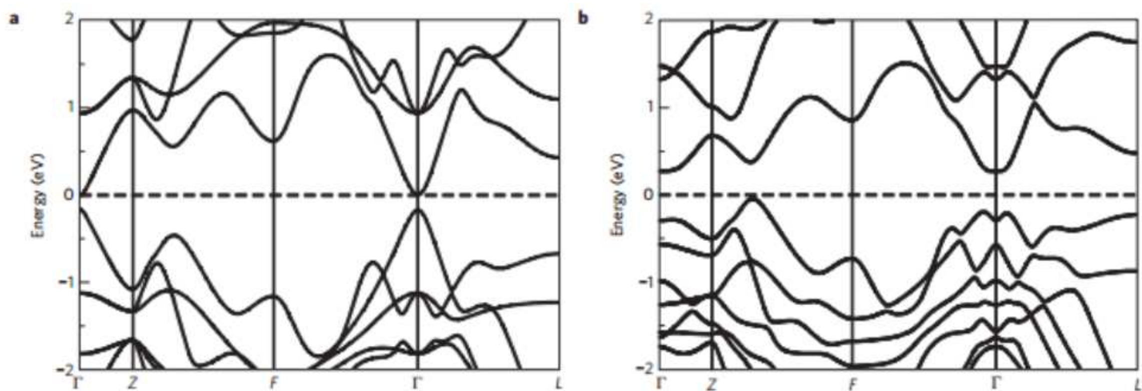

Figure 2.4 Band diagram of the topological insulator Bi_2Se_3 (a) without adjusting for spin orbit coupling and (b) with spin orbit coupling. The lifting of the degeneracy can be and the avoided level crossing can be clearly seen at the Γ point. Reproduced with permission from [19]

So far, all the processes discussed have relied on an implicit assumption that electrons can be modeled as Bloch waves described by

$$\psi(\boldsymbol{r}) = e^{\,i\boldsymbol{k}\cdot\boldsymbol{r}} u(\boldsymbol{r}) \quad (2.1)$$

This describes a plane wave ψ in a periodic potential $u(\boldsymbol{r})$ caused by the crystal structure where r is position, e is Euler's number, i is the imaginary unit number, and k is the crystal wave vector. One implication of the Bloch function is the boundary condition [13]

$$u(\boldsymbol{r} + \boldsymbol{a}) = u(\boldsymbol{r}) \quad (2.2)$$

While this is very useful for describing bulk behavior, it cannot be applied at surfaces, where the periodic nature of the Bloch function no longer applies. At the surfaces ψ and $d\psi/dx$ must remain continuous, which means that the conduction band in material 1 must meet the conduction band in material 2, and the same for the valence bands. In 3D topological insulators however the band inversion adds another complication. At the surface, the s-orbitals in the TI must connect to the s-orbitals in the normal material and likewise for the p-orbitals. This is achieved through the formation of gapless linear surface states connecting each band (Figure 2.2.d) [20]. These topological surface states (TSS) comprise a Dirac cone and are the basis for much of the interesting behaviors of topological insulators [21].

2.1.3 Quantum Spin Hall effect

To understand the meaning of a topological state it is useful to look at the evolution of topological states in 2D. Imagine an electron traveling in the xy plane. If

a magnetic field is applied in the z direction, the electron will experience a force perpendicular to both its direction of travel and to the magnetic field (in accordance with the right-hand rule). Given a large enough xy plane, the force pushing the electron will result in a circular travel path, known as a cyclotron orbit, whose radius is dependent on the strength of the applied magnetic field and the mass of the particle. Charged particles traveling in cyclotron orbits have quantized energy levels called Landau levels. As the strength of the applied magnetic field increases, the radius of the cyclotron orbit decreases and the number of states per Landau level increases. At sufficiently high magnetic fields, the orbits become so small that all the electrons in the sample can reside in only a few Landau levels.

In the center of the material, the electrons traveling in complete cyclotron orbits result in insulating behavior as there is no net movement of electrons. However, along the edge of the material the cyclotron orbit path intersects with the interface. Here the electron will scatter back off the interface and try to establish a new orbit.

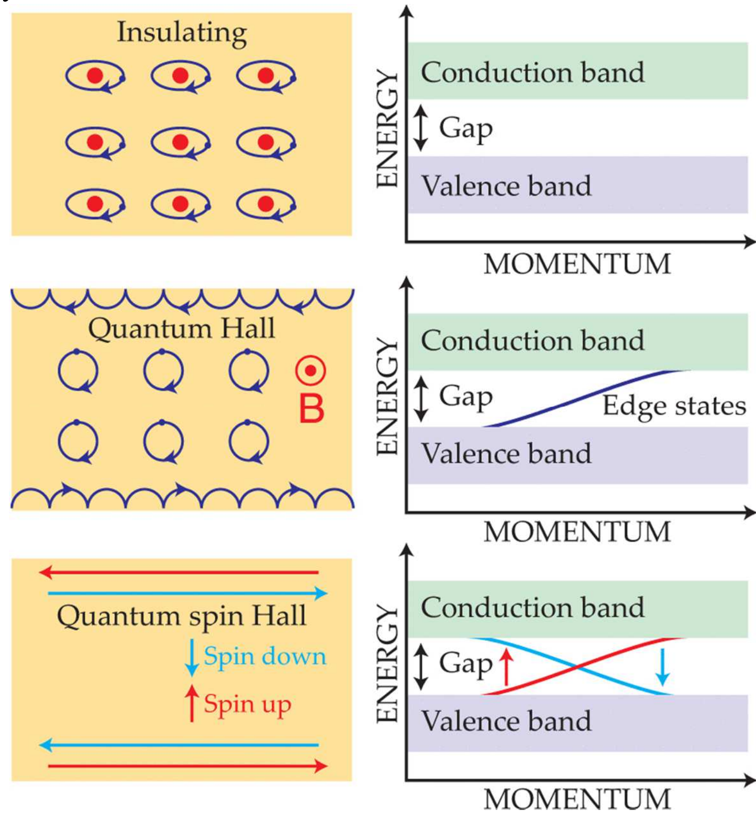

Figure 2.5 Schematic of topologically distinct insulating, Quantum Hall, and Quantum Spin Hall states. Reproduced with permission from [22]

The series of incomplete edge orbits form a band of available states which results in a flow of electrons around the edge of the sample, as can be seen in Figure 2.5 [22]. The electrons in this scenario are confined to two dimensions so the energy states they can occupy become highly quantized and only certain Landau levels are allowed. This quantization can be seen by measuring the Hall resistivity, ρ_{xy}, and the longitudinal resistivity, ρ_{xx}, under a strong varying magnetic field. Changing the magnetic field shifts the energy of each Landau level with regard to the Fermi Level of the sample. If the Fermi level lays between Landau levels, ρ_{xy} plateaus and ρ_{xx} goes to zero. However, if the Fermi level lays within a Landau level, ρ_{xy} increases and ρ_{xx} spikes. This results in a step like behavior in ρ_{xy} with accompanying spikes in ρ_{xx}. This phenomenon is known as the Quantum Hall effect and is only observable in 2D samples with high mobility measured under a large magnetic field at low temperature to prevent any phonon scattering [23].

In the quantum spin Hall effect the spin orbit coupling of a material is strong enough to produce a magnetic field large enough to create edge states like those seen in the quantum Hall effect [22,24]. However, since the effect is now dependent on the interaction with spin, two edge states will be created: one for spin up electrons and one for spin down electrons (Figure 2.5). The insulating, quantum hall, and quantum spin hall states described above are referred to as topologically distinct. This means you cannot transition between the three via continuous deformation of the band structure. Instead the band gap must be collapsed and reopened by some significant perturbation (e.g. a large magnetic field or strong spin orbit coupling).

2.1.4 The Dirac Cone in Topological Insulators

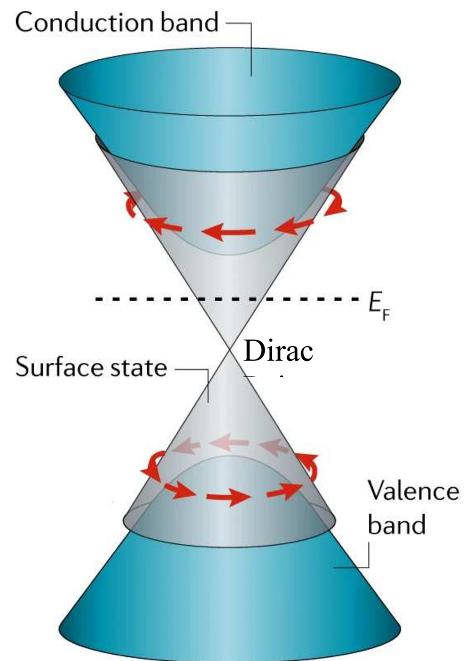

Figure 2.6 The Dirac Cone formed by the TSS. Reproduced with permission from [25]

Electrons that occupy the TSS (topological surface states) behave fundamentally differently than bulk carriers. Electrons traveling through a repeating crystal lattice can be modeled as electrons in free space with an altered mass. This is called the effective mass of the electrons and it is dependent on the curvature of the band that electron is occupying. Since the Dirac cone, pictured in Figure 2.6 [25] is linear the lack of curvature results in an effective mass of zero (to first order approximation). These electrons are referred to as massless Dirac electrons, much like electrons found in graphene.

Unlike in graphene, electrons in the TSS are spin momentum locked. Like in the quantum Spin Hall effect, strong spin-orbit coupling results in certain allowed electron motions based on their spin. In this case the momentum and spin are locked perpendicular to each other, following the left-hand rule if the Fermi level is above the Dirac point or the right-hand rule if it's below. TSS are extremely robust due to protection from the spin momentum locking and time reversal symmetry. For any electrons in the TSS to change direction, it would require for their spins to flip, which is only possible with a magnetic perturbation [13]. In the absence of a magnetic perturbation, TSS electrons tunnel through any impurities they encounter maintaining their direction and spin [26]. Scattering into trivial bulk states is possible but not

highly probable. Electrons in the surface state of topological insulators are therefore extremely scattering resistant leading to theoretically lossless electron transport. In addition, since there is little scattering to reduce the velocity of the electrons, they will travel at relativistic speed [26]. Both these qualities make electrons in the surface states of topological insulators excellent candidates for spin computing.

2.2 Material Properties

2.2.1 Crystal Structure

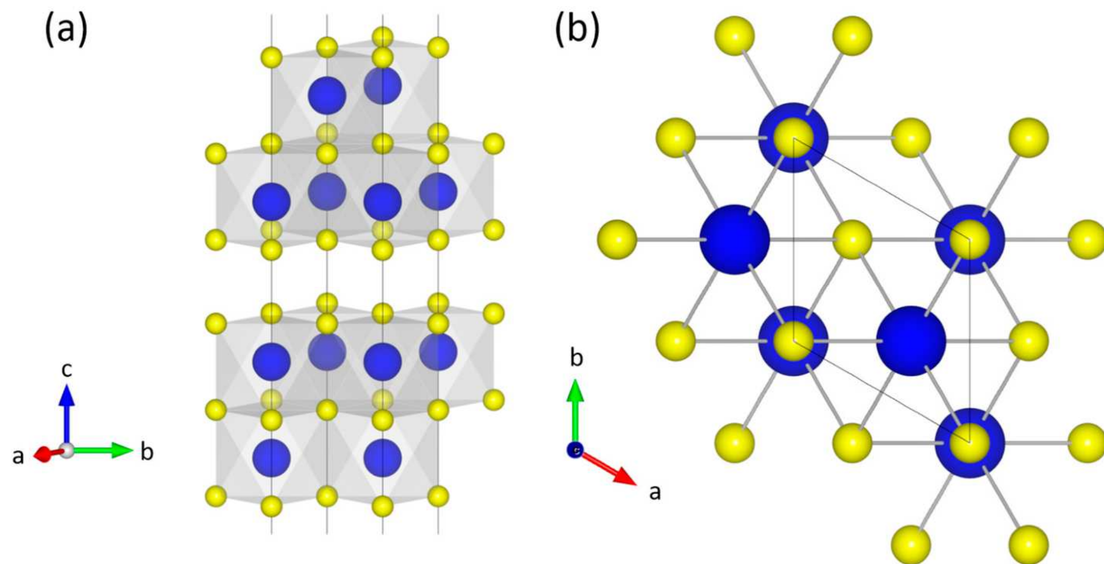

Figure 2.7 Crystal structure of tetradymite Bi_2Se_3 (other TI materials are similar). Bi atoms are large and shown in blue while Se atoms are smaller and shown in yellow. (**a**) Crystal structure along the a-b plane showing two quintuple layers with the van der Waals gap between them. (**b**) Crystal structure along the c-axis. Reproduced with permission from [27]

Bi_2Se_3, Bi_2Te_3, and their alloy are commonly studied 3D topological insulators. As can be seen in Figure 2.7 [27], their hexagonal crystal structure consists of 5 alternating layers of Se/Te and Bi forming a quintuple layer (QL). QLs are held together by weak van der Waals forces in the *c*-axis. [28] While some researchers refer

to the QL as the unit cell of the crystal, others define it as 3 stacked QLs since the threefold symmetry of the material requires 3 QL before the identical rotational position is restored. As can be seen in Table 2.1, the lattice constants of both Bi_2Se_3 and Bi_2Te_3 are very similar, however the slightly larger band gap of Bi_2Se_3 has made it the more popular choice for study as a topological insulator [29]. Additionally, the Dirac point of Bi_2Se_3 is located in the bandgap while the Dirac point of Bi_2Te_3 is obscured below the top of the valence band [30]. It is theoretically possible to tune the Fermi energy through the Dirac point in Bi_2Se_3 to observe the materials behavior as the density of states shrinks to zero at the Dirac point.

2.2.2 Defect Types

Bi_2Se_3 and Bi_2Te_3 also differ in the types of vacancies they are prone to. In bulk films, Bi_2Se_3 tends to be n-type doped, which is most commonly attributed to selenium vacancies. Bi_2Te_3, on the other hand, is more prone to Bi-Te antisite defects, resulting in p-type doped samples for predominantly Bi_{Te} defects or an n-type sample from Te_{Bi} defects [31]. Alloy studies of bulk crystals have shown that Bi_2Te_2Se samples naturally deter these two defect types from forming, resulting in the lowest doping density of any of the alloys. Since the Se-Bi bond is stronger than the Te-Bi bond, selenium preferentially inhabits the center of the quintuple layer which reduces its ability to escape and leave a vacancy. Additionally, the strong Se-Bi bond prevents the formation of Bi-Te antisite defects. [32,33] The preferential Te-Bi-Se-Bi-Te QL structure has been confirmed via transmission electron microscopy.

Table 2.1 Lattice constants and bandgaps of Bi_2Se_3, Bi_2Te_3, and In_2Se_3.

	a/b (nm)	c (nm)	QL (nm)	Bandgap (eV)
Bi_2Se_3	0.41	2.87	0.96	0.35
Bi_2Te_3	0.44	3.05	1.02	0.21
In_2Se_3	0.40	2.88	0.96	~1.5*

*The literature has not yet reached a consensus on the exact value, however for this work behavior of In_2Se_3 as a trivial insulator is of more importance than the precise bandgap value.

2.2.3 In_2Se_3

In MBE it is useful to find materials with common crystal structures and lattice constants, yet different electronic properties. For the bismuth chalcogenide TI family In_2Se_3 serves this purpose. In_2Se_3 is a trivial insulator whose α-phase has the same van der Waals structure as Bi_2Se_3 and Bi_2Te_3. While MBE growth of pure In_2Se_3 is difficult due to its polymorphic nature, alloying in bismuth forces the crystal into the correct phase. $(Bi_{1-x}In_x)_2Se_3$ has been shown to be a trivial insulator for $x \geq 0.3$ so alloys with a high bismuth content can be used to create heterostructures without worrying that excessive Indium will diffuse into the TI layers [34]. Creating heterostructures of TIs and trivial insulators will allow for the observation of multiple interacting TSS.

2.3 Plasmons

2.3.1 Plasmons background

Plasmons excitations resulting from the coupling of photons and free electrons. Depending on the material and physical properties of the system different types of

plasmon resonances can be observed. Each plasmon type will have a unique dispersion relation that determines the plasmons' oscillation frequency.

$$k_x = \frac{\omega}{c}\sqrt{\left(\frac{\varepsilon_1\varepsilon_2}{\varepsilon_1+\varepsilon_2}\right)} \quad (2.3)$$

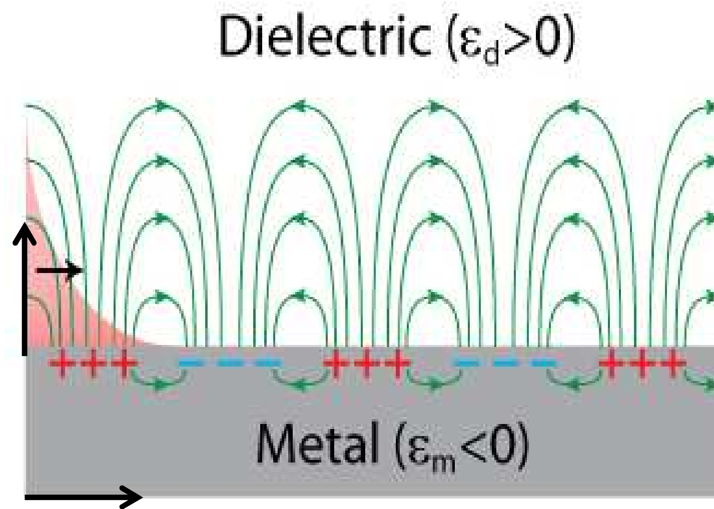

Figure 2.8 The oscillation of electrons and resulting electric field of a surface plasmon polariton.

The simplest plasmons to discuss are surface plasmons polaritons (SPPs) which occur at interfaces between dielectric-like and metal-like materials. Polaritons are the strong coupling of light with a dipole carrying excitation, in this case the surface plasmons. When light of the correct frequency impinges on the surface the free electrons will collectively oscillate in resonance with it, creating a new quasiparticle [1]. SPPs can propagate along the interface and create an enhanced electric field that decays exponentially perpendicular to the surface, as can be seen in Figure 2.8. Equation 2.3 gives the dispersion relation for a wave propagating along a surface where k_x is the wavevector in the propagation direction, ω is the frequency, *c* is the

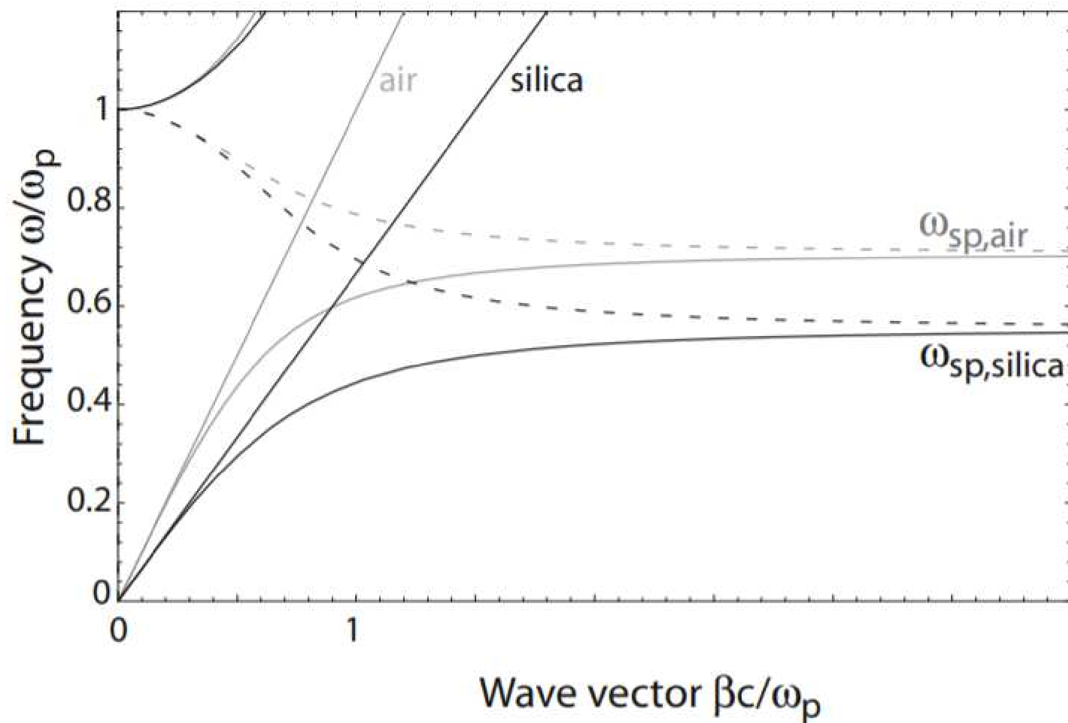

Figure 2.9 The dispersion of a plasmon at the interface between a metal and air, as well as a metal and a silica prism.[35]

speed of light, and ε_1 and ε_2 are the permittivities of the metal and the dielectric. The dependence of confinement on the permittivities of both materials means that material selection is critical to determining the behavior. For the visual spectrum traditional metals may be used, however in the THz region the permittivity of the metals is so large that Equation 2.3 simplifies to $k_x = \frac{\omega}{c}$ and the light is not usefully confined (assuming an interface with air, ε_2-1). Thus, novel materials must be used for THz applications. Additionally, the momentum of the plasmon will always be larger than that of the light that excites it. Momentum must be added to the incoming light via a prism or grating in order to excite the plasmon, as shown in Figure 2.9 [35].

If the thin film is much thinner than the excitation wavelength, the SPPs on each surface will couple together. Coupled plasmons result from the enhanced electric

fields created at each surface overlapping and forming two distinct modes. In the optical mode, the charge density waves propagating along two interfaces are in phase with each other resulting in an even greater enhancement of the electric field. In the case of the acoustic plasmons, the waves are in antiphase. As is suggested by the name only the optical mode is optically active and observable via spectroscopic methods [35].

Should further confinement be introduced, for instance by patterning the film into subwavelength gratings or nanoparticles, the plasmon can no longer propagate along the surface. Instead a localized surface plasmon (LSP) will be excited, as shown in Figure 2.10. When an LSP is excited the free electrons migrate to one side of the particle, creating a buildup of positive charge on the opposite side. This creates a restorative force resulting in the electrons oscillating from one side of the particle to the other. The frequency of this LSP oscillation is dependent on the effective mass of the electron, the size and shape of the particle, and the charge carrier density [36].

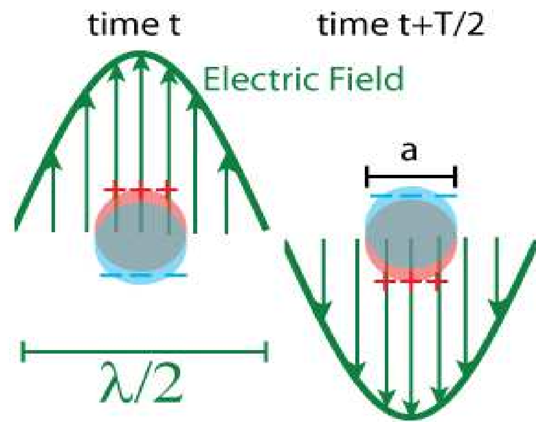

Figure 2.10 The time resolved oscillation of electrons and resulting electric field of a localized surface plasmon.

2.3.2 Plasmons in Topological Insulators

Plasmons excited in the surface state of topological insulator are quite unique as they inherit the behaviors of their constituent electrons. This means that a TSS

plasmon will be massless and spin polarized with long propagation distances. TSS

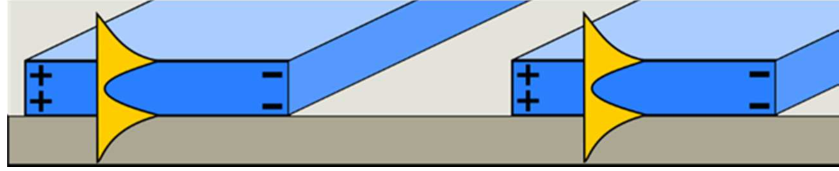

Figure 2.11 A schematic of coupled Dirac plasmons showing the induced electric field (yellow) at both surfaces of the topological insulator (blue). Reproduced with permission from [113]

plasmons could open the door to spin computing technology as they provide long range, coherent, and controllable movement of spin not found in many other systems. Plasmons in TSS are also useful as their frequencies are in the Terahertz (THz) range. THz falls between the infrared and microwave ranges (~3 mm to 30 μm) and has a wide range of applications including toxic gas sensing, airport security, and space observation. However, THz is currently a difficult range to work in as sensor and emitter technologies are very inefficient. Functional plasmonic materials in the THz would be immensely helpful in making this frequency range more accessible. The plasmonic materials discussed in this thesis are patterned out of Bi_2Se_3 films 50-200nm thick. In the THz these thicknesses are very subwavelength so the plasmons excited on each surface will couple together resulting in a coupled 2D Dirac plasmon as seen in Figure 2.11.

$$\omega_p^2 = \frac{e^2}{4\varepsilon_0\varepsilon_r}\frac{n_M}{m^*}q \quad (2.3)$$

$$\omega_p^2 = \frac{e^2}{\varepsilon_0}\frac{v_F\sqrt{2\pi n_D}}{h}\frac{q}{\varepsilon_T+\varepsilon_B+qd\varepsilon_{TI}} \quad (2.4)$$

The inherently 3D nature of Bi_2Se_3 allows for the existence of at least two carrier pathways beyond the TSS: bulk doping and a band bending 2D electron gas (2DEG) at the interface of the TI and adjacent material. [37] One way to distinguish Dirac plasmons from co-existing massive bulk plasmons and massive 2DEG plasmons

is by mapping how the plasmon frequency depends on film thickness as well as stripe width, Figure 2.12. Equation (2.3) shows the dispersion relation for massive bulk plasmons, where w_p is the plasmon frequency, e is the electron charge, n_M is the 2D sheet density, e_r is the average permittivity of the surrounding materials, and q is the wavevector of light. For massive bulk plasmons, n_M will increase as the film thickness increases (assuming the bulk, 3D carrier density is constant), [38] resulting in an increase of the plasmon frequency. In the case of band-bending 2DEG plasmons, the film thickness will have no effect on plasmon frequency since n_M for a 2DEG will be independent of film thickness. Finally, Equation (2.4) shows the dispersion relation for coupled 2D Dirac plasmons. [39] Here v_F is the Fermi velocity, n_D the 2D Dirac carrier density, d is film thickness, and $e_{T,}$ $e_{B,}$ e_{TI} are the permittivities above, below, and inside the TI respectively; in this case e_T is 1 and the equations for e_B and e_{TI} are given in the following references and in the supporting information. [40,41] For coupled 2D Dirac

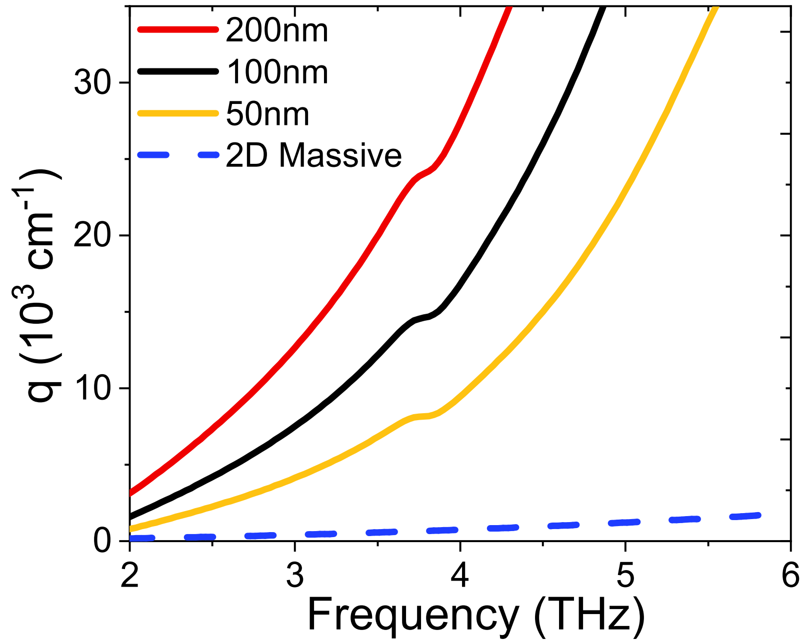

Figure 2.12 The theoretical dispersion relations of a 2D massive plasmon (dotted line) and 2D couple Dirac Plasmons with varying film thicknesses (solid lines). A 2D carrier density of $n_s = 2.38 \times 10^{13}$ cm^{-2} was used for the calculation.

plasmons, the plasmon frequency will increase with film thickness but at a much slower rate than 2D massive plasmons. Thus, by mapping the plasmon frequency as a function of both wavevector and film thickness, we can distinguish all three types of plasmons. Demonstrating the presence of an excited Dirac plasmon is the first step towards functional devices that take advantage its unique behaviors.

Chapter 3

METHODS

Modern science has been made possible in large part by the myriad of techniques and technologies that have been invented over the course of scientific pursuit. These technologies allow for the creation of improved samples, the measurements of minuscule features or obscured properties, and the creation of devices and features well beyond the limits of unaided human ability. This chapter will explore the growth, characterization, and fabrication technologies that made the research discussed in this thesis possible. While many scientific instruments can be operated as a “black box”, understanding their underlying science and inner workings is vital to correctly interpreting data, designing meaningful and efficient experiments, and problem solving when something inevitably goes wrong.

3.1 Growth

3.1.1 Molecular Beam Epitaxy

The topological insulator thin films discussed in this thesis are grown through Molecular Beam Epitaxy (MBE) conducted in a dedicated Veeco GENxplor reactor, part of the University of Delaware Material Growth Facility. MBE is an ultrahigh vacuum method (usually between 10^{-8}-10^{-10} Torr) for producing high quality crystalline thin films on a desired substrate [42]. Molecular beam refers to the path of source material molecules in the growth chamber: the ultrahigh vacuum environment

allows them to travel unimpeded in a direct beam towards the growth surface. The word epitaxy is Greek in origin and breaks down into epi meaning 'upon' and 'taxis' meaning arrangement. Epitaxy can therefore be understood as the *arrangement* of atoms *upon* a substrate, the crystal structure of the substrate informing the placement of the adatoms [43]. MBE is a relatively simple idea, however many technologies and mechanisms must all work in tandem in order to produce successful results.

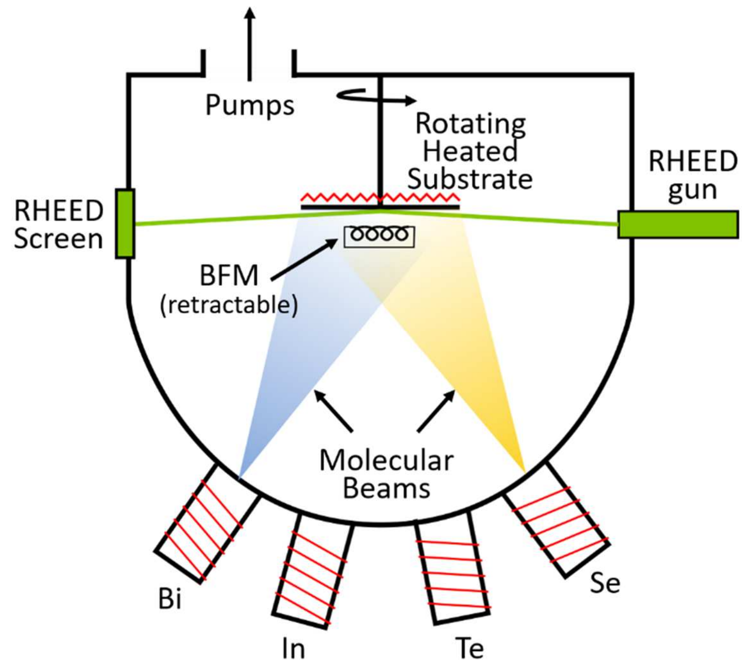

Figure 3.1 A schematic of an MBE chamber.

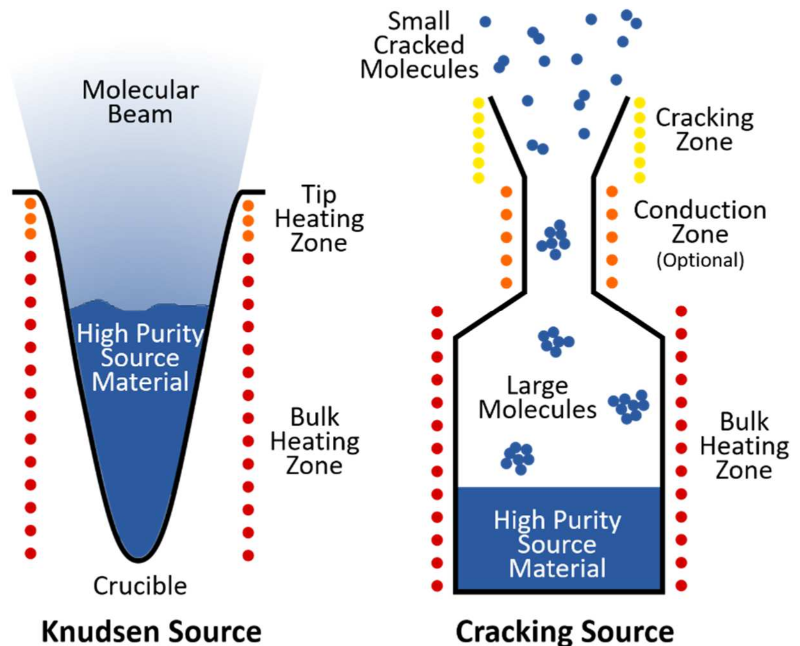

Figure 3.2 Schematics of (left) a traditional Knudsen effusion cell with the outgassing molecules depicted as molecular beam and (right) a cracker cell with the outgassing molecules depicted as clusters of atoms.

Extremely high purity source material

(in this case bismuth, indium, selenium, and tellurium) is loaded into individual effusion cells (crucibles surrounded by heating elements). As the sources are heated with pricelessly controlled heating zones, the source material starts to outgas creating a beam of molecules directed towards the growth substrate as shown in Figure 3.2.a. In a standard Knudsen type cell, a bulk heating zone is used to control the flux of the material while a shutter controls whether or not the substrate is exposed to the molecular beam. A tip heating zone, kept hotter than the bulk, is often used to stop material condensing around the mouth of the source. Elements like selenium and tellurium outgas from the bulk source as large molecules with low reactivity which must then be broken apart at the growth surface to be incorporated into the film. This is an inefficient process which requires large fluxes and can lead to vacancy defects [33]. Alternatively, a cracking source can be used to break apart the large molecules before they reach the growth surface. Cracker sources have a bulk heating zone that controls the flux of the material, as well as a second heating zone, called the cracking zone, that is kept much hotter (~900-1100 °C) to thermally break apart the large selenium molecules into monatomic and diatomic molecules [44]. Some cracking sources include a third heating zone, called the conductance zone, to ease the thermal gradient between the bulk and cracking zones. As discussed in a later chapter, using cracking sources for selenium while growing Bi_2Se_3 is much more efficient than a traditional source and allows for a three to four times smaller Selenium to Bismuth ratio to be used [45–47]. For larger sources (200cc or more) the large thermal mass of the source material makes flux control via temperature change impractical. In these cases, a valve may be used to provide fine control of the flux while the bulk temperature provides coarse control.

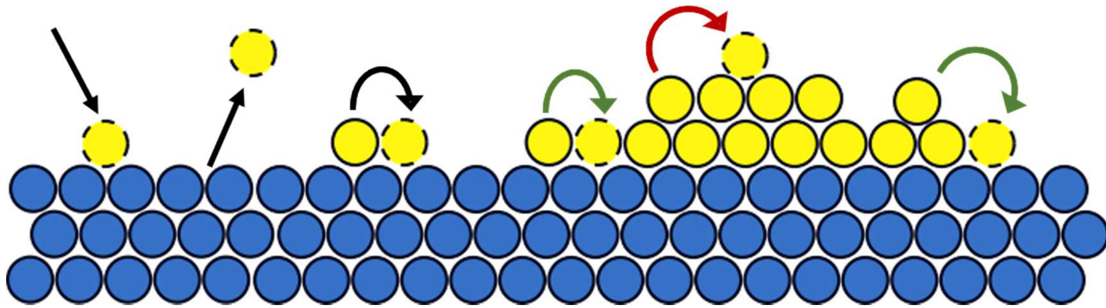

Figure 3.3 A diagram of behaviors at the growth surface. From left to right: impinging atom, evaporation, hopping between equal sites, hopping to a step edge, hopping up a step edge, and hoping down a step edge. Black arrows represent behaviors who rate is primarily dependent on substrate temperature and source flux, green arrows represent typically energetically favorable moves, and the red arrow represent a move that is generally unfavorable. Blue circles represent stylized substrate atoms and yellow circles represent adatoms.

Once the molecules leave the sources the low-pressure environment of the growth chamber ensures that they have a long mean free path, the distance a particle can travel without collision. At room temperature and a pressure of ~10^{-9} torr, a molecule will have a mean free path of tens to hundreds of kilometers, meaning molecules are likely to impinge upon the growth surface (or chamber walls) long before they collide with another molecule. The lack of scattering during the particle's travel is what creates the beam-like behavior of the source molecules [43]. An ion gauge called a beam flux monitor (BFM) can be used to quantify the flux of each molecular beam in order to determine appropriate growth conditions. The BFM is extended into the growth chamber just below the growth surface in the path of the beam, then the source shutter is then opened for 60sec and closed for 60sec and the BFM value is recorded at the end of each minute. The 'closed' value is subtracted from the 'open' value to determine the beam equivalent pressure (BEP) of the source. In our studies four BEP readings are taken and averaged for each source. Due to the differing ionization energy of different elements BEP measurements do not give an

exact flux, however they should be relatively consistent in individual chambers. Once BEP measurements are concluded the BFM is retracted out of the way of the growth.

When the source molecules impinge upon the surface their behavior is controlled by adatom-surface and adatom-adatom interaction strengths. An atom sitting on a crystalline substrate will inhabit a low energy absorption site, the atom can hop from site to site, but it requires energy to do so. The adatoms' ability to diffuse across the surface is called the adatom mobility. It can be helpful to think of adatom mobility in terms of how many bonds the adatom is able to satisfy at each site. On a totally flat surface hopping from site to site does not change the number of interacting neighbors so each site is equally energetically favorable. If the adatom encounters a step edge, sitting at the step edge will allow it to satisfy more bonds at once. Similarly, hopping down a steep increases the amount of satisfied bonds and is therefore energetically favorable while hopping up a step to form a new layer result in fewer bonds and is energetically unfavorable [48]. Increasing the substrate temperature increases the energy of the adatoms and improves adatom mobility. However, if the substrate temperature is too high, re-evaporation from the growth surfaces increases and thermal degradation of the film is possible. In our samples, bismuth and indium control the growth rate and it is their adatom mobility that dominates the growth behavior. Increasing the flux of selenium and tellurium generally increases the adatom mobility of bismuth and indium. While this explanation is true in the most basic MBE growth, it is possible to push the growth into more exotic morphologies by introducing complications like lattice mismatch or weakly interacting substrates. Self-assembled quantum dot, nanowires, nanotubes, and more are all possible via MBE given the correct material and clever manipulation of the growth parameters.

By controlling the substrate temperature and the flux ratios of the sources, it is possible to tailor growth parameters for the desired material. Some materials have very narrow growth windows and finding the right parameters is often quite a lengthy process. In traditional MBE, the growth is considered epitaxial because the growing film uses the substrate's crystal structure to organize itself. This means that careful consideration must be paid to crystal structure compatibility and lattice matching. However, as bismuth chalcogenide topological insulators are van der Waals materials, we can take advantage of the weak substrate-film interaction and can grow on a wide variety of substrates. MBE growth is advantageous to other growth methods for many reasons including its ability to produce single crystal films with very few defects or impurities and its ability to grow layered heterostructures. While the slow growth rates used in MBE (1nm-1μm) a minute allow for impressive control over crystal quality, layer thickness, and interface smoothness they can pose an impediment to scalability for manufacturing. MBE is also an expensive growth method, requiring specialized equipment, expensive source materials and substrates, and lengthy user training periods. MBE is best suited to commercial applications where material quality is more important that cost or time considerations.

3.1.2 Reflective High Energy Electron Diffraction

During growth, film quality is monitored in real time using reflective high energy electron diffraction (RHEED). In RHEED a beam of high energy electrons is diffracted off the growth surface at a glancing angle. Electrons that diffract at the correct angles will interfere constructively to produce the RHEED pattern as they strike a phosphorescent screen. An Ewald sphere, as seen in Figure 3.4.a [49] can be used to determine these diffraction angles. An imaginary sphere whose radius is equal to the reciprocal wavelength of the incident electrons, $k_0=2\pi/\lambda$, is created on the reciprocal lattice of sample surface. When points on the reciprocal lattice intersect the Ewald sphere, the vector connecting the center of the sphere to the intersection point will be equal in magnitude to k_0 and the diffraction conditions are met, Figure 3.4.b [50]. Points of intersection between the Ewald sphere and the reciprocal lattice are projected as a two dimensional pattern onto the RHEED screen. For a perfect 2D crystalline sample the reciprocal lattice is a series of infinite rods, which would appear as a series of dots on the RHEED screen. However, in real samples, domain size and surface roughness interfere with long range order and cause the dots to smear into vertical lines. Generally, a pattern of lines is considered desirable for flat single crystal

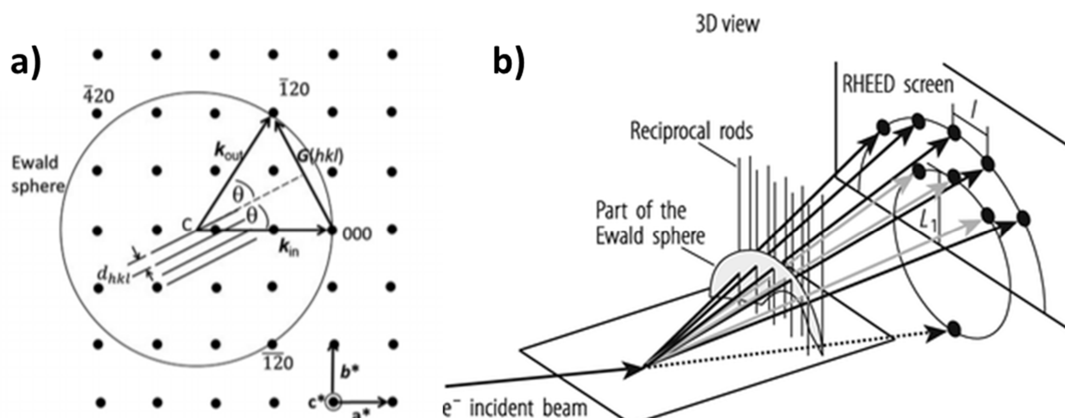

Figure 3.4 RHEED diffraction geometry and construction of the Ewald sphere. Part a reproduced with permission from [49]. [50]

MBE growth, with sharper lines indicating increased long-range order. In polycrystalline growth, the lattice constant remains the same between grains but the orientation changes. This results in a series of rings, as if the dots from the "perfect" RHEED pattern were rotated around a center axis to trace out the pattern (Figure 3.5.b). An amorphous sample will scatter the RHEED beam and produce a vague glow instead of a coherent pattern. If growth conditions create 3D features, the reciprocal lattice of the 3D crystal must be constructed instead of the 2D surface. As the reciprocal lattice becomes more intricate so does the resulting RHEED pattern; chevrons (Figure 3.5.c) or complex patterns of dots (Figure 3.5.d) are possible depending on the exact morphology of the surface. Paying close attention to how a RHEED pattern evolves during growth and understanding the cause of different patterns, can allow MBE growers to optimize parameters during growth and to understand what growth mechanism may be at play.

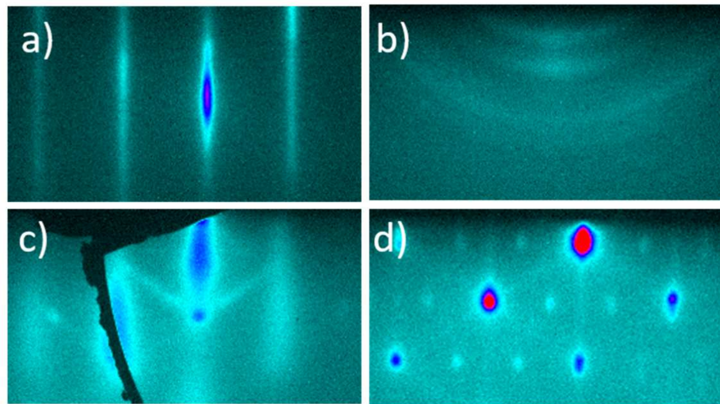

Figure 3.5 Example RHEED patterns for a) single crystal, b) polycrystalline, and c,d) 3D growth.

3.2 Characterization

3.2.1 Hall

Once grown, Hall Effect Voltage and van der Pauw resistivity measurements are performed to determine the electrical properties of the films. Both techniques require a square sample with an electrical contact on each corner as shown in Figure 3.6We use indium applied with a soldering iron to create our contacts. During Hall effect, the film is subjected to an external magnetic field while a current is applied diagonally across the sample (contacts 1 & 3). In the presence of a magnetic field, the charge carriers travel in a curved path and accumulate along the edge of the sample. The resulting Hall voltage is then measured between the two remaining contacts (contacts 2 & 4). The Hall measurement is conducted multiple times, swapping which contacts are used for current and voltage in order to eliminate any anisotropic effects [23]. In van der Pauw measurements a current is applied between two adjacent contacts (1&2) and the resulting voltage is measured between the two remaining corners (3&4) [51]. The resistance can then be calculated using $R_{12,34}=V_{34}/I_{12}$. The sheet resistivity, ρ, of the sample can be calculated using two different R values and the van der Pauw formula:

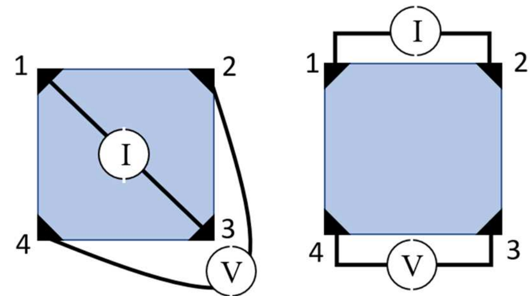

Figure 3.6 A schematic of the measurement set up Hall (left) and van der Pauw (right) measurements.

$$e^{-\pi R_{12,34}/\rho} + e^{-\pi R_{23,41}/\rho} = 1 \quad (3.1)$$

Using the results from these measurements it is possible to calculate the majority carrier mobility μ using:

$$\mu H = \frac{|V_h t|}{BI\rho} \quad (3.2)$$

where V_h is the Hall voltage, t is the sample thickness, B is the applied magnetic field and, I is the current used in the Hall measurement. The carrier concentration, n, can then be calculated using:

$$\rho = \frac{1}{qn\mu} \quad (3.3)$$

where q is the electron charge [23]. These measurements are extremely quick, require minimal preparation, are nondestructive to the majority of the film, and can be conducted in atmospheric conditions at room temperature, making them an ideal gauge for film quality. When comparing electrical properties to literature values, it is important to note at what temperature the measurements were taken. Low temperature Hall tends to produce higher mobilities as phonons are frozen out, however room temperature properties are important for device applications.

3.2.2 Atomic Force Microscopy

Atomic force microscopy (AFM) is a method of imaging the surface morphology by rastering a very fine-tipped cantilever across the surface of the film, Figure 3.9 [52]. In tapping mode, the tip is repeatedly brought into close proximity with the sample.

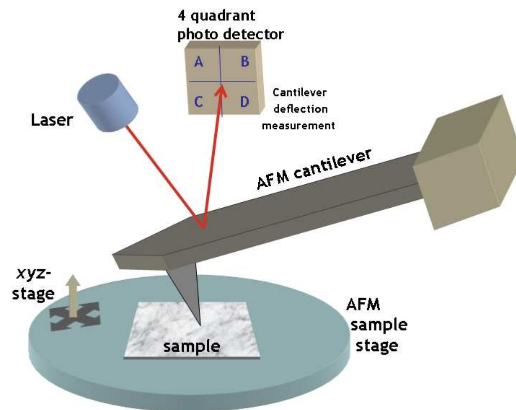

Figure 3.7 A schematic of an AFM set up. Reproduced with thanks to Opensource Handbook of Nanoscience and Nanotechnology CC by 2.5 [52]

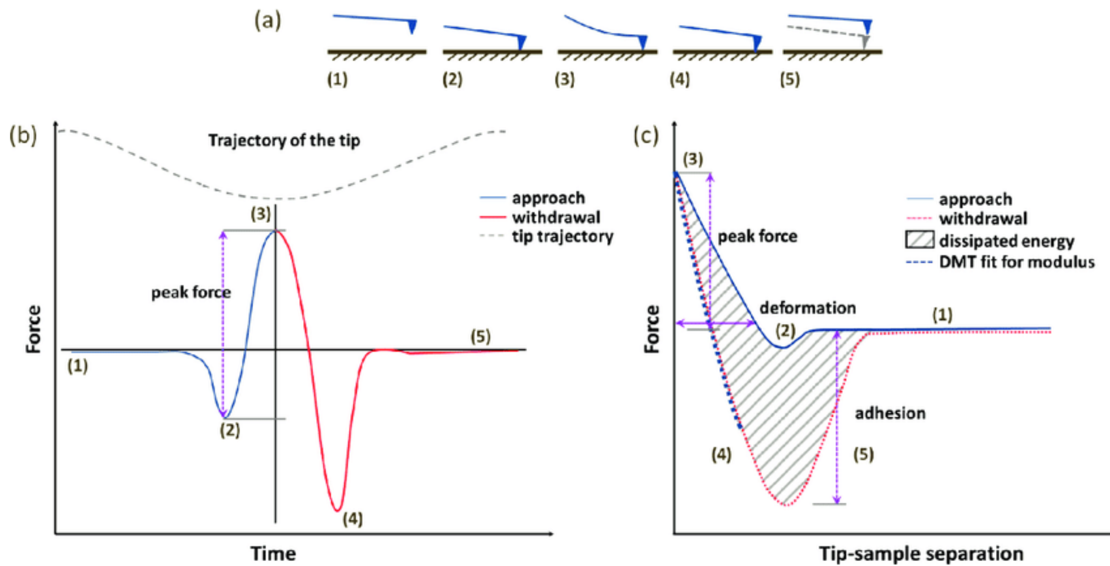

Figure 3.8 (a) Approach and withdrawal of the AFM-tip in a single tapping cycle (b) principle of Peak Force Tapping operation with the tip trajectory (c) schematic of force-distance curve obtained at each tapping cycle with the peak force as controlling parameter. [53]

Their interaction is measured via the displacement of a laser beam reflected off the back of the cantilever onto a position sensitive photodetector. As the tip approaches the sample surface, it will feel an initial attractive force which transitions into a repulsive force as the two are pushed closer together, Figure 3.11 [53]. As the tip is withdrawn the opposite is true, an initial repulsive force transitions into an attractive force. By using these forces to deflect the cantilever, it is possible to map out the sample surface topography without having to drag the tip across the sample surface. AFM can produce images with nanometer resolution in atmospheric conditions without the need for any special sample preparation. One disadvantage of AFM is its tendency towards artifacts: features that show up in scans but are not actually present on the surface. Extreme height differences, bad scan parameters or a tip defect can all produce artifacts that can be hard to distinguish from real features [54]. The AFM

measurements presented in this work were taken on a Dimension-3100 V SPM AFM, part of the Keck Center for Advances Microscopy & Microanalysis.

3.2.3 Scanning Electron Microscopy

Scanning Electron Microscopy (SEM) is method of imaging a surface with sub-nanometer resolution using a focused beam of electrons [55]. When electrons hit the sample, they can ionize atoms by causing them to release secondary electrons [56], SEM is thus dependent on the work function of the material. The secondary electrons are absorbed by a detector which uses a photomultiplier to improve the signal to noise ratio of the image. Since SEM uses electrons instead of light, magnetic lenses must be used to focus the beam onto the sample surface (Figure 3.10 [57]) instead of the optical lenses used in traditional microscopes. Despite requiring a low-pressure environment, SEM is an excellent technique for quickly imaging sample surfaces. However, due to the electron

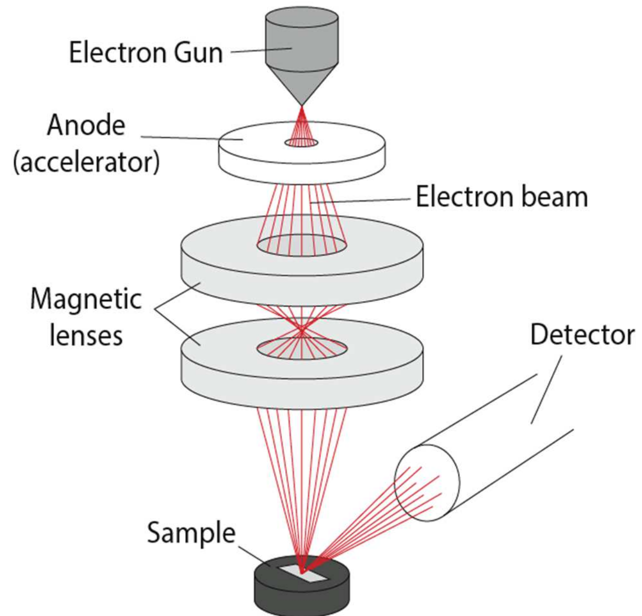

Figure 3.10 Diagram of the focusing components of an SEM. [57]

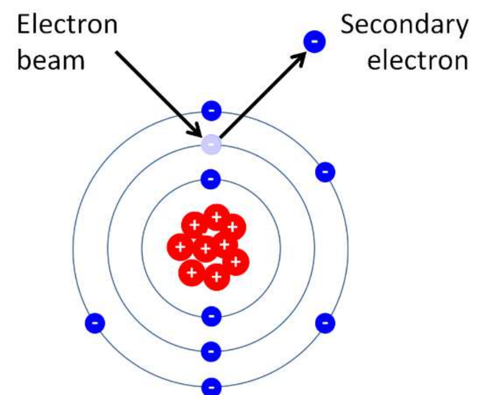

Figure 3.9 Generation of secondary electrons. CC by 4.0 [56]

beam's sensitivity to the electronic properties of the samples, conductivity can often be confounded with topography and so a complimentary surface imaging technique such as AFM should always be used to confirm results. Additionally, samples with low conductivity can experience charging effects which can obscure topographical features. The SEM used in the study is a Zeiss Merlin, part of the University of Delaware Nanofabrication Facility.

3.2.4 X-ray Diffraction

X-ray Diffraction (XRD) operated in a coupled theta – two theta scan mode is a useful technique for determining the composition and phase of the films and can provide insight into the crystal quality. In XRD, a beam of monochromatic Cu Kα1 x-rays is diffracted off the sample surface at a specific angle towards a detector. As the source and detector move through a range of diffraction angles, intensity peaks will appear when the x-rays diffract off lattice planes and interfere constructively with each other, Figure 3.11 [58]. Using Bragg's Law, $2dsin\theta = n\lambda$, the angle of diffraction can be used to determine the spacing between planes, d. [59] It is then possible to find the lattice constant of the crystal using the formula:

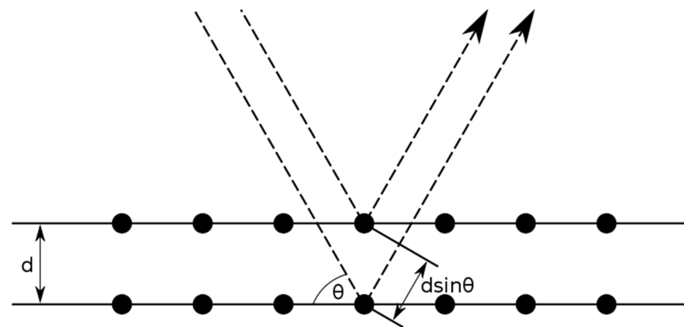

Figure 3.11 Reflection off of crystal planes that cause peaks in XRD patterns due to Bragg's Law. [58]

$$\frac{1}{d_{hkl}^2} = \frac{4}{3}\frac{h^2+hk+k^2}{a^2} + \frac{l^2}{c^2} \quad (3.4)$$

When alloying between two binary compounds, such as Bi_2Se_3 and In_2Se_3, Vegard's Law and XRD data can be used to provide a rough estimate of the film composition. Vegard's Law assumes that the lattice constant of an alloy changes linearly as it transitions from one binary to the other [60]. At higher angles the change in peak position between compounds becomes more exaggerated but XRD signal is decreased. When using Vegard's Law, it useful to pick the highest ordered peak possible while still maintaining a strong signal-to-noise ratio. The XRD presented in this thesis was taking using a Bruker D8 XRD, part of the Advanced Materials Characterization Lab.

3.2.5 Fourier Transform Infrared Spectroscopy

The terahertz (THz) optical properties of the samples are of interest in certain parts of this study. To determine the THz extinction spectra of our samples we use a technique called Fourier Transform Infrared Spectroscopy (FTIR). In this technique, a broadband source of terahertz light is sent through a Michelson interferometer as shown in Figure 3.12 [61]. The light is directed onto a beam splitter

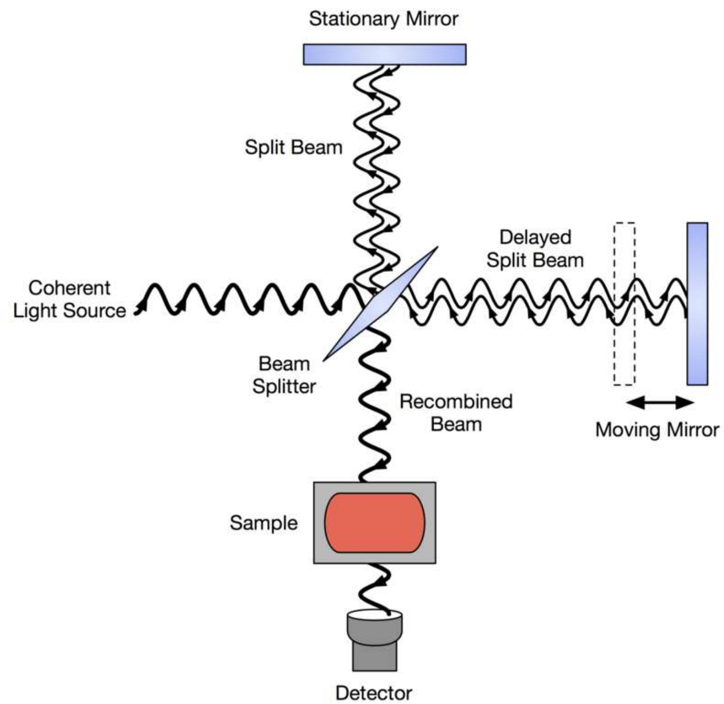

Figure 3.12 A diagram of a Michelson interferometer.[61]

which reflects half the light onto a stationary mirror and allows the remaining light to pass through onto a moving mirror. After reflecting off their respective mirrors, the beams recombine at the beam splitter and interfere with each constructively or destructively depending on the difference in the pathlength created by the moving mirror. The intensity modulation caused by the interference will change at different rates for individual wavelengths contained in the broad-spectrum light, resulting in a unique spectrum corresponding to each mirror position. This light is then sent through the sample (transmission mode) or reflected off the sample (reflection mode) and into a detector for analysis [62].

The raw data collected by the detector is called an interferogram and is in the form of intensity vs. mirror position. To convert this data into a more informative form, we use a mathematical process called a Fourier transform, which converts one domain into its inverse domain. For example, audio speakers use Fourier transforms to convert multiple frequencies into a single diaphragm displacement position for a given instant in a song. This is directly analogous to the multiple wavelengths created by a given mirror position being represented by a single intensity value. Using a Fourier transform, we can convert intensity vs mirror position to intensity vs wavelength. To differentiate the behavior of the films and the behavior of the substrate, scans are taken of a corresponding bare substrate for use in background correction. In transmission mode it is only possible to study samples grown on substrates with a reasonable degree of transmission in the desired frequency range. To calculate the final extinction (E) spectra, we use the formula $E=1-T/B$, were T is transmission through the sample and B is the background scan [62].

Operating in the THz requires specialized FTIR components designed to work in this difficult frequency range. A deuterated triglycine sulfate (DTGS) detector is used for its THz responsiveness. DTGS is a slow detector by FTIR standards, however it does not need to be cooled with liquid nitrogen. The beam splitter used is a proprietary polymer designed for wide range use across the IR and THz wavelengths, and the broadband THz source is a glowbar. It is exceedingly important to take these measurements under vacuum as THz radiation is readily absorbed by water vapor. The FITR used in this thesis is a Bruker VERTEX 70v situated on a floating table to reduce vibrational interference.

3.3 Fabrication

The plasmonic section of this thesis necessitated the patterning of samples with features 1-4μm in size. Creating such small features required the use of lithography done in a class 100 cleanroom. A thin coat of a photosensitive polymer called photoresist is spun onto the samples surface then baked on a hot plate to drive out most of the solvent. When the photoresist is exposed to ultraviolet (UV) light, the polymer will photodecompose and become soluable, so lithography bays in cleanrooms use yellow tinted overhead light to avoid accidental UV exposure. Placing a chrome mask with the desired pattern over the film allows for the selective photodecomposition of undesired areas [63]. It is vital to ensure good contact between the mask and photoresist layer before exposure in order to provide the best possible feature resolution. After exposure, a chemical developer is used to dissolve away the soluble photodecomposed areas, leaving behind the desired pattern in photoresist. There also exist negative photoresists that crosslink under UV exposure. With these resists, the exposed section will remain while the unexposed section is rinsed away

with developer. UV-lithography does not have the resolution for sub-micron feature sizes so instead e-beam lithography must be used. The process is very similar except that a beam of electrons is used to draw the pattern into the photoresist instead of using a mask [64].

Once the resist is patterned, the samples are placed in an ion mill to transfer the pattern to the film. In the ion mill, the sample surface is bombarded with argon ions that physically knock atoms off the surface. Partially due to their van der Waals nature, our films mill much faster than the photoresist, so the exposed areas can be completely milled way while the covered areas will remain protected. After the films have been milled the remaining photoresist can be removed in a bath of hot N-Methyl-2-Pyrrolidone. Once the photoresist has been applied, it is important to work in a timely manner as the longer photoresist stays on a sample the harder it is to remove. All work should ideally be completed and the photoresist removed within 2-3 days.

Chapter 4

THE GROWTH OF HIGH-QUALITY BISMUTH SELENIDE USING A SELENIUM CRACKER SOURCE

4.1 Introduction

The first step in producing quality scientific results is being able to produce high quality material to study. Therefore, the first step in studying any MBE grown films is to optimize the growth recipe. The initial material chosen to grow on the newly installed MBE system was Bi_2Se_3. As previously stated Bi_2Se_3 is a well-known topological insulator whose prevalence in literature and binary nature should assist in easily finding the optimal growth parameters. In this chapter growth of Bi_2Se_3 using a selenium cracker source on both Si(111) and sapphire substrates will be discussed. The selenium cracker is expected to improve selenium incorporation into the films during growth, resulting in films with improved electrical properties. The effect of selenium flux during growth on the films, as well as the relationship between surface morphology and electrical properties, will be explored. Work in this chapter was published in Ginley et al. [38]

An ideal TI film has a completely insulating bulk with all the charge carriers inhabiting the TI surface states, resulting in films with high electron mobilities and low carrier densities. However, MBE grown thin films of Bi_2Se_3 tend to be significantly n-type doped, partially due to selenium vacancies and antisite

defects [33]. Bi_2Se_3 thin films also traditionally show significant sensitivity to water vapor and ageing effects upon exposure to air as adatoms attach to the surface and oxygen molecules diffuse in the film [65]. These ageing effects add to the bulk carrier density and serve to obscure the behavior of the TI surface states and making the films ill-suited to device applications. Efforts to improve the quality of MBE grown Bi_2Se_3 thin films for optical or electronic applications mainly focus reducing the carrier density of the films. In this work we aim to improve selenium incorporation during growth to reduce selenium vacancies and thus reduce the overall carrier density.

4.2 Growth

In MBE grown Bi_2Se_3 the growth rate is controlled by the bismuth flux and a large selenium over pressure is used to ensure adequate incorporation and to prevent selenium atoms from outgassing during growth or cooling. Using a traditional Knudsen-type effusion cell for the selenium source, with only bulk and tip heating zones, Se:Bi ratios can be as high as 200:1 [45,46,66–69], measured via beam equivalent pressures. In these sources selenium evaporates as large molecules (Se_6, Se_7, Se_8…) and must be thermally cracked at the growth surface in order to be incorporated [70]. The flux ratios are measured by beam equivalent pressure, as discussed in chapter 3, and so provide a useful tool for recipe creation rather than an exact measure of comparative fluxes. Since Bi_2Se_3 is grown at relatively low temperatures (300°C) the growth surface does not provide much energy to break apart the large selenium molecules. The cracking process is thus highly inefficient and likely the cause of some bulk doping even at large Se:Bi ratios. In a cracking source the large selenium molecules evaporating from the bulk pass through a cracking zone held at 900°C where they thermally break apart into smaller molecules (believed to be

Se, Se_2, Se_3) well before impinging on the growth surface. This allows for much more efficient incorporation into the film and lower selenium fluxes can be used to achieve comparable results. All selenium containing films discussed in this thesis were grown using a cracked selenium source.

Initially, growths of Bi_2Se_3 were attempted on Si(111) substrates. To remove the native oxide a Hydrogen Fluoride etch was used and samples were immediately placed in the load lock of the MBE. Samples were heated to 200°C for 12 hours to remove any water vapor. Then samples were transferred into the growth chamber and heated to 650°C to remove any remaining surface contamination. Despite varying the substrate temperature during growth, the Se:Bi flux ratios, and the growth rate, growths on Si(111) remained low quality and polycrystalline as indicated by a ring pattern in the RHEED and the diffuse appearance of the films upon removal from the MBE. It was determined that the complex nature of the substrate surface after the removal of the oxide was complicating the growth dynamic and a more inert substrate would be better suited for initial growth exploration. Switching to growth on Sapphire substrates immediately produced films of a high enough quality that the growth phase space could be meaningfully explored. All films discussed in the remainder of this chapter were grown on sapphire substrates using a growth rate of ~1nm/min and the same bake out procedure as the Si(111) substrates (200°C in the load lock for 12hrs and 650°C in the growth chamber).

4.3 Electrical Properties

The phase space parameters explored in this study are Se:Bi flux ratios as determined by beam equivalent pressures and substrate temperature during growth as determined by thermocouple. Figure 4.1 [38] reports the mobility and sheet carrier

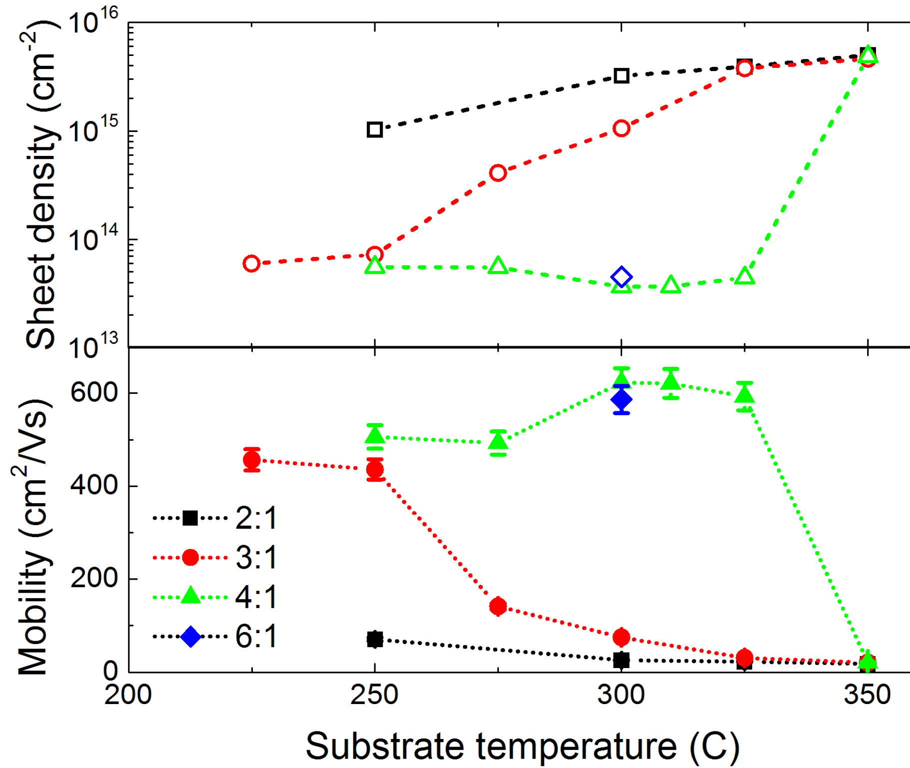

Figure 4.1 Room temperature sheet density (open symbols) and mobility (closed symbols) as a function of substrate temperature for Bi2Se3 films grown with Se:Bi ratios of 2:1 (black squares), 3:1 (red circles), 4:1 (green triangles), and 6:1 (blue diamonds). The lines are a guide to the eye. For all sheet density and some mobility measurements, the error bars are smaller than the size of the symbols and are not visible on this plot. Reproduced with permission from [38]

densities of a series of 100nm films grown spanning this phase space. An ideal film will have a high mobility and a low sheet carrier density, signifying that most of its' carriers are in the surface states instead of the bulk. At a flux ratio of 2:1, denoted by the black squares, mobility remained low (<100 cm^2/Vs) and the sheet carrier density remained high (>10^{15} cm^{-2}) regardless of growth temperature. We attribute this to selenium vacancies induced in the film due to the low Se:Bi flux ratio. This interpretation is supported by the fact that, as the growth temperature is lowered, the

film properties improve slightly. At lower growth temperatures, selenium re-evaporation is reduced, and fewer selenium vacancies are expected.

For films grown with a Se:Bi ratio of 3:1, we see some reduction in the sheet density and improvement in the mobility. Specifically, as the substrate temperature is lowered, the sheet density decreases and the mobility increases, with the best values found at a substrate temperature of 225°C. Because the electrical properties were beginning to plateau, lower substrate temperatures were not investigated. These data again support the theory that selenium vacancies are dominant force contributing to the electrical properties.

For a 4:1 flux ratio, the best electrical properties were obtained using a substrate temperature of 300°C, where we observed a room temperature sheet density of $3.32 \pm 0.2 \times 10^{13}$ cm^{-2} and a corresponding mobility of 623 ± 30 cm^2/Vs. Substrate temperatures up to 330°C resulted in similar electrical properties, indicating that this is a stable set of growth parameters. A high flux ratio of 6:1 was tried and gave the same electrical results as the 4:1 attempt, to within error bars so it was determined that further increasing the selenium flux would yield no significant improvement in film quality.

Insufficient selenium incorporation dominates the growth quality in the low selenium limit, however once a sufficient flux is reached adatom mobility starts to play a dominate role. This is evidence by the appearance of a growth window from 300-330°C at a flux ratio of 4:1. Here low temperatures result in a worsening of electrical properties, contrary to films grown at lower fluxes. This can be explained by the reduction in adatom mobility at lower temperatures leading to larger defect densities. At 350°C the electrical properties completely degrade for all flux ratios

indicating that Bi_2Se_3 thermally decomposes at this temperature. Based on this search through parameter space, we designated a substrate temperature of 300°C and a 4:1 flux ratio as our optimal growth conditions, and all subsequent growths discussed in this chapter were done using this recipe.

Films with a variety of thicknesses were grown using our optimized recipe. Sheet density for films between 10nm and 100nm remained constant at ~3x10^{13} cm^{-2} to within error bars, which indicates that the conductivity is dominated by two-dimensional channels. While constant across film thickness, our reported sheet density is still much higher than ~5x10^{12} cm^{-2}, the estimated sheet density for two topological surface states and an insulating bulk. These extra carriers can be explained by a disordered layer at the substrate interface that will be discussed in a later chapter. Temperature-dependent Hall measurements were taken on the best film, down to 40K (the minimum temperature available in our Hall system). The sheet density remained constant across the temperature range, while the mobility increased, reaching a maximum value of 925±46 cm^2/Vs at 40K.

To investigate the effects of ageing on our samples, Hall measurements were also performed as a function of time, as shown in Figure 4.2. Two thin samples (10nm and 20nm) were chosen for this study, as these were expected to be the most sensitive to ageing. The first data point was taken immediately upon removing the samples from the MBE chamber, while the second data point was taken one day later. There is a sharp decrease in mobility between these two data points, likely due to adsorbates on the surface, causing increased scattering of the surface states [71]. Over the two-month measurement period, the mobility continues to decrease slowly with time. Notably, the doping density always remains constant, to within experimental error.

This is in contradiction to other studies, in which the doping density evolved with time [72]. These evolutions have been attributed both to an increase in selenium vacancies as selenium out-diffuses, an increase in oxygen impurities as oxygen substitutes for the missing selenium atoms, and doping due to the surface reacting with water in the atmosphere [65]. We attribute our results to the use of the selenium cracker resulting in a film with fewer selenium vacancies and a carrier density which is stable upon exposure to atmosphere. Stability over time after exposure to the atmosphere is a key feature in the creation of reliable sensors, one of the potential device applications for this material system.

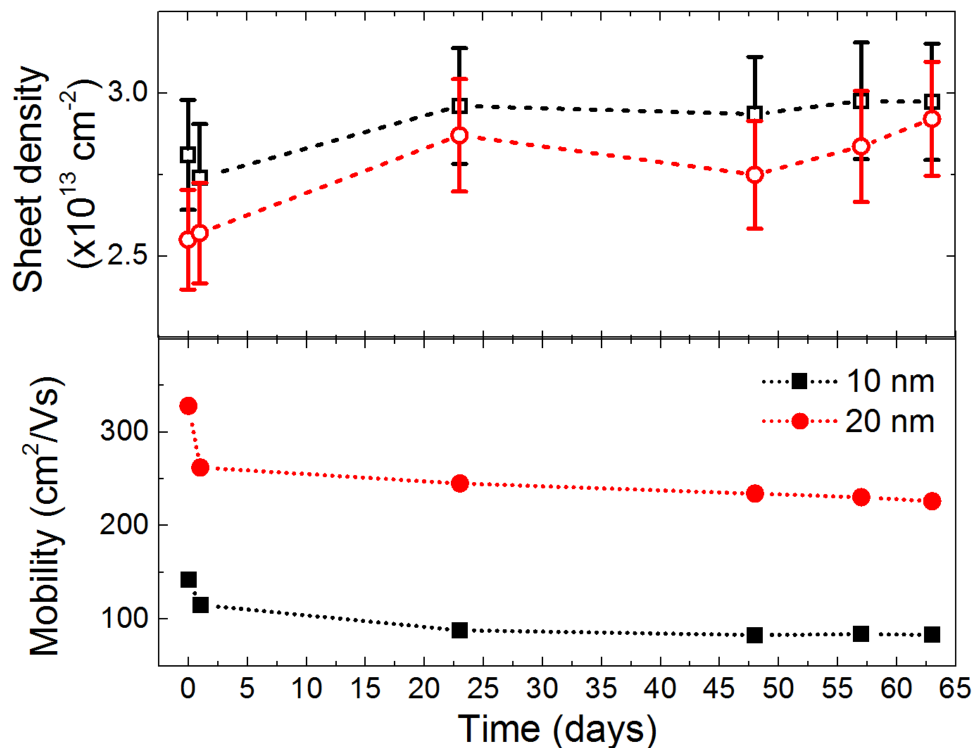

Figure 4.2 Sheet density (top, open symbols) and mobility (bottom, closed symbols) over time for films with thickness 10nm (black squares) and 20nm (red circles). The sheet density remains constant, indicating reduced ageing effects. Reproduced with permission from [38]

4.4 Film Morphology

Atomic force microscopy measurements were performed on a subset of films to correlate surface morphologies to electronic properties. Figure 4.3 compares samples grown at the four different Se:Bi flux ratios while keeping the film thickness and substrate growth temperature constant. We can see that films grown using a 2:1 or 3:1 flux ratio have hill or cloud like morphologies. This is most likely due to insufficient selenium during growth, potentially causing bismuth to aggregate. These

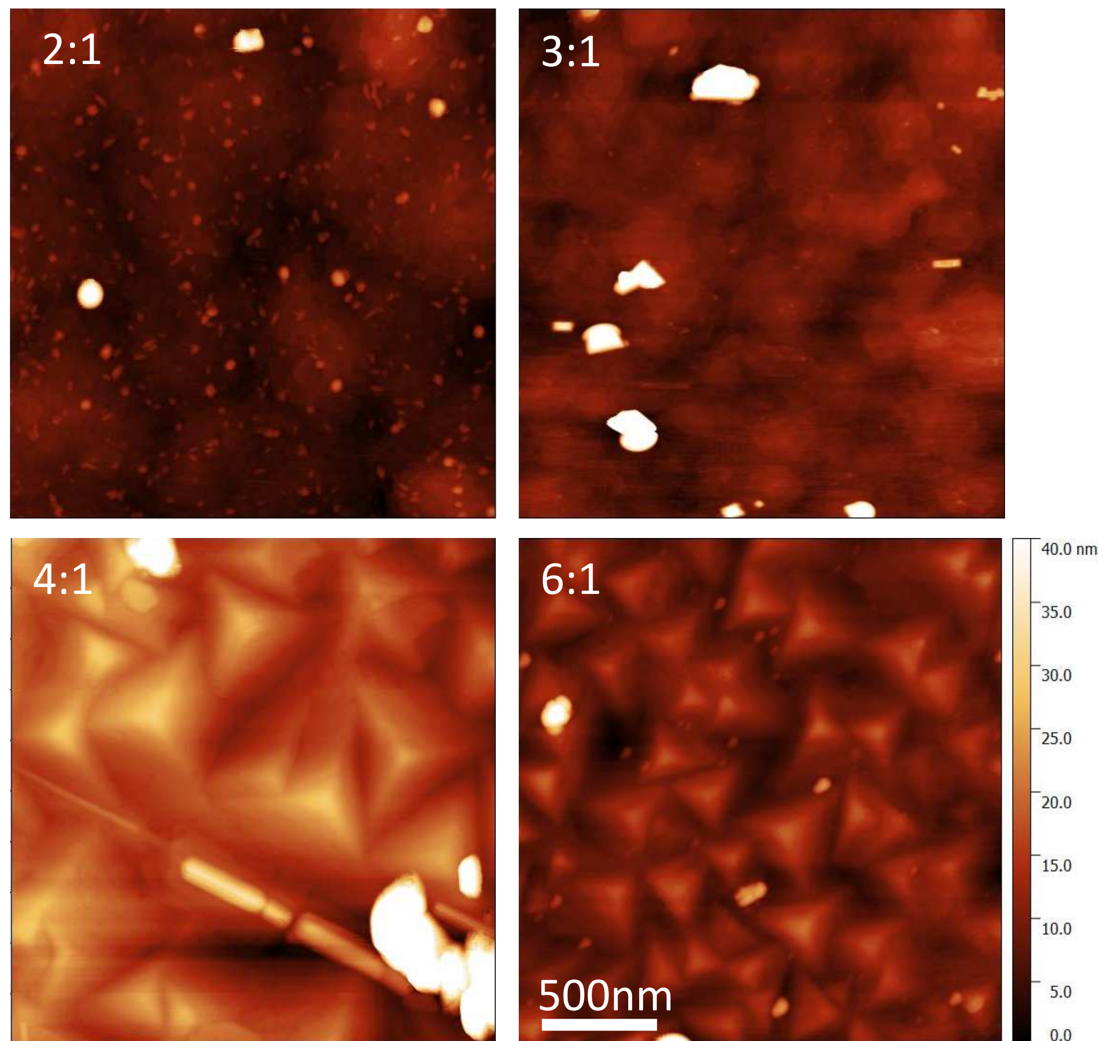

Figure 4.3 2μm x 2μm AFM scans for 100nm films grown with varying flux ratios, as indicated. Reproduced with permission from [38]

films also exhibited poor electrical properties, which were attributed to a high density of selenium vacancies in the films. Films grown using a higher flux ratio (4:1 or 6:1) exhibit the pyramid-like structures common to MBE grown Bi_2Se_3. The domain sizes are larger in the 4:1 film, implying that these growth conditions may be superior to the 6:1 growth condition, despite their similar electrical properties.

Figure 4.4 shows the AFM images of 100nm films grown at a 4:1 Se:Bi BEP ratio but with varying substrate temperatures. The 250 °C film shows much smaller pyramids than the 300°C film and has slightly worse electronic properties. At this lower substrate temperature there is lower surface mobility during growth which may lead to a higher defect density, resulting in poorer electronic properties. The low surface mobility likely also leads to smaller domains. At 330°C the morphology is hill like, similar to the 2:1 and 3:1 samples from Figure 4.3. At this

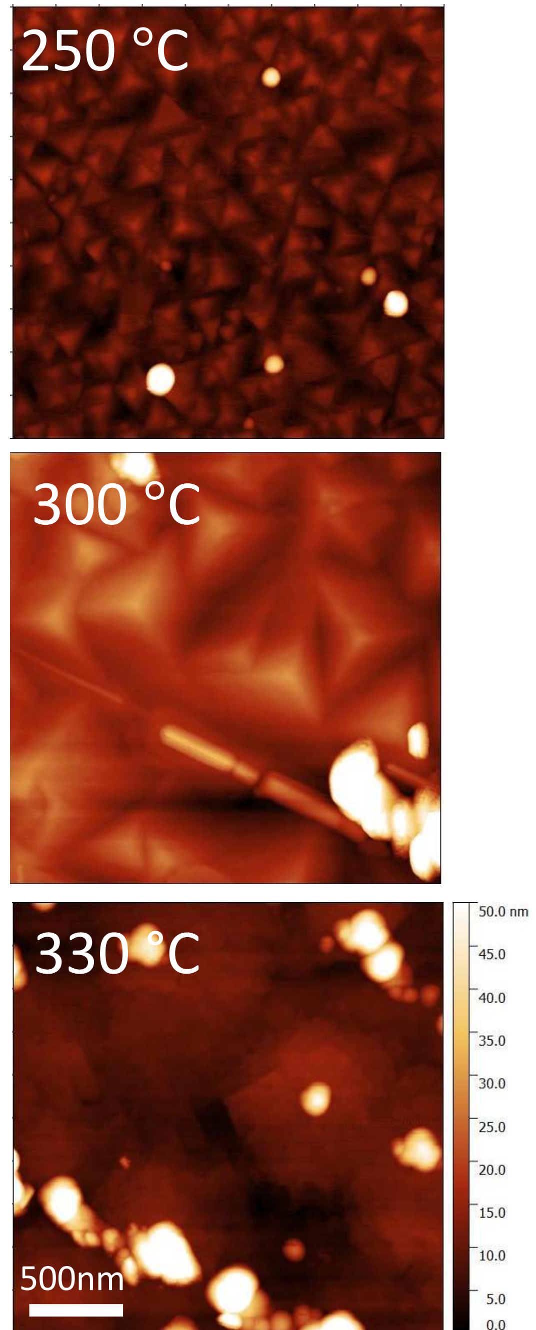

Figure 4.4 AFM scans of 100nm Bi_2Se_3 films grown using a 4:1 Se:Bi BEP ratio at varying substrate temperatures. Reproduced with permission from [38]

high substrate temperature there will be increased re-evaporation of selenium during the growth leading to surface characteristics and electrical properties similar to films grown with insufficient selenium flux. All three samples have similar surface roughness, despite the difference in surface quality.

Finally, Figure 4.5 shows AFM scans for growths with a 4:1 Se:Bi ratio, a substrate temperature of 300°C, and varying film thickness. The pyramid shape is already clearly visible in the 10nm film, indicating that the crystalline domains are established early in the growth however the small grain size indicates a lack of long-range order during the early stages of growth. The domain size increases with sample thickness, reaching about 500nm in the 100nm thick film and 1500nm in the 300nm thick film. As film thickness increases, the pyramids begin to merge into larger domains. It should be noted that the height of the pyramids does not increase

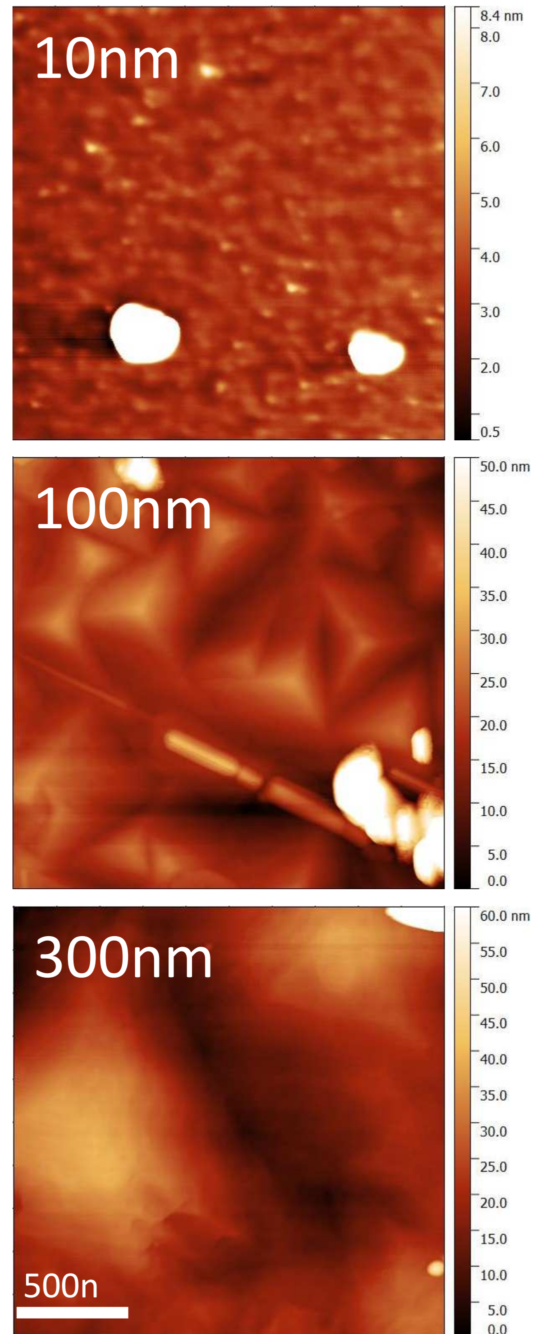

Figure 4.5 AFM scans of Bi_2Se_3 films with different thicknesses grown using a 4:1 Se:Bi BEP ratio at a substrate temperature of 300°C. Reproduced with permission from [38]

significantly between the 100nm and 300nm films, indicating that the surface roughness remains constant despite the larger domain size.

4.5 Summary

In this initial stage of our research we successfully grew thin films of Bi_2Se_3 with electronic properties and surface morphologies comparable to values reported in literature at the time. Using a valved selenium cracker source we were able to grow high quality films with much lower Se:Bi fluxes than traditionally reported. As can be seen by our struggles to grow quality films on Si(111) substrates the substrate film interaction is still extremely important to growth quality despite the van der Waals nature of the films. This substrate interaction results in a disordered layer at the interface preventing us from reaching the 2D carrier density limit theorized for topological insulator thin films, a problem which is addressed in later stages of our research.

Chapter 5

UNDERSTANDING THE ROLE OF DEFECT TYPE IN THIN FILM DOPING

5.1 Introduction

After optimizing the growth of Bi_2Se_3 to reduce carrier concentration and increase mobility, we turned to more novel approaches to produce an ideal topological insulator. It has been shown that in bulk crystals $Bi_2(Se_{0.33}Te_{0.66})_3$ reliably has the lowest carrier density of all the Bi_2Se_3-Bi_2Te_3 alloys. As discussed in section 2.2.2, this is due to the relative strengths of the Se-Bi and Te-Bi bonds. The stronger Se-Bi bond means the Se atoms preferentially occupy the center of the QL where they can form the most Bi bonds. As it is harder to form Se vacancies from this strongly bonded position, the n-type Se vacancies that plague pure Bi_2Se_3 are reduced. Likewise, the strong bonds to the center Se atoms help prevent Bi-Te antisite defects from forming, reducing the main doping source of bulk

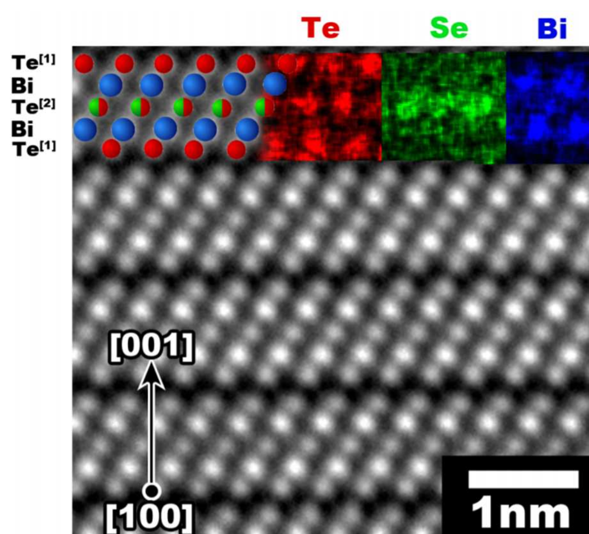

Figure 5.1 HAADF STEM image of $Bi_2Te_2.7Se0.3$ viewed along the [100] direction. The corresponding Te, Se, and Bi atomic resolution EDS maps are shown at the top. Note the Se signal resides in the Te(2) position. Reproduced with permission from [73]

Bi_2Te_3 samples. As can be seen in Figure 5.1 [73] the preferential Te-Bi-Se-Bi-Te QL arrangement has been confirmed via STEM/EDS and appears robust across bulk and MBE fabrication methods. In this chapter we will discuss work done with in collaboration with groupmate Yong Wang to reduce carriers in MBE grown TI films by alloying Bi_2Se_3 and Bi_2Te_3, published in Yong et al. [74]

To recreate the bulk alloying experiment in thin films, a series of $Bi_2(Se_{1-x}Te_x)_3$ films were grown on *c*-plane sapphire substrates using a variety of growth parameters. Film quality was monitored *in-situ* during growth via RHEED, using a sharp streaky RHEED pattern as a signal of good growth quality. After growth XRD was used to determine the alloy composition on the films using Vegard's law as a first approximation. As discussed in Section 3.2.4 Vegard's Law assumes that an alloy's lattice constant in the c-direction will vary linearly with composition. All compositions reported in this chapter are calculated using Vegard's Law and XRD data. An attempt was made to confirm the composition using Rutherford Backscattering Spectroscopy, however, it was unable to satisfactorily differentiate between selenium and tellurium.

5.2 Controlling Alloy Composition

First, the fluxes of selenium and tellurium were varied to change film composition as the substrate temperature was held constant at 300°C and the bismuth flux was set to produce a growth rate of ~1nm/min. A series of six films were grown as shown in Table 5.1. Figure 5.2.a shows the wide angle XRD data for these films. In all six samples the peak for the sapphire substrate can be seen at ~42 degrees. The rest of the peaks are in good agreement with the predicted peak locations for the (001) orientation of a bismuth chalcogenide thin film. As the sample composition shifts to

higher tellurium incorporation (top to bottom), the XRD peaks for the films clearly shift towards lower angle. Since this shift is more pronounced at higher angle,

Table 5.1 Growth parameters for films grown with varying alloy compositions. The lattice constants were determined by XRD and the tellurium content was calculated using Vegard's Law. Reproduced with permission from [74]

Se:Bi	Te Bulk (°C)	Te Valve (mils)	Lattice Constant (Å)	% Te
4:1	200	0	28.7	0
4:1	200	150	29.18	30.16
1:1	210	150	29.39	42.22
1:1	215	300	29.76	62.58
1.4:1	230	150	29.80	65.04
0:1	260	100	30.5	100

zooming on the [0 0 21] peak allows the composition dependent shift to be observed with a high degree of peak separation between the films, Figure 5.2.b. The compositions used in the figure legend were calculated using this [0 0 21] peak, Vegard's Law, and pure Bi_2Se_3/Bi_2Te_3 as endpoints.

Based on the full width half maximum values of the [0 0 21] peaks it seems that Bi_2Se_3, Bi_2Te_3, and $Bi_2(Se_{0.37}Te_{0.63})_3$ have better crystal quality than the other alloys. This is in keeping with the theory that a Te-Bi-Se-Bi-Te is a favorable arrangement. In high selenium content films, we occasionally saw peak splitting like that shown by the 30% tellurium film in Figure 5.2.b. [74] This might indicate that high selenium films are less stable and more prone to phase segregation than the "ideal" $Bi_2(Se_{0.33}Te_{0.66})_3$ alloy

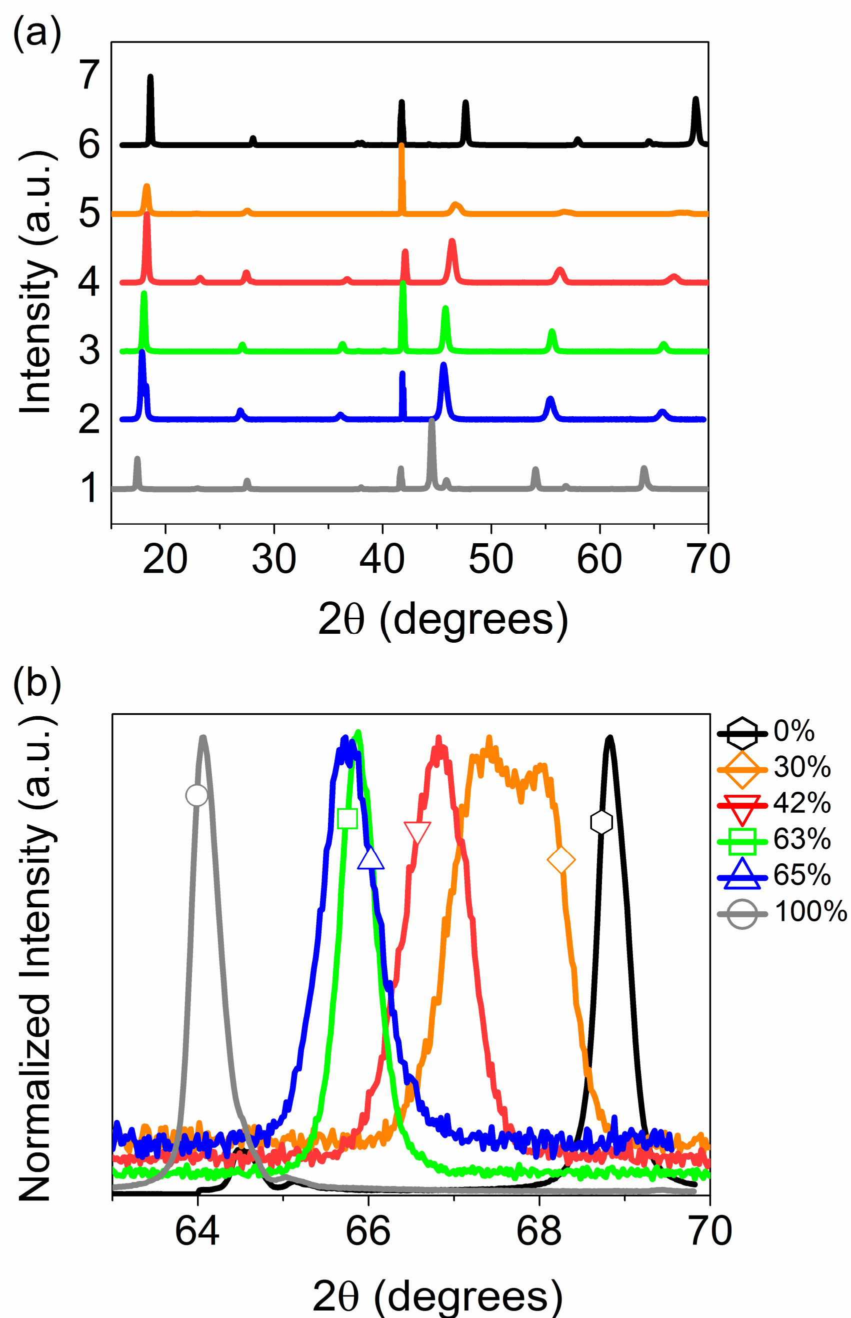

Figure 5.2 a) Wide-range XRD spectra for samples with different tellurium content, as indicated in the legend. Tellurium content increases from top to bottom. All intensities are normalized and data is offset for clarity. b) The [0021] peak showing the shift in peak position with tellurium content. The growth parameters for samples in this Figure can be found in Table 5.1. Reproduced with permission from [74]

.

5.3 Preferential Selenium Incorporation

While the tellurium heavy $Bi_2(Se_{0.33}Te_{0.66})_3$ is clearly a stable and favorable alloy, our samples indicate preferential incorporation of selenium during MBE growth. From Table 5.1, we can see that selenium and tellurium do not incorporate at the same rate. The Se;Te ratio measured in the films always shows more selenium than would be expected from the Se:Te flux ratios during growth, a trend is commonly seen in II/VI systems such as CdSeTe and ZnSeTe [75,76]. This preferential incorporation is a result of being the Bi_2Se_3 more stable of the two binaries. The bond length of Bi_2Se_3 is shorter than that of Bi_2Te_3, indicating that the Bi_2Te_3 has a lower binding energy than Bi_2Se_3. Furthermore, enthalpy of formation for Bi_2Se_3 at 273K is 28 kJ/(g

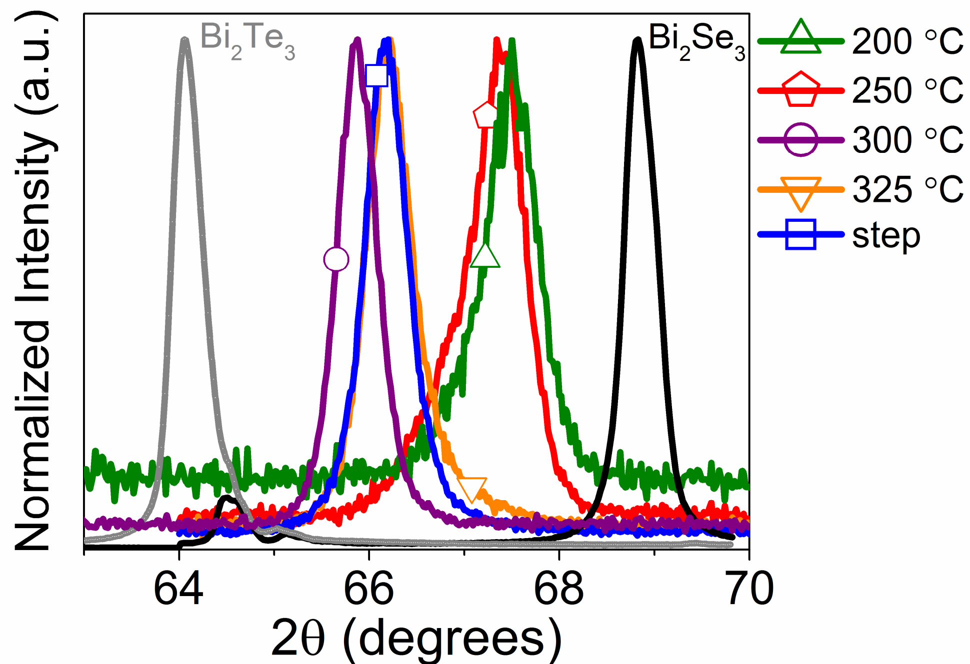

Figure 5.3 XRD spectrum of samples grown with a fixed flux ratio and a variable substrate temperature. The blue line represents the sample grown with a two-step procedure: a substrate temperature of 200°C for first 4 QLs and followed by a ramp up to 300°C for the rest of the growth. Lines on the far left and far right are pure Bi_2Te_3 and Bi_2Se_3 respectively, for comparison. Reproduced with permission from [74]

atom) as compared to only 15.7 kJ/(g atom) [77] for Bi_2Te_3. As growth temperature changes the incorporation of each element, it is possible to vary the Se;Te flux while keeping the resulting alloy compotion constant. These comparisons were done to determine the optimal growth parameters for the Bi_2SeTe_2 samples (discussed below).

The relative incorporation rates of tellurium and selenium were further explored by keeping the Se:Te flux ratio fixed while varying the substrate temperature used during growth. As can be seen in Figure 5.3, at low substrate temperatures tellurium incorporation into the film is reduced. This may be another feature of the stronger Se-Bi bond. As selenium and tellurium atoms impinge upon the surface and start to form bonds, the lower energy tellurium bond is easier to break. Tellurium may reevaporate from the growth surface at a faster rate than the selenium without the increased surface temperature to help break apart Se-Bi bonds. Increasing the substrate temperature to 300°C, our usual growth temperature for Bi_2Se_3 [38], also increased tellurium incorporation into the film. Two other substrate temperatures were tried: 325°C, and a two-step procedure in which the first four QLs were grown at 200°C followed by a ramp up to 300°C for the rest of the growth, inspired by work on other TI materials [78–80]. In both cases tellurium incorporation was slightly reduced as compared to the 300°C sample. This is all in good agreement with the theory that Bi_2Se_3 is the more stable of the two compounds. Any deviation from the optimized growth conditions result in a trend towards the more stable compound and higher selenium incorporation.

5.4 Electrical Properties

To determine if MBE grown $Bi_2(Se_{0.33}Te_{0.66})_3$ thin films behave like bulk samples and produce better electrical properties than other alloys we measured their mobilities and carrier densities using a room temperature Hall setup. As a reminder, an ideal TI film must have a high mobility- as the electrons in the surface states can travel mostly unimpeded at relativistic speeds. The ideal film will also have a low sheet carrier density as bulk carriers are reduced, leaving only surface state carriers. Unfortunately, the data shown in Figure 5.4 does not agree with the desired bulk behavior. As tellurium content increases the electrical properties of the films worsen:

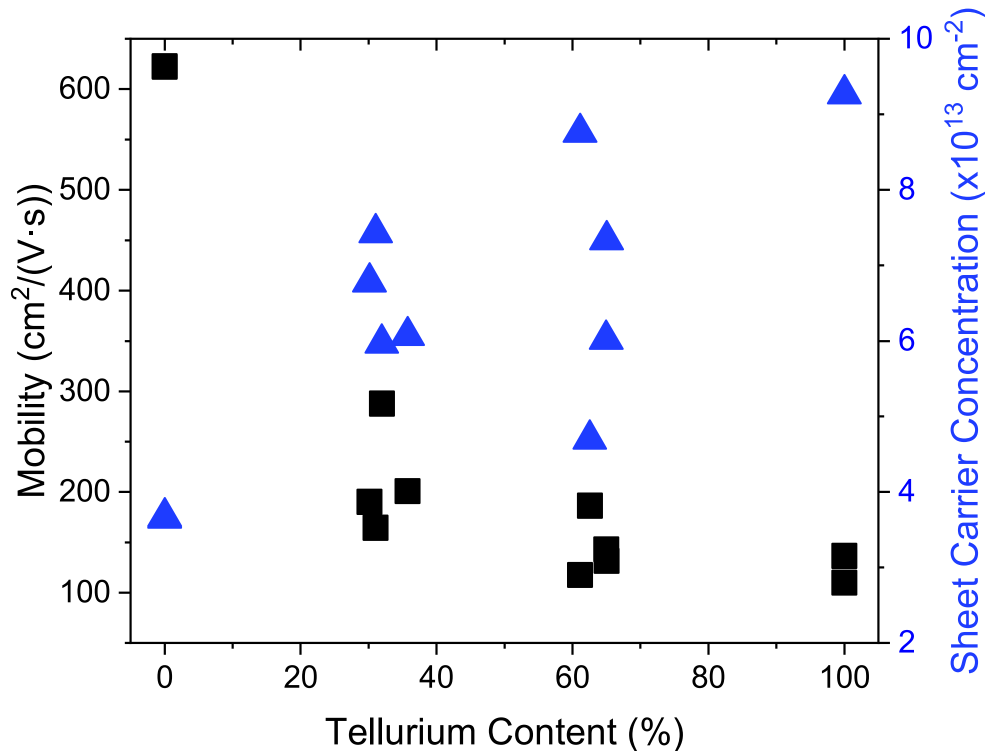

Figure 5.4 The mobilities (black) and sheet carrier concentrations (blue) of films grown with varying tellurium content. As tellurium content increases the mobility trends downwards while the carrier concentration trends upwards. Data clusters around 33% and 66% indicate samples with different growth parameters but similar compositions. Reproduced with permission from [74]

sheet carrier concentration increases while mobility decreases. While varying growth parameters for both the 33%Te and 66%Te alloys did produce some improvement in electrical properties, neither composition was able to match pure Bi_2Se_3. In a stark contrast to bulk films, there is no significant improvement in film quality at the $Bi_2(Se_{0.33}Te_{0.66})_3$. These results indicate that selenium vacancies and Bi-Te antisite defects are not the primary doping mechanism in MBE grown thin films.

5.5 Indication of a Disordered Interface

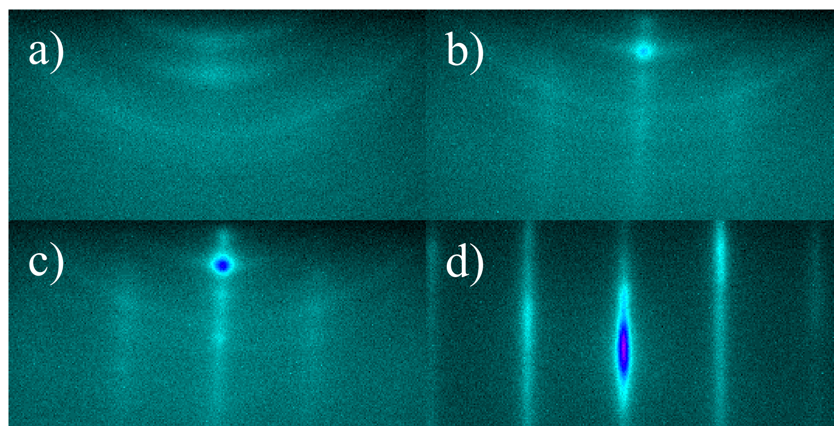

Figure 5.5 a)-d) The progression of the RHEED pattern from polycrystalline rings to single crystal streaks over the course of 5-15 QL (depending on growth conditions).

As an alternate explanation of high bulk doping in bismuth chalcogenide thin films, we propose a disordered layer at the interface between the substrate and the grown film. This hypothesis is supported by various observations in our research. First, at the beginning of each growth we see a ring RHEED pattern indicating polycrystalline growth. Depending on growth conditions these rings may last for 5-15QL before transitioning into lines, Figure 5.5.a-d This is a clear indication that there is a period of disorder before high quality single crystal growth is achieved and has been previously reported by other groups [81–84]. Next, as we see in Figure 5.6.a-b,

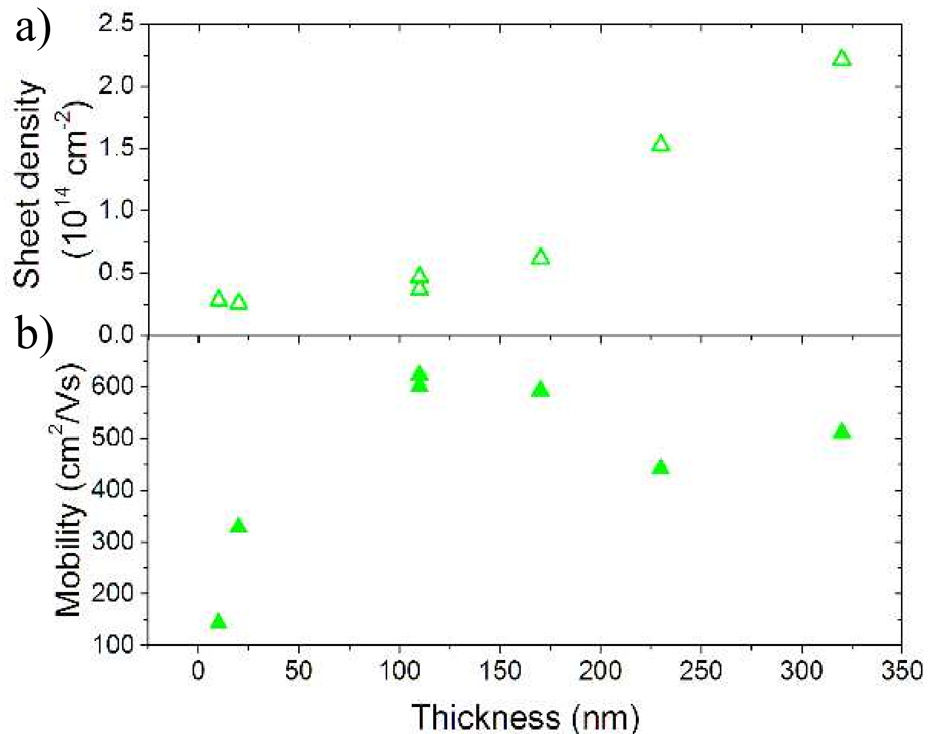

Figure 5.6 The a) sheet carrier density and b) mobility of films of varying thickness.

the sheet carrier density is fairly constant for films 10-100nm thick. If bulk carriers were the dominant pathway, we would expect to see a linear increase in carriers with thickness. Instead, we see very little increase in the thin films that would be most sensitive to interface disorder followed by a linear sheet density increase in thick films where bulk carriers can dominate the interface. Likewise, the recorded mobility is very poor for thin films but levels out for thicker films. Finally, despite attempting to optimize growth conditions, pure Bi_2Te_3 displayed worse electrical properties than either Bi_2Se_3 or any of the alloy compositions. If the transport properties were dominated by bulk behavior or by alloy scattering, we would expect the Bi_2Te_3 to behave similarly to the Bi_2Se_3 films. As noted above, Bi_2Te_3 is less stable than Bi_2Se_3 and therefore more likely to form defects at the film/substrate interface when grown

on a mismatched substrate. These higher-defect density layers can then lead to a larger sheet carrier density and a lower mobility in Bi_2Te_3 compared to Bi_2Se_3. When tellurium is alloyed into the Bi_2Se_3 crystal, similar effects are expected since tellurium will preferentially occupy sites on the outside of the QL, while selenium will preferentially occupy the inner site. Given these results, we believe that the transport properties of our films are dominated by the quality of the film/substrate interface, despite the use of van der Waals epitaxy, and not by bulk defects. This supports the conclusion from Chapter 4 that substrate interaction plays a key role in van der Waals growth.

Chapter 6

BISMUTH INDIUM SELENIDE BUFFER LAYERS TO IMPROVE ELECTRONIC PROPERTIES

6.1 Introduction

The results from Chapters 4 and 5 clearly indicate that a highly defective layer at the substrate interface is the primary source of bulk doping in our films. A growing body of research shows that van der Waals materials have a strong tendency towards 3D growth after nucleation, instead of the clean layer by layer growth found in many epitaxially grown III-V material systems [85–87]. Controlling nucleation and interface dynamics to create large areas of atomically flat films or single layer growth remain one of the open problems in van der Waals epitaxy. However, for the sake of our films we can borrow a technique from traditional epitaxy; instead of fixing the interface itself, we can bury the defective interface by creating a buffer layer to grow the TI films on. The alloy $(Bi_{1-x}In_x)_2Se_3$ was selected as our buffer layer material as it has the same crystal structure as Bi_2Se_3 and Bi_2Te_3, a similar lattice constant, and is a trivial insulator for $x>0.3$ [34]. This chapter will discuss work done in collaboration with Yong Wang on the growth of $(Bi_{1-x}In_x)_2Se_3$ and its effectiveness as a buffer layer to improve the electrical properties of Bi_2Se_3 and Bi_2Te_3. The optimization of $(Bi_{1-x}In_x)_2Se_3$ growth is discussed in greater detail in Yong et al. [88]

6.2 Seed Layer

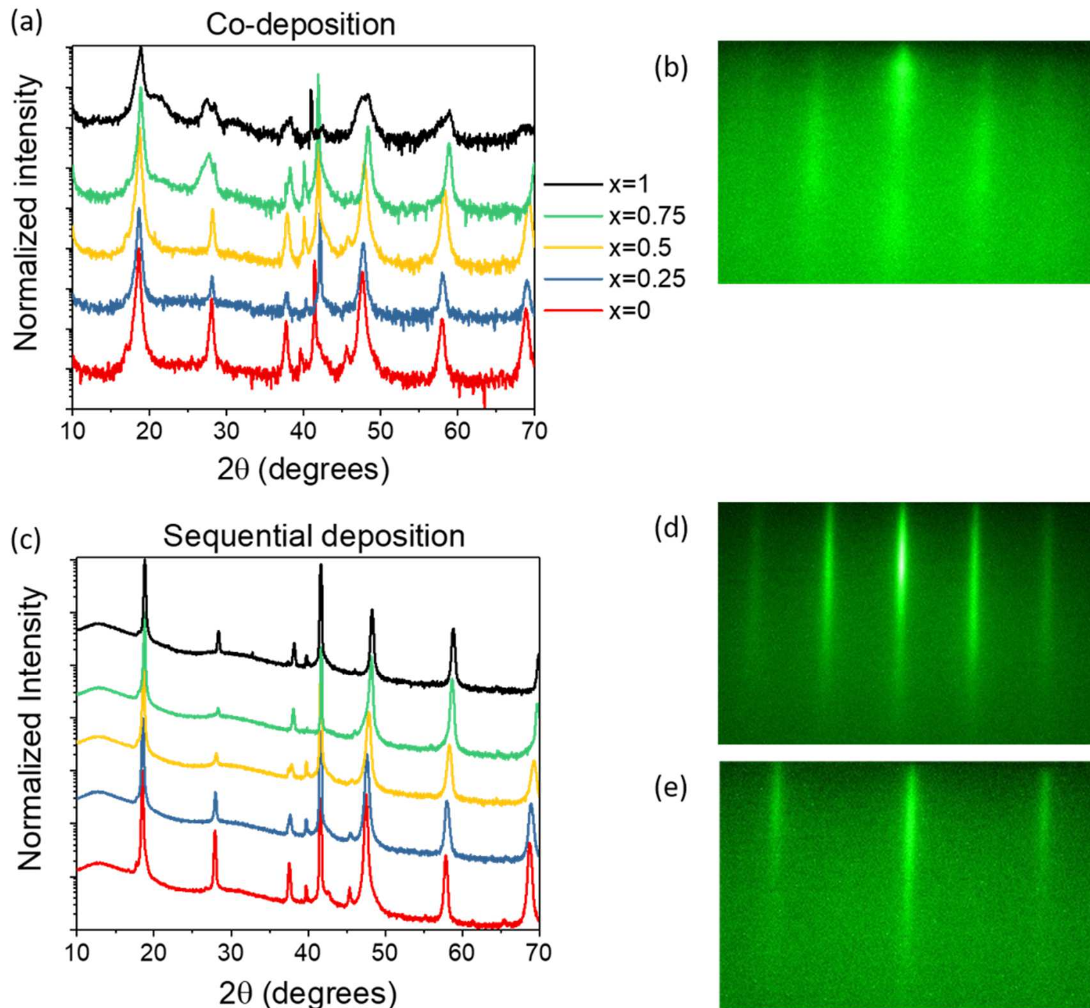

Figure 6.1 Comparison of co-deposited (a, b) BIS films with BIS films grown on a sequentially deposited seed layer (c, d, e). (a) XRD scans of five co-deposited BIS films with indium concentration increasing from bottom to top, as indicated in the legend. All the scans are normalized to the maximum of each scan and offset for clarity. For high indium content films, the FWHM of the peaks increases and double-peaks begin to arise, indicating poor crystal quality. (b) RHEED image of a co-deposited (Bi0.5In0.5)2Se3 film showing wide, diffuse streaks with intensity variation, indicating polycrystalline growth. (c) XRD scans of five BIS films grown on a sequentially-deposited seed layer with the same compositions as in (a). For all films, the peak FWHM is narrow and no double-peaks are observed. (d, e) RHEED images in the $[10\bar{1}0]$ (d) and $[11\bar{2}0]$ (e) directions showing thin lines and different streak spacing, indicating high-quality, single-crystal film growth. Reproduced with permission from [88]

The first attempts at growing $(Bi_{1-x}In_x)_2Se_3$ of various compositions were done via co-deposition, meaning the bismuth and indium were deposited simultaneously. In this method the Bi:In flux ratios were varied while keeping the (Bi+In):Se ratio constant during growth. All films discussed in this chapter were grown on sapphire substrates. It was found that for all alloy compositions co-deposition produced low quality films with blurry RHEED patterns during growth, Figure 6.1.b. The blurry RHEED images indicate poor long-range order, and there for poor crystal quality. XRD of the films revealed the fullwidth half-maximum values of the peaks increased with indium content, Figure 6.1.a, suggesting that indium incorporation was responsible for poor film quality. In_2Se_3 is known to have at least five polymorphs (α, β, γ, δ, and κ [89–93]) which have varying crystal structures and lattice constants. We aimed to grow the β-phase as it is as a similar lattice constant to Bi_2Se_3. However, we believe growth by co-deposition results in multiple polymorphs in one film, rather than a single polymorph, leading to the degradation of film quality. In fact, the pure In_2Se_3 film has clear peak splitting in the XRD scan, indicating the presence of at least one similar secondary phase.

To combat this polymorph induced disorder, a new growth recipe was devised with a sequentially grown seed layer. First 5QL of pure Bi_2Se_3 were grown at 300°C to pin the growth into the correct phase. Since Bi_2Se_3 does not possess any known polymorphs, growth with no phase segregation was consistently achieved. Next, 5QL of In_2Se_3 were grown and the bilayer was heated to 425°C to anneal in a selenium overpressure. During the annealing step the indium and bismuth interdiffuse to create

a 10QL layer of single phase $(Bi_{0.5}In_{0.5})_2Se_3$. Room temperature Hall measurements were used to confirm that the resulting seed layer was a trivial insulator. Once the seed layer was grown and annealed the substrate could be cooled to the correct growth temperature for the desired composition of $(Bi_{1-x}In_x)_2Se_3$. Using the sequential deposition method resulted in sharper RHEED images and smaller fullwidth half-maximum values in XRD, indicating improved structural quality from films of all compositions.

6.3 $(Bi_{0.5}In_{0.5})_2Se_3$ as a Buffer Layer

Table 6.1 A description of all films discussed in sections 3 and 4. Including the composition of the TI layer, thickness and growth type of the buffer layer, thickness of the capping layer, mobilityμ, and 2D sheet carrier concentration n_s Reproduced with permission from [88]. "Co." indicates codeposition while "Seq" indicates sequential deposition..

Sample	TI Comp.	Buffer	Cap	μ (cm^2/Vs)	n_s ($x10^{13}$ cm^{-2})
A	Bi_2Se_3	None	None	434±21.7	2.61±0.16
B	Bi_2Se_3	15nm Co.	None	202±21.7	1.38±0.08
C	Bi_2Se_3	50nm Co.	None	314±15.7	1.14±0.07
D	Bi_2Se_3	50nm Seq.	None	659±33.0	1.42±0.09
E	Bi_2Se_3	50nm Seq.	50nm	453±22.7	1.86±0.11
F	Bi_2Te_3	None	None	165±8.2	9.27±0.56
G	Bi_2Te_3	50nm Seq.	50nm	262±13.1	2.79±0.17

To first evaluate the effectiveness of $(Bi_{1x}In_x)_2Se_3$ as a buffer layer for Bi_2Se_3, a series of Bi_2Se_3 films were grown on $(Bi_{0.5}In_{0.5})_2Se_3$ buffer layers with varying parameters. The 50% indium composition was chosen to minimize lattice mismatch

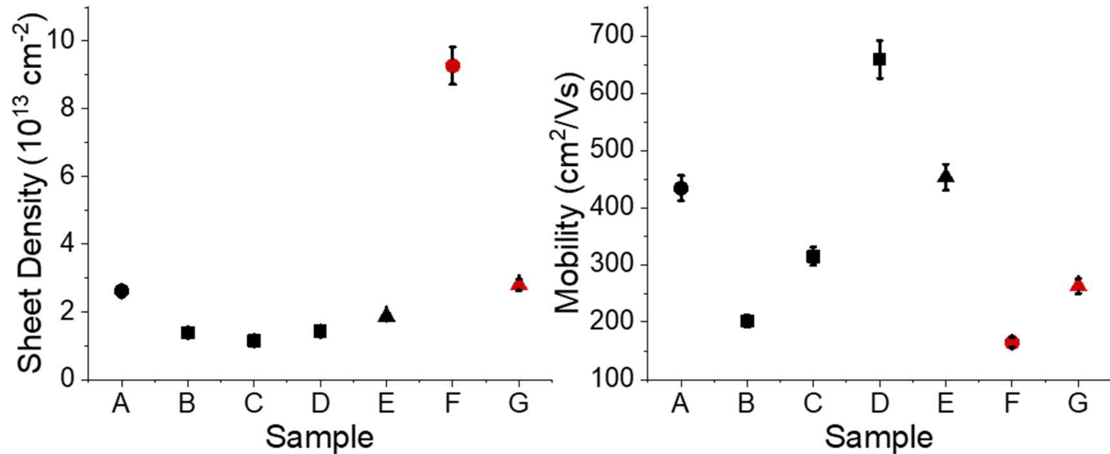

Figure 6.2 Room temperature sheet density and mobility of the samples listed in Table 6.1. Black symbols represent Bi_2Se_3 samples while red symbols represent Bi_2Te_3. Circles are unbuffered samples, squares are buffered samples, and triangles are layered heterostructures. Error bars were included for all images but may be hidden by the symbol.

and indium diffusion into the TI layers while still ensuring an insulating buffer layer. Room temperature Hall measurement were then taken to compare the films' electrical properties to that of unbuffered Bi_2Se_3 (sample A in Table 6.1), improved electrical properties were defined as a reduced sheet density and an increased mobility. First, a 15nm buffer layer was grown via co-deposition (Sample B). This film showed a large decrease in both sheet density and mobility, Figure 6.2. Increasing the buffer thickness to 50nm (Sample C) further improved the sheet density and showed a partial recovery of the mobility. Finally, growing Bi_2Se_3 on a 50nm sequentially deposited buffer layer (Sample D) resulted in a film with a 50% reduction in sheet density and a 50% increase in mobility, proving the efficacy of a sufficiently thick and well grown $(Bi_{0.5}In_{0.5})_2Se_3$ layer as a buffer layer.

6.4 Topological Insulator Heterostructures

With an eye towards future experiments with $Bi_2Se_3/(Bi_{1-x}In_x)_2Se_3$ heterostructures, a layered sample of 50nm $(Bi_{0.5}In_{0.5})_2Se_3$ / 50nm Bi_2Se_3 / 50nm

$(Bi_{0.5}In_{0.5})_2Se_3$ (Sample E) was grown and examined via Hall measurements. While the electrical properties did worsen compared to the buffer film, the sheet density remained improved compared to the unbuffered film and the mobility was equal within error bars. A similar film of 50nm $(Bi_{0.5}In_{0.5})_2Se_3$ / 50nm Bi_2Te_3 / 50nm $(Bi_{0.5}In_{0.5})_2Se_3$ (Sample G) was grown to see if the buffer layer also improved the electrical properties of Bi_2Te_3 (Sample F). This layered structure showed a reduced sheet density of 2.87×10^{13} cm^{-2}, as compared to 9.27×10^{13} cm^{-2} in the best Bi_2Te_3 results achieved in unbuffered films. The mobility also improved from 164 cm^2/Vs in the unbuffered film to 262 cm^2/Vs in the layered structure. While this demonstrates significant improvement in the quality of Bi_2Te_3 films, the electrical properties remain worse than those of even unbuffered Bi_2Se_3 films. The n-type doping may indicate that the majority of carriers are coming from Te_{Bi} antiste defects, potentially due to using a large tellurium overpressure during growth.

6.5 Conclusion

This research successfully demonstrated the efficacy of $(Bi_{0.5}In_{0.5})_2Se_3$ as a buffer layer to improve the electrical properties of both Bi_2Se_3 and Bi_2Te_3 topological insulators. These results suggest that a buffer layer may also be used to grow Bi_2Se_3 on other substrates where the initial substrate interaction causes a disordered layer and degrades film quality. Additionally, it was shown that, while growing $(Bi_{0.5}In_{0.5})_2Se_3$ on top of Bi_2Se_3 did slightly worsen the films properties (potentially due to increased disorder at the interface introduced during the growth of the capping layer), a layered insulator/TI/insulator film remained of high enough quality to study its' TI properties. This opens the door to growing TI/insulator heterostructures to investigate the interaction between multiple TI layers.

Chapter 7

SELF-ASSEMBLED BISMUTH SELENIDE NANOWIRES IN VAN DER WAALS EPITAXY

7.1 Introdcution

After successfully using a $(Bi_{0.5}In_{0.5})_2Se_3$ buffer layer to improve the quality of Bi_2Se_3 grown on a sapphire substrate, we turned our attention to improve film quality on GaAs (001) substrates. GaAs(001) was chosen as is it a technologically relevant substrate that is known to have a high degree of interaction with bismuth adatoms. Successful growth on GaAs(001) would also allow for future experiments using backgating to dynamically tune the Fermi level. In this section the growth of $(Bi_{1-x}In_x)_2Se_3$ was explored with regard to surface oxide removal conditions, growth stages, selenium over pressure, and Bi:In alloying. It was found that growth on GaAs(001) produced a wide range of morphologies of $(Bi_{1-x}In_x)_2Se_3$ including self-assembled nanowires, smooth surfaces, and needle like phase segregation. Exploration of phase space indicated that morphology was either controlled by the fast diffusion of bismuth along the GaAs[110] direction in the case of the nanowires or the tendency of In_2Se_3 to phase segregate in the case of the needles. This chapter provides valuable insight into previously unexplored growth mechanics of vdW materials and provides insight into improved growth of these materials in the future. All samples discussed in this chapter are listed in Table 7.1.

Table 7.1 A list of all samples included in this study. The selenium fluxes and indium contents given are those used during the $(Bi_{1-x}In_x)_2Se_3$ stage of the growths

Sample	Structure	Se Flux ($x10^{-6}$ Torr)	x (In content)
A	5nm Bi_2Se_3	4.02	N/A
B	5nm Bi_2Se_3 +5nm In_2Se_3	4.02	N/A
C	5nm Bi_2Se_3 + 5nm In_2Se_3 40min anneal (entire seed layer)	4.11	N/A
D	Seed + $(Bi_{1-x}In_x)_2Se_3$	2.32	0.5
E	Seed + $(Bi_{1-x}In_x)_2Se_3$	2.49	0.5
F	Seed + $(Bi_{1-x}In_x)_2Se_3$	3.76	0.5
G	Seed + $(Bi_{1-x}In_x)_2Se_3$	4.04	1
H	Seed + $(Bi_{1-x}In_x)_2Se_3$	4.08	0.75
I	Seed + $(Bi_{1-x}In_x)_2Se_3$	4.07	0.5
J	Seed + $(Bi_{1-x}In_x)_2Se_3$	4.00	0.25
K	Seed + $(Bi_{1-x}In_x)_2Se_3$	4.09	0
L	Seed + $(Bi_{1-x}In_x)_2Se_3$ + 50nm Bi_2Se_3	3.09	0.5
M	Seed + $(Bi_{1-x}In_x)_2Se_3$ + 50nm Bi_2Se_3	1.23	0.5

7.2 Deoxidization

Growing epitaxial films on GaAs substrates requires the removal of the native oxide layer. Typically, this is achieved by heating the substrate to the deoxidization point while maintaining an arsenic overpressure to prevent arsenic from evaporating out of the substrate. For this study, a selenium overpressure was maintained during the deoxidization process as described above to compensate for the arsenic outgassing and to prevent the formation of gallium droplets. If selenium pressure during this process was below ~$2x10^{-6}$ Torr, pit defects formed on the substrate. These defects were present even when the RHEED showed a transition to the (2x4) surface reconstruction associated with successful deoxidization under an arsenic overpressure. $(Bi_{1-x}In_x)_2Se_3$ films grown on pitted substrates display needle-like nano-features clustered around the pit edges. The pits seem to encourage the phase segregation seen in indium rich alloys

(discussed later in the paper); it is therefore crucial to ensure a high selenium flux during the deoxidization process if homogenous growth is desired.

7.3 Seed Layer

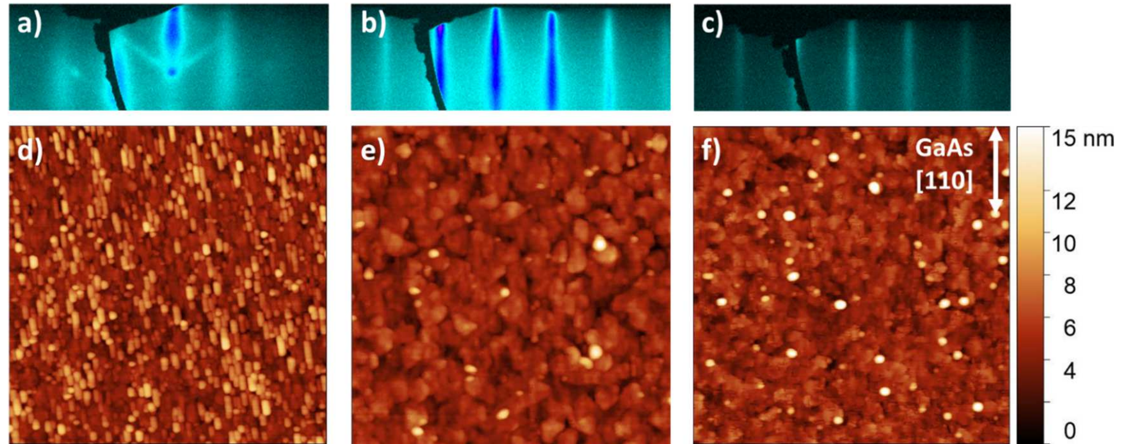

Figure 7.1 RHEED (a-c) and AFM (d-f) images of various stages in seed layer development. (a) and (d) show 5nm of Bi_2Se_3 (Sample A); (b) and (e) show 5nm of In_2Se_3 on 5 nm of Bi_2Se_3 (Sample B); (c) and (f) show the completed seed layer after annealing (Sample C). All AFM images are 2μm x 2μm and have the same scale bar and orientation relative to the substrate.

We will first discuss how the seed layer nucleates the GaAs(001) substrate after deoxidization in a selenium overpressure. Understanding the nucleation of this layer sets the stage for discussing the unique morphologies we achieve. A series of three films (Samples A-C) were grown representing each stage of the seed layer. Sample A was terminated immediately after the initial 5nm of Bi_2Se_3, Sample B was terminated after 5nm of Bi_2Se_3 and 5nm of In_2Se_3, and Sample C was terminated after the anneal. As shown in Figure 7.1.a, after the growth of the initial 5 nm of Bi_2Se_3, the RHEED pattern show chevrons which are indicative of faceted growth. The black shape in all RHEED images is a selenium flake that fell on the RHEED screen. The corresponding AFM image in Figure 7.1.d shows that the film has formed small rectangular domains extending along the [110] direction of the substrate. In Sample B,

the RHEED pattern in Figure 7.1.b has transitioned into streaks while the rectangular domains shown in the AFM image in Figure 7.1.e have spread into triangular domains more typical of this material system. It is important to note that the newly formed triangular domains inherit the strong substrate alignment established in the Bi_2Se_3 layer. For Sample C, the streaks in the RHEED image shown in Figure 7.1.c have sharpened further and the domains in the AFM image in Figure 7.1.f have become more cohesive while maintaining their orientation to the substrate. While the seed layer is only 10nm thick, it is already clear that a clear interaction with the substrate is present.

7.4 Varying Selenium During Growth

Next, we will study the effect of selenium overpressure during the buffer layer growth. All films were grown on identical seed layers as previously described, and all films were of the $(Bi_{0.5}In_{0.5})_2Se_3$ composition. Sample D was grown using a low selenium flux of 2.32×10^{-6} Torr as measured with a beam flux monitor using an iridium filament. This film had a spotty/chevron RHEED pattern, which is typical of highly three-dimensional growth as shown in Figure 7.2.a. This three dimensionality is confirmed by SEM and AFM images in Figure 7.2.d and Figure 7.2.g which show a needle-like morphology. The needles are aligned along the (110) axis of the GaAs substrate. Increasing the selenium flux to 2.49×10^{-6} Torr for Sample E results in a mostly streaky RHEED pattern as shown in Figure 7.2.b Both the AFM and SEM images for Sample E shown in Figure 7.2.e and Figure 7.2.h show a much smoother film. While some needle structures are still present in the AFM scan, their density is much lower, and they are much smaller at about 15nm tall. Between the needles, the film is smooth rather than terraced, which makes it an ideal candidate for use as a

buffer for TI films. Unfortunately, the growth window for this morphology is small and easily falls into the needle morphology as growth progresses. Constant monitoring of the RHEED and adjustment of the selenium flux may be needed to obtain a smooth morphology throughout the entirety of the buffer layer growth. Finally, for Sample F the selenium flux was increased even further to 3.76 x10^{-6} Torr. The RHEED pattern for Sample F, shown in Figure 7.2.c, is spotty and indicative of three-dimensional growth. This is confirmed by the SEM and AFM images shown in Figure 7.2.f and

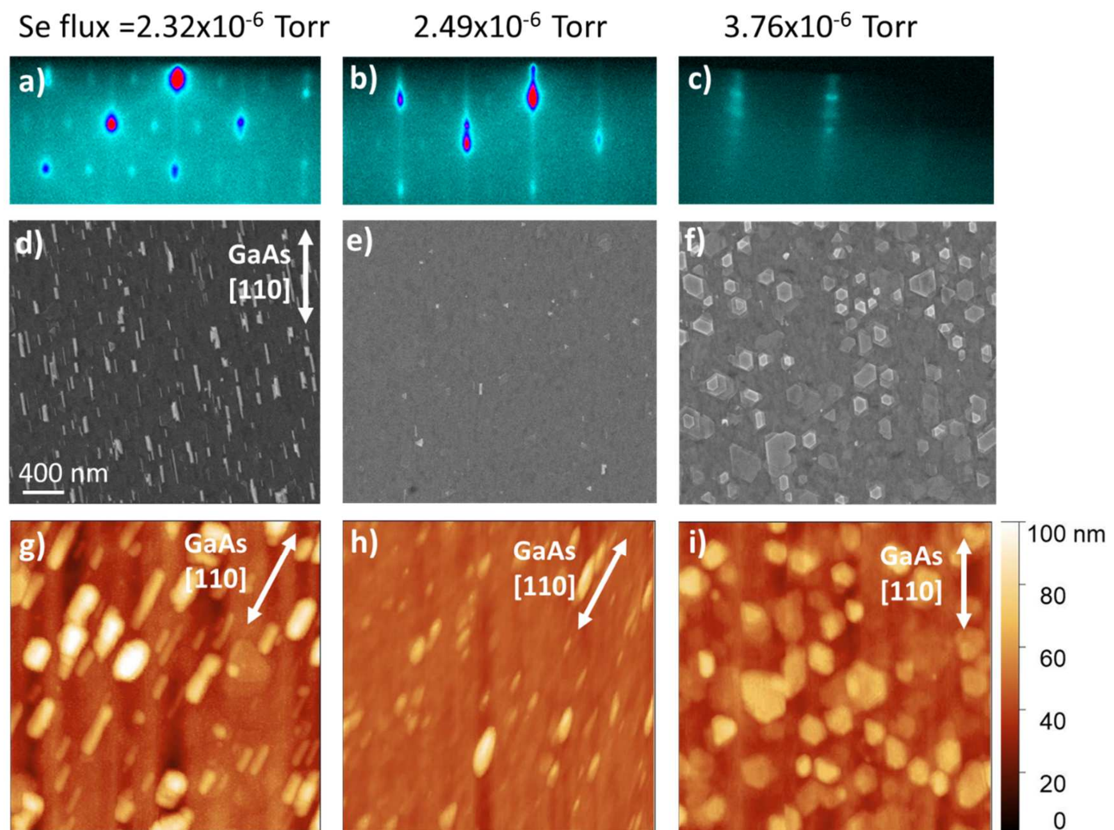

Figure 7.2 RHEED (a-c), SEM (d-f), and AFM (g-i) images of complete $((Bi_{0.5}In_{0.5})_2Se_3$ buffer layer grown at varying selenium over pressures. (a), (d), and (g) show Sample D grown with a low selenium overpressure; (b), (e), and (h) show Sample E grown with a moderate selenium overpressure; (c), (f), and (i) show sample F grown with a high selenium overpressure. All SEM images have the same scale bar and substrate orientation. All AFM images are 2μm x 2μm and have the same scale bar.

Figure 7.2.i. We observe a columnar growth morphology with sheer-walled columns or nanowires ranging from 50-300 nm in diameter and up to 30 nm tall. The tops of the columns are extremely smooth except for the occasional step edge where a terrace has yet to fully cover the underlying layer. As in Samples D and E, the structures present in Sample F are aligned along the (110) axis of the underlying substrate.

7.5 Varying Indium:Bismuth Ratio

Finally, we grew a series of films in which we changed the Bi:In flux ratio using a constant, high selenium overpressure to better understand how the interaction between the film and the substrate is driving the surface morphology. All films were

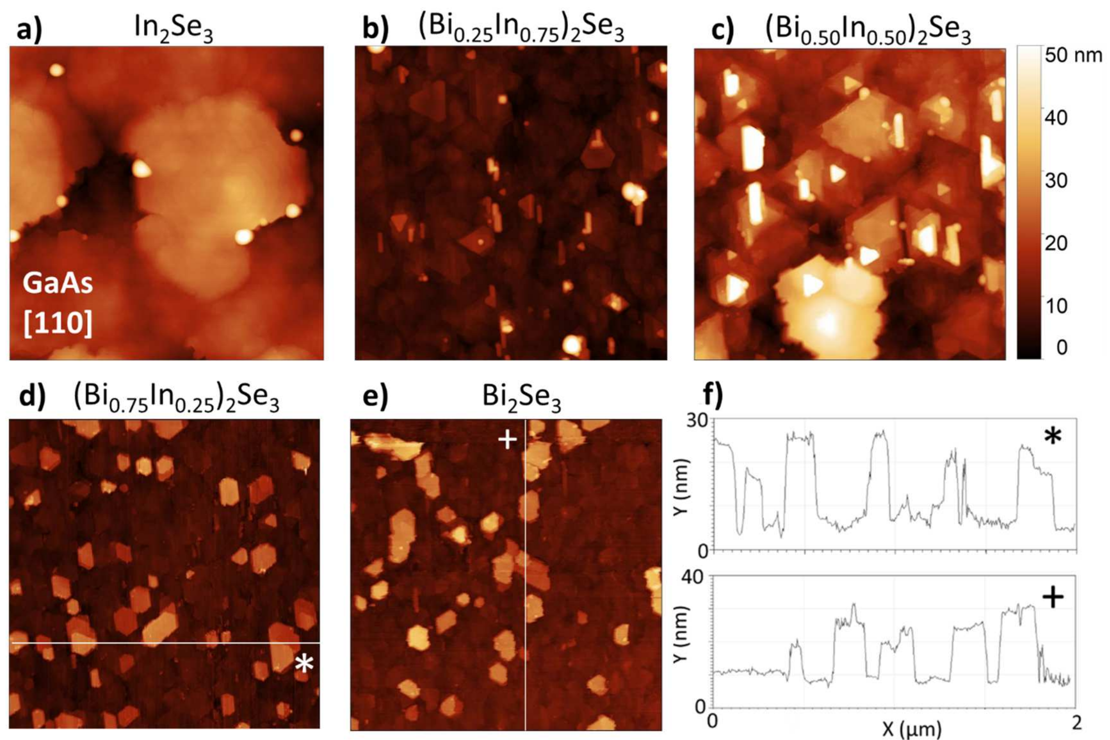

Figure 7.3 (a-e) AFM images of $(Bi_{x-1}In_x)_2Se_3$ films grown at varying indium to bismuth ratios: (a) Sample G with x=1, (b) Sample H with x=0.75, (c) Sample I with x=0.5, (d) Sample J with x=0.25, (e) Sample K with x=0. All AFM images are 2μm x 2μm and have the same scale bar and orientation relative to the substrate. (f) Line cuts of (d) and (e) showing the heights of the nanowires.

grown on identical seed layers and using an identical selenium flux of ~$4x10^{-6}$ Torr. As shown in Figure 7.3.a, the pure In_2Se_3 film has large, micron-scale domains with an approximately hexagonal shape and a fractal-like border [48]. High indium content alloys (x= 0.75 and 0.50) have primarily flat triangular domains with small needles as a secondary phase as shown in Figure 7.3.b and Figure 7.3.c. Films with low indium content (x=0.25 or 0) grow as distinct hexagonal columns or nanowires as shown in Figure 7.3.d and Figure 7.3.e. These nanowires range from 50-150nm in diameter and have sheer walls as shown in the linecuts in Figure 7.3.f. The heights of the nanowires are uniform and stepped: for the pure Bi_2Se_3 sample, nanowire heights cluster around 10 nm, 15 nm and 20 nm only (Figure 7.3.f). In all cases, the features of the film remain aligned along the (110) axis of the substrate.

7.6 X-Ray Diffraction Data

Finally, we want to determine the crystal structure and phase of the films. In_2Se_3 is known to have multiple polymorphs, usually denoted as α, β, γ, δ, and κ. The α and β polymorphs have the same crystal structure and similar lattice constant to Bi_2Se_3. In Figure 7.4, we show x-ray diffraction scans of Samples D-K. As the selenium pressure during growth is varied, the change in morphology is accompanied by a change in dominant polymorph as shown in Figure 4a. The columnar nanowire morphology grown at the high selenium flux (red trace in Figure 7.4.a) predominately contains the standard (001) orientation of $(Bi_{1-x}In_x)_2Se_3$, which is the typical phase for vdW epitaxy of these materials. At lower selenium fluxes, the smooth and needle morphologies (black and blue traces in Figure 7.4.a) show a significant contribution

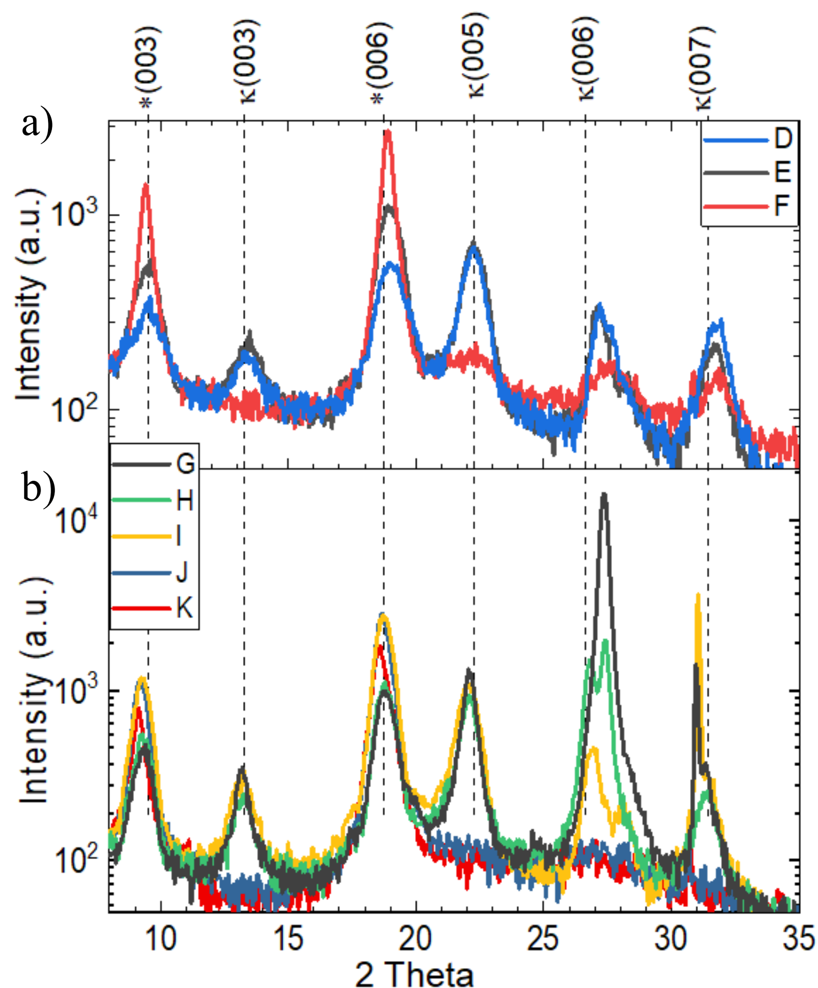

Figure 7.4 XRD scans of (a) Samples D, E, and F and (b) Samples G-K. The * represents a standard orientation $(Bi_{1-x}In_x)_2Se_3$ peak while the κ represent a κ-phase In_2Se_3 peak.

from κ-phase In_2Se_3. A similar trend is seen for Samples G-K in Figure 7.4.b. For the nanowire morphology at high bismuth content, (red and blue traces) the XRD data shows only standard phase material with small variations in the peak position due to the varying Bi:In ratio. At 50% indium and above as the morphology changes, strong κ-phase peaks appear (yellow, green, and black traces in figure). Above 75% an additional peak appears near 28 degrees. We believe this is the cubic phase of In_2Se_3, though information on this phase is scarce. Taken together, these data indicate that the

columnar nanowires are comprised purely of the standard phase and their composition varies as the Bi:In ratio is changed. The needles, on the other hand, are most likely entirely kappa phase In_2Se_3. It is currently unclear which physical features correspond to the cubic phase, which may be entirely buried and invisible to AFM and SEM.

7.7 Effectiveness of the Buffer Layer

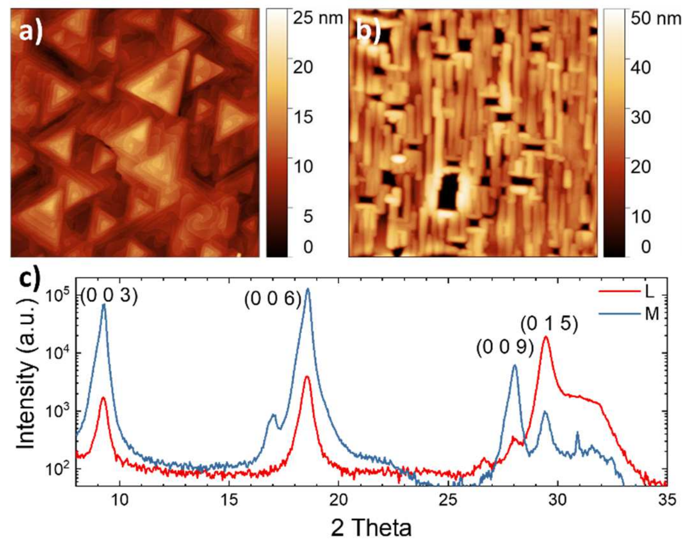

Figure 7.5 AFM images of Bi_2Se_3 grown on (a) a smooth buffer later (Sample L) or (b) a buffer layer with a needle morphology (Sample M). (c) XRD scans of Sample L (red) and Sample M (blue).

Finally, to evaluate the effectiveness of $(Bi_{x-1}In_x)_2Se_3$ as a buffer layer, Bi_2Se_3 films were grown on two buffer layers grown with different selenium fluxes: Sample L, on a buffer layer grown under a selenium flux of 3.09×10^{-6} Torr, and Sample M, grown on a buffer layer using a selenium flux of 1.23×10^{-6} Torr. In Figure 7.5.a, the AFM scan of Sample L shows the expected triangular pyramid morphology for Bi_2Se_3. The accompanying XRD scan (Figure 7.5.c) shows predominantly peaks in the (001) orientation. The Bi_2Se_3 grown on the high selenium flux buffer layer reported a room-temperature mobility of 785 cm^2/Vs and a sheet density of 1.57×10^{13} cm^{-2}, a considerable improvement over Bi_2Se_3 grown on unbuffered GaAs which had a mobility of 597 cm^2/Vs and a sheet density of

$3.67 x 10^{13}$ $cm^{-}2$. When using a buffer layer grown with a low selenium overpressure, the morphology of the Bi_2Se_3 is changed dramatically. As shown in Figure 7.5.b, the pyramids are replaced by long rectangular features, a symmetry impossible for the hexagonal (001) orientation. The XRD pattern reveals the presence of the (015) orientation. This suggests that Bi_2Se_3 is nucleating along the needles we see in buffer layers grown with low selenium fluxes, resulting in the vdW bonds aligned at angle to the substrate.

7.8 Discussion

We will now discuss how the interaction between the film and the substrate is driving the formation of these unique morphologies. We first discuss the morphology of the seed layer. When the seed layer is grown on a sapphire substrate, it is comprised of small triangular domains with no clear orientation to the substrate. [88] However, when we grow on GaAs(001), we find that the domains are oriented along the GaAs[110] direction. This is most obvious in the small rectangular domains that emerge during the initial Bi_2Se_3 seed layer shown in Figure 1a. We attribute this alignment to a longer bismuth diffusion length along this direction driven by the anisotropy in surface energy due to the (2x4) GaAs surface reconstruction. [94] During the growth of the In_2Se_3 layer (Figure 7.1.a) and into the anneal (Figure 7.1.c), the rectangular domains are replaced by triangular domains but the orientation of the domains along the GaAs[110] axis is preserved.

In order to understand the buffer layer morphologies, we must first discuss how TI films normally grow. Bi_2Se_3 and In_2Se_3 films usually grow as triangular domains with a terraced or spiral pyramidal morphology (see Figure 7.5.a for an

example as well as [38,88,95]). The triangular domain shape is thought to be caused by differences in growth rates of the Bi_2Se_3 $[\bar{1}2\bar{1}]$ and $[\bar{2}11]$ edges. [96] These are the two edges of the hexagonal unit cell in the *a*-*b* plane. The unreconstructed $[\bar{2}11]$ edge has one dangling bond per edge atom while the unreconstructed $[\bar{1}2\bar{1}]$ edge has two dangling bonds per edge atom. Adatoms will therefore preferentially incorporate at the $[\bar{1}2\bar{1}]$ edge, causing this edge to grow much faster than the $[\bar{2}11]$ edge. This difference in growth rates leads to the characteristic triangular domains of Bi_2Se_3 and related vdW materials. When these domains encounter a step edge on the substrate, spiral growth in the vertical direction can occur due to the difference in edge growth rate, leading to the terraced pyramids normally observed for Bi_2Se_3 thin films. Finally, terraced growth can also occur in vdW materials due to the weak interaction between the film and substrate. [48] When the film-substrate interaction is weak, the energy barrier for adatoms to diffuse up from a lower layer to a higher layer is significantly reduced. In modeling, this can lead to domains that exhibit a terraced morphology. Taken together, these effects explain the characteristic pyramidal, triangular domains that are commonly observed in vdW films.

Our nanowires clearly exhibit a significantly different growth mode. To understand the growth, we first discuss the growth of catalyst-free GaN nanowires as they display the same morphology and can provide insight into the Bi_2Se_3 growth mechanisms. [97–102] In the case of GaN, previous experiments found that high substrate temperatures and low gallium fluxes were needed to form nanowires. [99] They found that the nucleation density of GaN nanowires increased either as the V:III ratio increased or by using higher atomic nitrogen concentrations rather than nitrogen dimers. [99] These data all indicate that a long gallium adatom diffusion length is key

for nanowire formation. [98] Nanowire nucleation likely occurs randomly with the nucleation density controlled by the gallium diffusion length. [103] After nuclei are formed, nanowire growth proceeds because the sticking coefficient for gallium adatoms is much higher at the nanowire tip than at the sidewall. [103] If a gallium adatom impinges at the tip of the nanowire, it will incorporate. If the gallium adatom impinges within a diffusion length of the tip, it will diffuse up the nanowire sidewalls and incorporate. [97] Adatoms that are not within a diffusion length of a nanowire tip only encounter the sidewalls of the nanowire and re-evaporate into the chamber. [100] We propose that this mechanism can also describe the formation of Bi_2Se_3 nanowires.

In our experiments, we find that nanowires are only formed for the relatively high-bismuth-content samples (x=0 and x=0.25 frequently; x=0.5 under some conditions). Bismuth is a surfactant material and generally has a long adatom diffusion length compared to indium. We also find that the morphology has a strong dependence on selenium overpressure. When the selenium overpressure is high, we observe nanowires; when it is low, we observe either secondary phases or a relatively flat and featureless film. We note again here that we are using a selenium cracker source, which produces more reactive selenium molecules compared to a traditional thermal source. This is equivalent to the more reactive nitrogen species required to form GaN nanowires. These observations are consistent with the results from GaN nanowires, in which a large nitrogen concentration was required for their formation.

For high indium content films, the lower adatom diffusion length leads to a higher density of domains that merge and grow via the normal vdW growth mechanism. For the high-bismuth-content samples, we propose that a relatively low density of well-separated domains are nucleating and growing into nanowires. We

propose that the longer diffusion length of bismuth atoms along with a surface reconstruction, along the side walls of the domains, caused by the high selenium overpressure is driving the formation of the nanowires. Bismuth atoms impinging upon the sample will either land on the top of a nanowire, on the side of a nanowire, or on the buffer layer between nanowires. Those landing on top of the nanowire will incorporate, adding to the nanowire length. Those landing on the side of a nanowire will either diffuse to the top and incorporate or re-evaporate. Likewise, adatoms landing on the buffer layer between nanowires will either diffuse up to the top of the nanowire and incorporate or re-evaporate. Diffusion up the nanowires is likely assisted by the weak film/seed layer interaction as noted above.

The question of why the bismuth adatoms do not incorporate at the sidewalls of the nanowires remains. To answer this, we note that the shape of the nanowires is not precisely triangular as is commonly observed for Bi_2Se_3 domains. Instead, we observe hexagonal and rhombohedral domains. The domain shape is easier to see in the SEM images rather than the AFM images due to tip-sample convolution in the latter case. As described previously, triangular domains are caused by differences in the growth rates of the $[\bar{1}2\bar{1}]$ and $[\bar{2}11]$ edges caused by differences in number of dangling bonds. We hypothesize that the selenium dangling bonds on the side walls of the nanowires undergo a reconstruction such that the number of dangling bonds on each edge is equal, thereby leading to equal growth rates in all directions. The reconstructed surfaces may also satisfy dangling bonds and significantly depress the probability of bismuth incorporation on the nanowire sidewalls. This reconstruction may be caused by the relatively large selenium overpressure; surface reconstructions

are known to change in the III-V family as the group V overpressure is changed. [104–107]

We observe that all nanowires have characteristic heights: each nanowire is either 10nm, 15nm, or 20nm high. We attribute this to an energetic effect. Nanowires grow taller by bismuth adatoms diffusing up the nanowires and incorporating on top. There is some energy cost to diffusing up the nanowire, which is offset by the energy of incorporation. At some critical height, the energy cost to diffusing up the nanowire will equal the energy cost of starting a new nanowire either adjacent to an existing nanowire or elsewhere on the substrate. Adatoms can now diffuse up the shorter nanowire and either incorporate on top of the shorter nanowire or diffuse up a second time and incorporate on top of the taller nanowire. This leads to nanowires with defined height differences across the substrate.

Finally, we will discuss Bi_2Se_3 films grown on low selenium flux buffer layers, which were demonstrated to grow in the (015) orientation. Growth in this orientation has been reported previously, but only when the substrate had been purposely patterned. [108,109] Most studies that report (015) growth refer to it as the (221) orientation. This is due to how the basis vectors are chosen; in the scheme in which the alternative orientation is (221), the conventional growth orientation would be called (111) rather than (001) orientation. [108], [110] For the sake of continuity with our previous studies we have chosen the (001) and (015) index labels, where the (001) phase grows with the vdW gaps parallel to the substrate and the (015) has vdW gaps at an angle to the substrate. On the patterned substrates, the vdW face of the Bi_2Se_3 nucleated along the facet walls, leading to the non-standard film orientation. In our system, it is likely that the needles of the κ-phase In2Se3 are acting as the faceted

nucleation sites that allow for growth of the (015) orientation. While this orientation is not as well studied as the (001) orientation, it is still believed to have topological surface states. [111] Additionally, the (015) orientation provides much greater access to the vdW gaps than thin films of Bi_2Se_3 (001). Easy access to the vdW gaps could allow for the intercalation of atoms for energy storage applications. [112]

7.9 Conclusion

In this chapter, the growth of $(Bi_{1-x}In_x)_2Se_3$ on GaAs(001) was explored and resulted in multiple unexpected morphologies. These unusual morphologies can be attributed to a competition between the high surface mobility of bismuth and the tendency for In_2Se_3 to for secondary phases. During the seed layer deposition, the fast diffusion of bismuth along the GaAs[110] direction establishes an alignment that is maintained during the growth regardless of the final morphology. At high bismuth content and high selenium fluxes, the high mobility of the bismuth dominates the growth resulting in columnar nanowires. Conversely, at high indium content and low selenium fluxes, significant secondary phase growth occurs with the formation of κ-phase needles. At intermediate fluxes, flat and relatively featureless films are growth. The ability to obtain such widely-varying morphologies in a van der Waals system is quite unexpected and previously unobserved, but can be understood by considering the film/substrate interaction. These results set the stage for the synthesis of a variety of interesting and unusual van der Waals material growth morphologies.

Chapter 8

COUPLED 2D DIRAC PLASMONS IN BISMUTH SELENIDE THIN FILMS

8.1 Introduction

One of the features that makes Bi_2Se_3 so interesting to researchers are the unique plasmons that can be excited in their topological surface states. These plasmons have resonances in a wavelength ranges known as the Terahertz (THz) Gap, a technologically important yet difficult to access region of the electromagnetic spectrum. Functional Bi_2Se_3 plasmonic devices could help to improve the performance of inefficient sources and detectors. Improved THz technology would be beneficial for cosmic observation, medical imaging, and the detection of toxic gases, among other applications. As discussed in Section 2.3.2, these plasmons will also inherit the properties of their constituent electrons resulting in 2D Dirac (massless) plasmons. Due to the spin momentum locking of their electrons, TIs are the only single material system in which spin plasmons can be housed and observed at room temperature. Spin plasmons have been extensively theoretically studied as possible spin rectifiers for spintronic devices [83] and a way to optically control the spin state of a propagating wave. Spin plasmons would also provide a link between plasmonics and emerging spintronic technology. Recent improvements in the quality of epitaxially grown thin films allow scientists to examine the plasmons in TSS without significant interference from bulk carriers. Work in this chapter was published in Ginley et al. [113]

As discussed in Section 2.3.2, the 3D nature of Bi_2Se_3 allows for the existence of two carrier pathways beyond the TSS: bulk doping and a band bending 2DEG at the interface of the TI and adjacent material. [37] Thankfully, the plasmon types can be easily distinguished based on their differing dispersion relations. By mapping how the plasmon frequency depends on film thickness as well as wavector, it is possible to determine that which kind of plasmon was excited. Equation (8.1) shows the dispersion relation for massive bulk plasmons, where ω_p is the plasmon frequency, e is the electron charge, n_M is the 2D sheet density, ε_r is the average permittivity of the surrounding materials, and q is the wavevector of light. In the case of a massive bulk plasmon, the plasmon frequency is expected to increase with film thickness as n_M increases. [38] For a 2DEG, n_M is independent of film thickness and so the plasmon frequency will remain constant. In equation (8.2) we see the the dispersion relation for coupled 2D Dirac plasmons. [39] Here v_F is the Fermi velocity, n_D the 2D Dirac carrier density, d is film thickness, and ε_T, ε_B, ε_{TI} are the permittivities above, below, and inside the TI respectively. We use as value of 1 for ε_T while ε_B and ε_{TI} are given by equation (8.3) and (8.4) respectively . [40,41] The values for Equation 3 were experimentally determined to be the values of n_o= 3.2, λ = 20.4 × 10−4 cm, and γ = 0.036 and the values for equation (8.4) are given in table Table 8.1.For coupled 2D Dirac plasmons, the plasmon frequency will increase with film thickness but at much slower rate than 2D massive plasmons. Thus, by mapping the plasmon frequency as a function of both wavevector and film thickness, we can distinguish all three types of plasmons.

$$\omega_p^2 = \frac{e^2}{4\varepsilon_0\varepsilon_r}\frac{n_M}{m^*}q \quad (8.1)$$

$$\omega_p^2 = \frac{e^2}{\varepsilon_0}\frac{v_F\sqrt{2\pi n_D}}{h}\frac{q}{\varepsilon_T+\varepsilon_B+qd\varepsilon_{TI}} \quad (8.2)$$

$$\varepsilon_B(\omega) = n_0^2 + (n_o^2 - 1)(\lambda\omega)^2 + i\gamma(n_o^2 - 1)(\lambda\omega) \quad (8.3)$$

$$\varepsilon_{TI}(\omega) = \varepsilon_\infty - \frac{\omega_D^2}{\omega^2+i\omega\gamma_D} + \frac{\omega_a^2}{S_a^2-\omega^2-i\omega\gamma_a} + \frac{\omega_b^2}{S_b^2-\omega^2-i\omega\gamma_b} + \frac{\omega_g^2}{S_g^2-\omega^2-i\omega\gamma_g} \quad (8.4)$$

Table 8.1 Frequency (ω_x), strength (S_x), and losses (γ_x) for the variables in equation (8.4) Reproduced with permission from [113]

Oscillator	ω_x [cm^{-1}]	S_x [cm^{-1}]	γ_x [cm^{-1}]
Drude (D)	908.66	0	7.43
α-phonon (a)	675.9	63.03	17.5
β-phonon (b)	100	126.94	10
Gap (g)	11249	2029.5	3920.5

8.2 Extinction Spectra

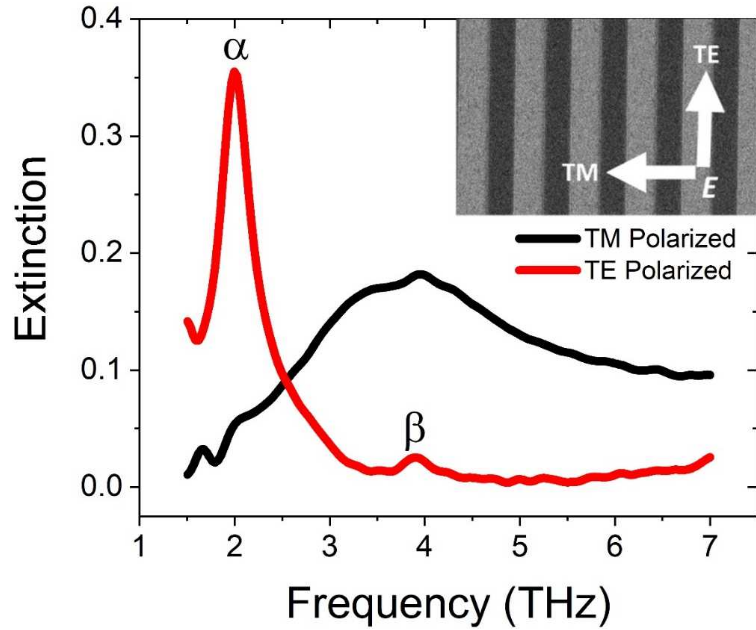

Figure 8.1 Extinction as a function of frequency for a sample with $d = 100$nm and $W = 2$μm for TE (red) and TM (black) polarized light. The α and β phonons are marked in the TE spectrum. Inset shows a scanning electron microscopy plot of a fabricated stripe array with the TE and TM electric field directions indicated. Reproduced with permission from [113]

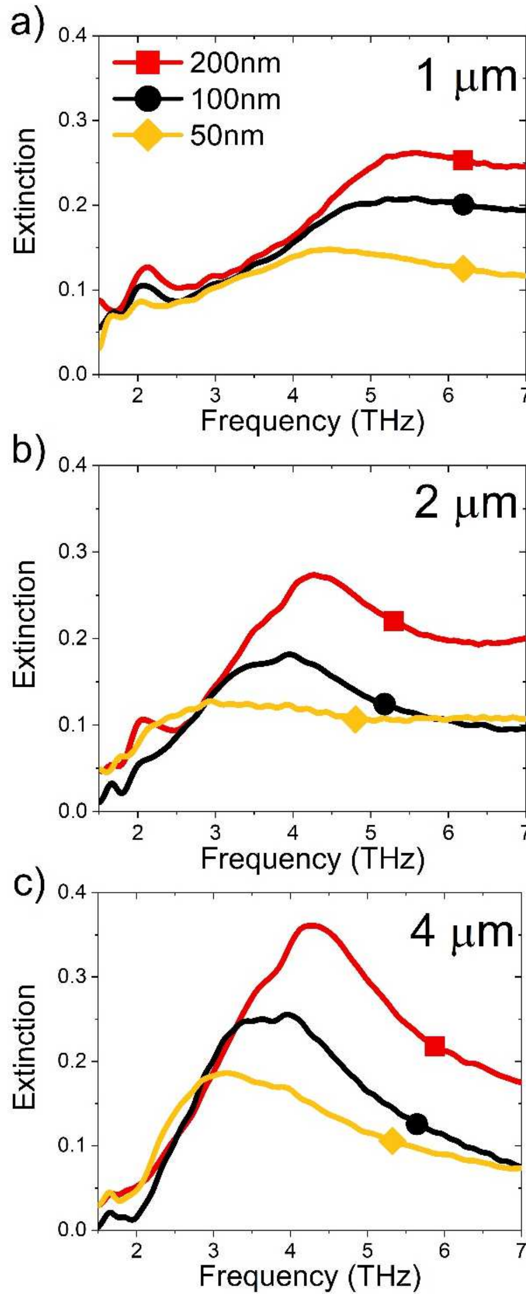

Figure 8.2 Extinction spectra for samples with stripe width of 1μm (a), 2μm (b), and 4μm (c). Film thicknesses of 200nm (red square), 100nm (black circle), and 50nm (yellow diamond) are shown in each plot. Reproduced with permission from [113]

In this study, we excite localized surface plasmons in Bi_2Se_3 thin films of varying thickness. The films are patterned into arrays of stripes of width W and periodicity $2W$ to change momentum $q = \pi/W$ to the incoming photon, enabling excitation of the plasmon discussed in Section 2.3.1. When taking FTIR measurements, the light is polarized either parallel to the stripes (transverse electric, TE) or perpendicular to the stripes (transvers magnetic, TM). As can be seen in Figure 8.1, TE light does not excite the plasmon and the extinction spectra shows an α-phonon around 2THz and a weaker β-phonon around 4THz. Under TM light, the α-phonon disappears due to a Fano interaction with the excited plasmon and a much broader excitation peak appears as evidence of the plasmons' excitation. Figure 8.2 shows the TM extinction spectra for nine films of varying thickness (50-200nm) and stripe widths

(1-4μm). When comparing films with constant stripe widths in Figure 8.2, the extinction peak shifts to higher frequencies as film thickness increases, as expected for a coupled 2D Dirac plasmons. As the peak shifts to higher frequencies the coupling between the α-phonon and plasmon weakens, resulting in a reemergence of the α-phonon peak at 2THz; this trend is most obvious in Figure 8.2.a. The β-phonon in these samples is too weak to produce a significant Fano interaction even as the plasmon frequency approaches 4THz.

8.3 Data Fitting

$$\gamma_I = \frac{2\pi v^2}{1+\left(\frac{\omega-\omega_p}{\gamma_p/2}\right)^2} \quad (5)$$

$$\varphi = \frac{\omega-\omega_I}{\gamma_{ap}/2} - \frac{\omega-\omega_p}{\gamma_p} \quad (6)$$

$$q = \frac{v*w/\gamma_p^{1/2}}{\gamma_I/2} + \frac{\omega-\omega_p}{\gamma_p/2} \quad (7)$$

$$P_{NI} = \frac{S_{NI}}{\pi} * \frac{\gamma_{NI}}{2\left((\omega_{NI}-\omega)^2+\left(\frac{\gamma_{NI}}{2}\right)^2\right)} \quad (8)$$

$$E = \frac{(\varphi+q)^2}{\varphi^2+1} \cdot \frac{\gamma_p}{1+\left(\frac{\omega-\omega_p}{\gamma_p/2}\right)^2} + P_{NI} \quad (9)$$

In order to extract the plasmon resonances the extinction spectra are fit to Equations (3)-(7), which describe the Fano interaction between a broad excitation (the plasmon) and a discreate excitation (the phonon) as shown by Giannini et. al. [114] These equations contain the plasmon frequency (ω), plasmon linewidth (γ_p), phonon-plasmon coupling factor (v), photon-phonon coupling factor (w), interacting phonon frequency (ω_I), non-interacting phonon frequency (ω_{NI}), non-interacting phonon linewidth (γ_{NI}), and non-interacting phonon strength (S_{NI}). Equation 5 gives the

plasmon coupled α-phonon line width (γ_l), Equation 6 gives the reduced frequency (φ), Equation 7 gives the Fano factor (q), and equation 8 is the contribution from the non-interacting phonon. These equations were used to create a Mathematica program to hand fit each spectrum, an example of which can be seen in Figure 8.3.

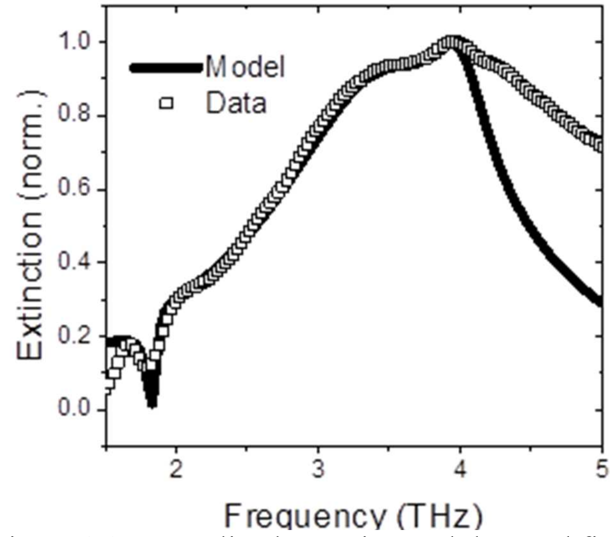

Figure 8.3 Normalized experimental data and fit model for the W=2μm d=100nm sample. Reproduced with permission from [113]

Table 8.2 Physical parameters (film thickness, d, stripe width, W), extracted fit parameters (plasmon frequency (ω_p), plasmon linewidth (γ_p), phonon-plasmon coupling factor (v), photon-phonon coupling factor (w), α-phonon frequency (ω_α), β-phonon frequency (ω_β), non-interacting phonon linewidth (γ_{NI}), and non-interacting phonon strength (S_{NI})), effective mode index (n_{eff}), and plasmon lifetime (τ_{pl}) for all samples. The error for the physical parameters (*d er* and *W er*) was calculated using the average deviation of values measured via AFM and profilometery. Reproduced with permission from [86]

D [nm]	D er [nm]	W [μm]	W er [μm]	ω_p [THz]	γ_p [THz]	v [THz$^{1/2}$]	w [THz]	ω_α [THz]	ω_β [THz]	γ_{NI} [THz]	S_{NI} [THz]	n_{eff}	τ_{pl} [fs]
50	11	1	0.12	4.31	3.58	0	0	2.045	4	0.505	0.541	211	140
50	11	2	0.24	3.16	3.5	0.104	0.404	1.976	3.993	0.36	0.36	140	143
50	11	4	0.48	2.87	2.61	0.305	0.848	2.042	3.976	0.531	0.866	114	191
100	22	1	0.12	4.9	3.48	0	0	2.08	4	0.515	0.689	154	144
100	22	2	0.24	3.42	2.1	0.209	0.510	1.934	4	0.515	0.657	128	238
100	22	4	0.48	3.16	1.84	0.373	0.706	2.085*	3.972	0.475	0.672	82	272
200	45	1	0.12	5.42	3.69	0	0	2.1	4	0.562	0.751	139	136
200	45	2	0.24	4.24	2.53	0.225	0.710	2.046	4	0.01	0.01	97	197
200	45	4	0.48	4.01	2.9	0.418	0.886	2.080*	4	0.01	0.01	77	172

Priority was given to achieving a good fit over the 1.5-4.5 THz range due to the poor signal to noise ratio of the detector outside of this range. Using this method self-consistent values were determined for all nine extinction spectra, as can be seen in Table 8.2.

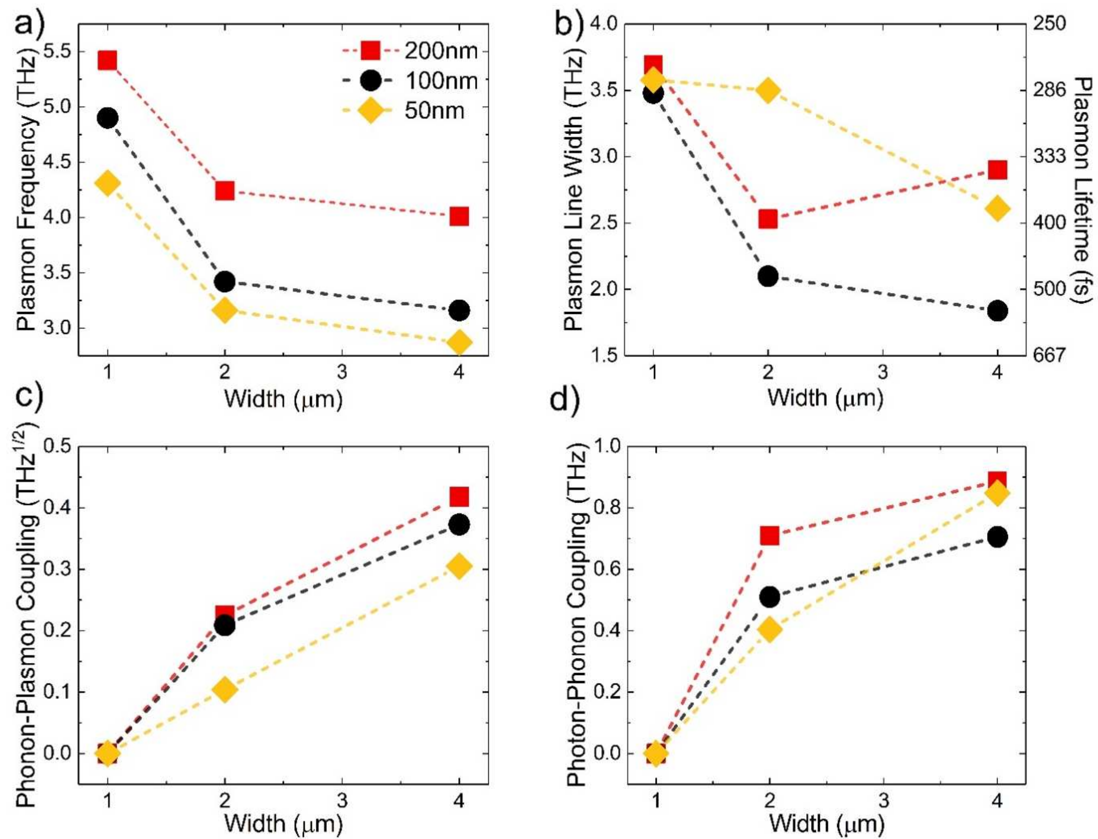

Figure 8.4 Extracted fitting parameters as a function of stripe width: plasmon frequency (a), plasmon linewidth and lifetime (b), phonon-plasmon coupling (c), and photon-phonon coupling (d). Film thicknesses of 200nm (red square), 100nm (black circle), and 50nm (yellow diamond) are shown in each plot. Dashed lines are a guide to the eye. Numerical values for these data are tabulated in Table 8.2 Reproduced with permission from [113].

We extracted four key parameters from these fits: the plasmon frequency (ω_p), plasmon linewidth (γ_p), phonon-plasmon coupling factor (v), and photon-phonon coupling factor (w). As can be seen in Figure 8.4.a, for films with a constant thickness,

a decrease in plasmon frequency is seen as stripe width increases, behavior consistent with either a massive or massless 2D plasmon. Looking at films with constant stripe we see an increase in plasmon frequency with increasing film thickness, which is consistent with a coupled 2D plasmon. From the extracted plasmon lines widths we calculated the plasmon lifetimes using $\tau_{pl} = 1/\gamma_{pl}$. Figure 8.4.b shows the plasmon lifetimes range from ~270-540fs and a trend towards larger linewidths and shorter lifetimes at smaller stripe widths. This is unsurprising as narrower stripes will be increasingly affected by any fabrication damage along the exposed edges to the higher surface:bulk ratio. The exposed sides are especially of concern since van der Waals materials are more prone to aging along the a and b-axis due to the broken bonds in this plane. No clear trend can be seen for plasmon lifetime across film thickness since it plays a much smaller role in determining the scattering rate and lifetime, due to the high quality of our materials.

The phonon-plasmon coupling factor, shown in Figure 8.4c, and photon-phonon coupling factor, shown in Figure 8.4.d, increase with both stripe width and film thickness. In thicker films, more bulk material is available to interact with the topological surface states and the incoming photon, leading to stronger coupling with the bulk phonon. As predicted by the dispersion formula, decreasing stripe width results in an increased plasmon frequency. This trend shifts the plasmon away from the phonon at 2THz, resulting in decreased phonon-plasmon coupling as stripe width decreases. Given the interdependence between the coupling factor and the linewidth, consistency between all 9 samples was taken into consideration while determining the best fits for each sample. The robust nature of the plasmon frequency across a wide range of fitting values gives us confidence in the fitting process.

Figure 8.5 show the extracted plasmon frequencies for varying film thicknesses and stripe widths plotted against the theoretical dispersion curves of coupled 2D plasmons (Equation 8.10) over the same parameter space. Based on Hall measurements of an unpatterned sample grown under the same conditions as the plasmon samples, a sheet carrier density of 2.38×10^{13} cm^{-2} was used to generate the theoretical curves. When plotting plasmon frequency as a function of wavevector in Figure 8.4.a or film thickness in Figure 8.4.b. the experimental values show excellent agreement with the theoretical curves. In Figure 8.4.a, the samples with the 1μm stripe width show a deviation towards higher frequencies (smaller line widths) than the theoretical curves. We attribute this to the increased affection of fabrication damage on the thinner strip widths, as discussed previously. Since there is no satisfactory way to determine an "effective stripe width" without introducing error and bias, the measured stripe widths were used. Overall, the agreement between the theoretical curves and the experimental data indicates that we are exciting couples 2D Dirac plasmons in the surface states of the topological insulator samples.

To further rule out bulk plasmons as an explanation of our findings, dispersion curves for bulk plasmons were also plotted against the experimental data. In Figure 8.5.a, the measured sheet carrier density of 2.38×10^{13} cm^{-2} was used to generate the bulk curve. As can be seen, it falls well short of accurately modeling the experimental values. The sheet carrier density would have to be decreased by two orders of magnitude to even approximate the experimental data using the bulk plasmon dispersion formula. In Figure 8.5.b, using the measured sheet density generated a curve below 0.2THz and was not visible on the plot. In order to make the bulk curve occupy the same range as the experimental values, a 3D carrier density of 1.5×10^{21}

cm^{-3} was used. This is equivalent to 3×10^{16} cm^{-2} for a 200nm film and is orders of magnitude higher than even the worst Bi_2Se_3 films we have ever grown. Despite using this unrealistic number to generate the bulk curve, its slope is still an extremely poor fit for the experimental values. Since other groups have found a small contribution to the extinction signal from massive carriers[4,5], we modified Equation 2 to include both the Fermi energy of the Dirac carriers (E_F^D) as well as the Fermi energy from a massive channel (E_F^{2DEG}) [4,6], as seen in Equation 8.10. Using this equation, we increased the massive carrier density while decreasing the Dirac carrier density to maintain a total sheet density of 2.38x10^{13} cm^{-2}. The addition of even a few percent of massive carrier resulted in a dramatic blue-shift away from the experimentally-observed values. Having ruled out bulk plasmons and a massive carrier contribution,

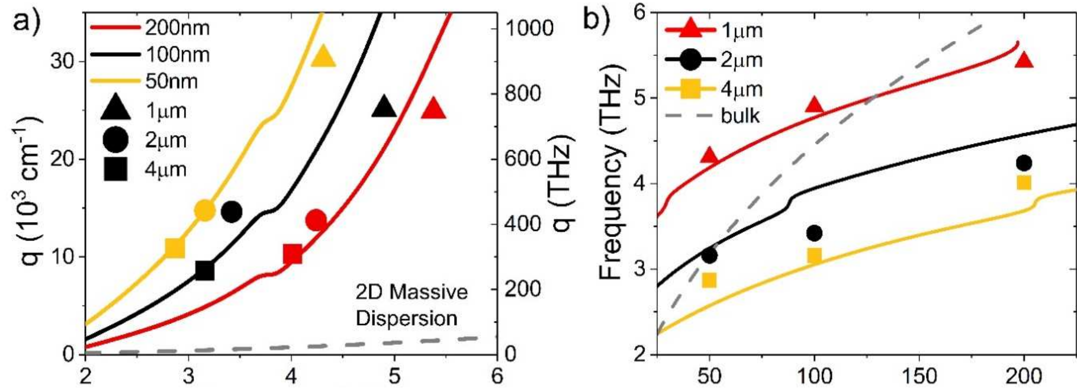

Figure 8.5 Experimental plasmon frequencies and theoretical dispersion curves for coupled 2D Dirac plasmons. (a) Theoretical curves for *d*=200nm (red line), *d*=100nm (black line), and *d*=50nm (yellow line). Experimental plasmon frequencies are shown as triangles (*W*=1μm), circles (*W*=2μm), and squares (*W*=4μm) in the corresponding thickness color. Dashed line shows the theoretical dispersion for a massive plasmon with $n_s = 2.38 \times 10^{13}$ cm^{-2}. (b) Theoretical curves for W=1μm (red line), W=2μm (black line), and W=4μm (yellow line). Experimental plasmon frequencies are shown as triangles (W=1μm), circles (W=2μm), and squares (W=4μm) in the corresponding stripe width color. Dashed line shows the dispersion curve for a massive plasmon with $n_{3D} = 1.5 \times 10^{21}$ cm^{-3}. Reproduced with permission from [113]

we can confidently conclude that the excited plasmons are entirely 2D coupled Dirac plasmons in the topological surface states.

$$\omega_p^2 = \frac{e^2}{2\pi\varepsilon_0\hbar^2}\left(E_F^D + 4E_F^{2DEG}\right)\frac{q}{\varepsilon_T+\varepsilon_B+qd\varepsilon_{TI}} \quad (8.10)$$

These results also reveal that Bi_2Se_3 surface states have an amazing ability to compress light. The effective mode index, defined as $n_p = q/\omega_p$, quantifies the ability of a material to compress light. For example, an effective mode index of 10 mean that light is compressed to 1/10th of its' free space wavelength. As show in Figure 8.4 these samples have effective indices between 77 and 211. These values are significantly higher than traditional materials and some even surpass Graphene, whose value is general reported to be around 100. [115] High degrees of confinement are usually accompanied by short lifetimes, however these samples exhibit relatively high plasmon lifetimes (333-550 fs). Large mode indices combined with the relatively long plasmon lifetimes make Bi_2Se_3 an excellent candidate for improved sensor and waveguide technology. Improved material quality, as described in Chapter 6, may further improve plasmon lifetime. The advantage of bismuth chalcogenide topological insulators over other material systems may be their place at intersection of 2D and 3D materials. These materials can take advantage of the high degree of confinement found in 2D material system like graphene while being able to implement the easier manufacturing methods of 3D materials.

In this chapter, we conclusively demonstrated the excitation of coupled 2D Dirac plasmons in Bi_2Se_3 by comparing experimentally determined values to the theoretical extinction curves. As expected, we saw increase in plasmon frequency with both increased film thickness and decreased stripe width. It was also show that Bi_2Se_3 has an amazing ability to confine light, with effective mode indices of up to 211. All

the films discussed in the chapter were grown using the method described in chapter 6. The improved film quality achieved by methods discussed in later chapters, as well as the ability to grow Bi_2Se_3 and $(Bi_{1-x}In_x)_2Se_3$ heterostructures, will be employed by future students in the Law group to further explore plasmon behavior in bismuth chalcogenide thin films. Demonstrating excitation of coupled 2D Dirac plasmons in Bi_2Se_3 the first step towards a wide variety of future projects.

Chapter 9

CONCLUSION

Over the course of this doctoral work, many research projects were completed with the goal of better improving bismuth chalcogenide topological insulators film quality. In the first study, it was found that using a selenium cracker source during growth improved selenium incorporation. Using a Se:Bi flux ratio of 4:1 during growth a room temperature sheet density of $3.32 \pm 0.2 \times 10^{13}$ cm^{-2} and mobility of 623 ± 30 cm^2/Vs were demonstrated, comparable to literature values using up to a 200:1 Se:Bi ratio with a traditional Knudsen cell. A studying on alloying Bi_2Se_3 with Bi_2Te_3 failed to show a reduction in carriers at the Bi_2Te_2Se composition, as expected from studies on bulk material. This, along with evidence from RHEED and thickness vs sheet carrier studies, led to the conclusion that bulk-like defects were not the primary cause of high doping levels in our thin films. Instead it was theorized that a disordered interface layer was the culprit. To remedy this, a $(Bi_{1-x}In_x)_2Se_3$ buffer layered was used to trap the disordered layer away from the topological surface states. Using this method, we saw a 50% reduction in sheet density and a 50% increase in mobility as compared to an unbuffered sample. This represents significant improvement in the quality of Bi_2Se_3 grown on a sapphire substrate.

Attempts to use the buffer layer method to improve films grown on GaAs(001) revealed a high degree of surface interaction resulting in many three-dimensional morphologies. It was concluded that the these resulted from bismuths' high surface and the tendency for In_2Se_3 to phase segregate. By varying composition and growth parameters morphologies ranging from smooth films to columnar growth were achieved. This research represents a step forward in the understanding and control of van der Waals epitaxy growths.

Finally, this research conclusively demonstrated the excitation of coupled 2D Dirac plasmons in Bi_2Se_3 thin films. By patterning samples of varying thicknesses into stripes arrays of varying widths, the shift in plasmon frequency was shown to be consistent with the theoretical dispersion relation and inconsistent with any other explanation. Additionally, the plasmons were demonstrated the ability to confine light down to $1/211^{th}$ its free space wavelength (depending on film parameters).

Bismuth chalcogenide topological insulators are of great interest to scientists due to their unique surface state that form as a result of strong spin orbit coupling. These linear surface states from a gapless Dirac cone in an otherwise trivial semiconductor band structure. The electrons that inhabit the Dirac cone are confined to two dimensions, travel at relativistic speeds, and are spin momentum locked. Studying these surface states may provide insight into fundamental physics applications as well a pathway to future computing technologies. Studying the Molecular Beam Epitaxy growth of bismuth chalcogenide also provides insight into the dynamics of van der Waals epitaxy which may be applied to other van der Waals

material systems. The research in this dissertation contributes to the scientific understanding of these materials and their epitaxial growth dynamics.

REFERENCES

[1] X. L. Qi and S. C. Zhang, Rev. Mod. Phys. **83**, (2011).

[2] L. Fu and C. L. Kane, Phys. Rev. Lett. **100**, 096407 (2008).

[3] A. F. Rigosi, A. R. Panna, S. U. Payagala, M. Kruskopf, M. E. Kraft, G. R. Jones, B.-Y. Wu, H.-Y. Lee, Y. Yang, J. Hu, D. G. Jarrett, D. B. Newell, and R. E. Elmquist, IEEE Trans. Instrum. Meas. **68**, 1870 (2019).

[4] D. Pesin and A. H. MacDonald, **11**, (2012).

[5] I. Appelbaum, H. D. Drew, and M. S. Fuhrer, Appl. Phys. Lett. **98**, 023103 (2011).

[6] M. Autore, F. D'Apuzzo, A. Di Gaspare, V. Giliberti, O. Limaj, P. Roy, M. Brahlek, N. Koirala, S. Oh, F. J. García de Abajo, and S. Lupi, Adv. Opt. Mater. **3**, 1257 (2015).

[7] D. Hsieh, Y. Xia, D. Qian, L. Wray, J. H. Dil, F. Meier, J. Osterwalder, L. Patthey, J. G. Checkelsky, N. P. Ong, A. V Fedorov, H. Lin, A. Bansil, D. Grauer, Y. S. Hor, R. J. Cava, and M. Z. Hasan, Nature **460**, 1101 (2009).

[8] Y. Xia, D. Qian, D. Hsieh, L. Wray, A. Pal, H. Lin, A. Bansil, D. Grauer, Y. S. Hor, R. J. Cava, and M. Z. Hasan, Nat. Phys. **5**, 398 (2009).

[9] Y. L. Chen, J. G. Analytis, J.-H. Chu, Z. K. Liu, S.-K. Mo, X. L. Qi, H. J. Zhang, D. H. Lu, X. Dai, Z. Fang, S. C. Zhang, I. R. Fisher, Z. Hussain, and Z.-X. Shen, Science **325**, 178 (2009).

[10] M. Franz, Nat. Mater. **9**, 536 (2010).

[11] J. J. Lee, F. T. Schmitt, R. G. Moore, I. M. Vishik, Y. Ma, and Z. X. Shen, Appl. Phys. Lett. **101**, 013118 (2012).

[12] N. Garcia and A. Damask, in *Phys. Comput. Sci. Students* (Springer US, New York, NY, 1991), pp. 395–428.

[13] C. Kittel, *Introduction to Solid State Physics*, Third (John Wiley & Sons, Inc, 1967).

[14] D. L. Greenaway and G. Harbeke, J. Phys. Chem. Solids **26**, 1585 (1965).

[15] T. Ginley, Y. Wang, Z. Wang, and S. Law, MRS Commun. **8**, 782 (2018).

[16] J. H. Davies, *The Physics of Low-Dimensional Semicinductors* (2006).

[17] S.-Q. Shen, Phys. World **174**, 32 (2011).

[18] D. A. B. Miller, *Quantum Mechanics for Scientists and Engineers* (2008).

[19] H. Zhang, C.-X. Liu, X.-L. Qi, X. Dai, Z. Fang, and S.-C. Zhang, Nat. Phys. **5**, 438 (2009).

[20] F. Ortmann, S. Roche, and S. O. Valenzuela, *Topological Insulators: Fundamentals and Perspectives* (John Wiley & Sons, 2015).

[21] Y. L. Chen, J. G. Analytis, J.-H. Chu, Z. K. Liu, S.-K. Mo, X. L. Qi, H. J. Zhang, D. H. Lu, X. Dai, Z. Fang, S. C. Zhang, I. R. Fisher, Z. Hussain, and Z.-X. Shen, Science (80-.). **325**, 178 (2009).

[22] C. Day, Phys. Today **61**, 19 (2008).

[23] S. Girvin and R. Prange, *The Quantum Hall Effect* (Springer New York, New York, NY, 1990).

[24] B. A. Bernevig and S. Zhang, Phys. Rev. Lett. **96**, 106802 (2006).

[25] Y. Tokura, K. Yasuda, and A. Tsukazaki, Nat. Rev. Phys. **1**, 126 (2019).

[26] O. V. Yazyev, J. E. Moore, and S. G. Louie, Phys. Rev. Lett. **105**, 266806 (2010).

[27] T. Ginley, Y. Wang, and S. Law, Crystals **6**, 154 (2016).

[28] S. K. Mishra, S. Satpathy, and O. Jepsen, J. Phys. Condens. Matter **9**, 461 (1997).

[29] M. M. Stasova, J. Struct. Chem. **8**, 584 (1967).

[30] X. Chen, X.-C. Ma, K. He, J.-F. Jia, and Q.-K. Xue, Adv. Mater. **23**, 1162 (2011).

[31] D. Koumoulis, B. Leung, T. C. Chasapis, R. Taylor, D. King, M. G. Kanatzidis, and L.-S. Bouchard, Adv. Funct. Mater. **24**, 1519 (2014).

[32] J. R. Drabble and C. H. L. Goodman, J. Phys. Chem. Solids **5**, 142 (1958).

[33] D. O. Scanlon, P. D. C. King, R. P. Singh, A. de la Torre, S. M. Walker, G. Balakrishnan, F. Baumberger, and C. R. A. Catlow, Adv. Mater. **24**, 2154 (2012).

[34] M. Brahlek, N. Bansal, N. Koirala, S.-Y. Xu, M. Neupane, C. Liu, M. Z. Hasan, and S. Oh, Phys. Rev. Lett. **109**, 186403 (2012).

[35] S. A. Maier, *Plasmonics: Fundamentals and Applications* (Springer US, New York, NY, 2007).

[36] E. Hutter and J. H. Fendler, Adv. Mater. **16**, 1685 (2004).

[37] M. Bianchi, D. Guan, S. Bao, J. Mi, B. B. Iversen, P. D. C. King, and P. Hofmann, Nat. Commun. **1**, 128 (2010).

[38] T. P. Ginley and S. Law, J. Vac. Sci. Technol. B **34**, (2016).

[39] T. Stauber, G. Gómez-Santos, and L. Brey, Phys. Rev. B **88**, 205427 (2013).

[40] Y. Deshko, L. Krusin-Elbaum, V. Menon, A. Khanikaev, and J. Trevino, Opt. Express **24**, 7398 (2016).

[41] S. Roberts and D. D. Coon, J. Opt. Soc. Am. **52**, 1023 (1962).

[42] A. J. Ptak, in *Handb. Cryst. Growth* (North-Holland, 2015), pp. 161–192.

[43] K. Alavi, Encycl. Mater. Sci. Technol. 5765 (2001).

[44] N. Chand, T. D. Harris, S. N. G. Chu, E. A. Fitzgerald, J. Lopata, M. Schnoes, and N. K. Dutta, J. Cryst. Growth **126**, 530 (1993).

[45] N. Bansal, Y. S. Kim, E. Edrey, M. Brahlek, Y. Horibe, K. Iida, M. Tanimura, G.-H. Li, T. Feng, H.-D. Lee, T. Gustafsson, E. Andrei, and S. Oh, Thin Solid Films **520**, 224 (2011).

[46] S. Schreyeck, N. V. Tarakina, G. Karczewski, C. Schumacher, T. Borzenko, C. Brüne, H. Buhmann, C. Gould, K. Brunner, and L. W. Molenkamp, Appl. Phys. Lett. **102**, 041914 (2013).

[47] K. W. Post, B. C. Chapler, L. He, X. Kou, K. L. Wang, and D. N. Basov, Phys. Rev. B **88**, 075121 (2013).

[48] B. Lü, G. A. Almyras, V. Gervilla, J. E. Greene, and K. Sarakinos, Phys. Rev.

Mater. **2**, 063401 (2018).

[49] G.-C. Wang and T.-M. Lu, J. Appl. Phys **125**, 82401 (2019).

[50] W. Moritz, in *Phys. Solid Surfaces Subvolume A*, edited by G. Chiarotti and P. Chiaradia (Springer Berlin Heidelberg, Berlin, Heidelberg, 2015), pp. 152–154.

[51] A. A. Ramadan, R. D. Gould, and A. Ashour, Thin Solid Films **239**, 272 (1994).

[52] Wikibook-Contributors, (2019).

[53] S. Nahar, A. Schmets, G. Schitter, and A. Scarpas, in *Asph. Pavements* (CRC Press, 2014), pp. 1397–1406.

[54] F. Gołek, P. Mazur, Z. Ryszka, and S. Zuber, Appl. Surf. Sci. **304**, 11 (2014).

[55] L. Reimer, *Scanning Electron Microscopy*, Second (Springer Berlin Heidelberg, Berlin, Heidelberg, 1998).

[56] ChemBAM, Https://Chembam.Com/Techniques/Electron-Microscopy/ (n.d.).

[57] Rolls-Royce UTC, Univ. Cambridge (2019).

[58] Wikipedia (n.d.).

[59] N. W. Ashcroft and N. D. Mermin, *Solid State Physics* (Holt, Rinehart and Winston, 1976).

[60] A. R. Denton and N. W. Ashcroft, Phys. Rev. A **43**, 3161 (1991).

[61] Sanchonx, WikimediaCommons (2011).

[62] B. C. Smith, *Fundamentals of Fourier Transform Infrared Spectroscopy* (CRC Press, 2011).

[63] B. El-Kareh and L. N. Hutter, *Fundamentals of Semiconductor Processing Technology* (Kluwer Academic Publishers, 1995).

[64] M. J. Madou, *Fundamentals of Microfabrication: The Science of Miniaturization*, Second (CRC Press, 2002).

[65] R. Valdés Aguilar, L. Wu, A. V. Stier, L. S. Bilbro, M. Brahlek, N. Bansal, S. Oh, and N. P. Armitage, J. Appl. Phys. **113**, 153702 (2013).

[66] Y. S. Kim, M. Brahlek, N. Bansal, E. Edrey, G. A. Kapilevich, K. Iida, M. Tanimura, Y. Horibe, S.-W. Cheong, and S. Oh, Phys. Rev. B **84**, 073109 (2011).

[67] L. He, X. Kou, and K. L. Wang, Phys. Status Solidi - Rapid Res. Lett. **7**, 50 (2013).

[68] J. Kampmeier, S. Borisova, L. Plucinski, M. Luysberg, G. Mussler, and D. Grutzmacher, Cryst. Growth Des. **15**, 390 (2015).

[69] C.-L. Song, Y.-L. Wang, Y.-P. Jiang, Y. Zhang, C.-Z. Chang, L. Wang, K. He, X. Chen, J.-F. Jia, Y. Wang, Z. Fang, X. Dai, X.-C. Xie, X.-L. Qi, S.-C. Zhang, Q.-K. Xue, and X. Ma, Appl. Phys. Lett. **97**, 143118 (2010).

[70] J. Berkowitz, J. Chem. Phys. **45**, 4289 (1966).

[71] H. M. Benia, C. Lin, K. Kern, and C. R. Ast, Phys. Rev. Lett. **107**, 177602 (2011).

[72] V. A. Golyashov, K. A. Kokh, S. V. Makarenko, K. N. Romanyuk, I. P. Prosvirin, A. V. Kalinkin, O. E. Tereshchenko, A. S. Kozhukhov, D. V. Sheglov, S. V. Eremeev, S. D. Borisova, and E. V. Chulkov, J. Appl. Phys. **112**, 113702 (2012).

[73] J. H. Dycus, J. S. Harris, X. Sang, C. M. Fancher, S. D. Findlay, A. A. Oni, T. E. Chan, C. C. Koch, J. L. Jones, L. J. Allen, D. L. Irving, and J. M. LeBeau, Microsc. Microanal. **21**, 946 (2015).

[74] Y. Wang, T. P. Ginley, C. Zhang, and S. Law, J. Vac. Sci. Technol. B **35**, (2017).

[75] Y. P. Chen, G. Brill, and N. K. Dhar, J. Cryst. Growth **252**, 270 (2003).

[76] F. S. Turco-Sandroff, R. E. Nahory, M. J. S. P. Brasil, R. J. Martin, R. Beserman, L. A. Farrow, J. M. Worlock, and A. L. Weaver, J. Cryst. Growth **111**, 762 (1991).

[77] B. Predel, in *Landolt-Börnstein - Gr. IV Phys. Chem. 5B*, edited by O. Madelung (Springer-Verlag Berlin Heidelberg, 1992).

[78] S. E. Harrison, S. Li, Y. Huo, B. Zhou, Y. L. Chen, and J. S. Harris, Appl. Phys. Lett. **102**, 2011 (2013).

[79] H. D. Li, Z. Y. Wang, X. Kan, X. Guo, H. T. He, Z. Wang, J. N. Wang, T. L. Wong, N. Wang, and M. H. Xie, New J. Phys. **12**, 103038 (2010).

[80] N. Bansal, Y. S. Kim, M. Brahlek, E. Edrey, and S. Oh, Phys. Rev. Lett. **109**, 116804 (2012).

[81] A. Ghasemi, D. Kepaptsoglou, L. J. Collins-McIntyre, Q. Ramasse, T. Hesjedal, and V. K. Lazarov, Sci. Rep. **6**, 26549 (2016).

[82] X. Liu, D. J. Smith, J. Fan, Y.-H. Zhang, H. Cao, Y. P. Chen, J. Leiner, B. J. Kirby, M. Dobrowolska, and J. K. Furdyna, Appl. Phys. Lett. **99**, 171903 (2011).

[83] N. Bansal, Y. S. Kim, E. Edrey, M. Brahlek, Y. Horibe, K. Iida, M. Tanimura, G.-H. Li, T. Feng, H.-D. Lee, T. Gustafsson, E. Andrei, and S. Oh, Thin Solid Films **520**, 224 (2011).

[84] N. Koirala, M. Brahlek, M. Salehi, L. Wu, J. Dai, J. Waugh, T. Nummy, M.-G. Han, J. Moon, Y. Zhu, D. Dessau, W. Wu, N. P. Armitage, and S. Oh, Nano Lett. **15**, 8245 (2015).

[85] G. W. Wicks, Crit. Rev. Solid State Mater. Sci. **18**, 239 (1993).

[86] K. Ploog, *MOLECULAR BEAM EPITAXY OF III-V COMPOUNDS: Technology and Growth Process 1* (1981).

[87] E. Luna, F. Ishikawa, B. Satpati, J. B. Rodriguez, E. Tournié, and A. Trampert, J. Cryst. Growth **311**, 1739 (2009).

[88] Y. Wang, T. P. Ginley, and S. Law, J. Vac. Sci. Technol. B **36**, 02D101 (2018).

[89] C. Julien, M. Eddrief, M. Balkanski, E. Hatzikraniotis, and K. Kambas, Phys. Status Solidi **88**, 687 (1985).

[90] N. D. Raranskii, V. N. Balazyuk, Z. D. Kovalyuk, N. I. Mel'nik, and V. B. Gevik, Inorg. Mater. **47**, 1174 (2011).

[91] J. Jasinski, W. Swider, J. Washburn, Z. Liliental-Weber, A. Chaiken, K. Nauka, G. A. Gibson, and C. C. Yang, Appl. Phys. Lett. **81**, 4356 (2002).

[92] C. H. De Groot and J. S. Moodera, J. Appl. Phys. **89**, 4336 (2001).

[93] X. Tao and Y. Gu, Nano Lett. **13**, 3501 (2013).

[94] M. Wu, E. Luna, J. Puustinen, M. Guina, and A. Trampert, Nanotechnology **25**, 205605 (2014).

[95] T. Okamoto, A. Yamada, and M. Konagai, J. Cryst. Growth **175–176**, 1045

(1997).

[96] Y. Liu, M. Weinert, and L. Li, Phys. Rev. Lett. **108**, 1 (2012).

[97] R. Songmuang, O. Landré, and B. Daudin, Appl. Phys. Lett. **91**, 251902 (2007).

[98] K. A. Bertness, N. A. Sanford, J. M. Barker, J. B. Schlager, A. Roshko, A. V. Davydov, and I. Levin, J. Electron. Mater. **35**, 576 (2006).

[99] K. A. Bertness, A. Roshko, L. M. Mansfield, T. E. Harvey, and N. A. Sanford, J. Cryst. Growth **300**, 94 (2007).

[100] K. A. Bertness, A. Roshko, L. M. Mansfield, T. E. Harvey, and N. A. Sanford, J. Cryst. Growth **310**, 3154 (2008).

[101] O. Landré, R. Songmuang, J. Renard, E. Bellet-Amalric, H. Renevier, and B. Daudin, Appl. Phys. Lett. **93**, 183109 (2008).

[102] R. K. Debnath, R. Meijers, T. Richter, T. Stoica, R. Calarco, and H. Lüth, Appl. Phys. Lett. **90**, 123117 (2007).

[103] J. Ristić, E. Calleja, S. Fernández-Garrido, L. Cerutti, A. Trampert, U. Jahn, and K. H. Ploog, J. Cryst. Growth **310**, 4035 (2008).

[104] C. Ratsch, W. Barvosa-Carter, F. Grosse, J. H. G. Owen, and J. J. Zinck, Phys. Rev. B **62**, R7719 (2000).

[105] K. D. Choquette, M. Hong, H. S. Luftman, S. N. G. Chu, J. P. Mannaerts, R. C. Wetzel, and R. S. Freund, J. Appl. Phys. **73**, 2035 (1993).

[106] M. D. Pashley and D. Li, J. Vac. Sci. Technol. A Vacuum, Surfaces, Film. **12**, 1848 (1994).

[107] H. J. Joyce, J. Wong-Leung, Q. Gao, H. H. Tan, and C. Jagadish, Nano Lett. **10**, 908 (2010).

[108] M.-H. Xie, X. Guo, Z.-J. Xu, and W.-K. Ho, Chinese Phys. B **22**, 068101 (2013).

[109] B. Li, Y. Xia, W. Ho, and M. Xie, J. Cryst. Growth **459**, 76 (2017).

[110] H.-D. Lai, S.-R. Jian, L. T. C. Tuyen, P. H. Le, C.-W. Luo, and J.-Y. Juang, Micromachines **9**, (2018).

[111] Z. Xu, X. Guo, M. Yao, H. He, L. Miao, L. Jiao, H. Liu, J. Wang, D. Qian, J.

Jia, W. Ho, and M. Xie, Adv. Mater. **25**, 1557 (2013).

[112] J. L. Atwood, L. J. Barbour, and A. Jerga, Science **296**, 2367 (2002).

[113] T. P. Ginley and S. Law, Adv. Opt. Mater. 1800113 (2018).

[114] V. Giannini, Y. Francescato, H. Amrania, C. C. Phillips, and S. A. Maier, Nano Lett. **11**, 2835 (2011).

[115] S. He, X. Zhang, and Y. He, Opt. Express **21**, 30664 (2013).